N°d'ordre NNT 2022ISAL0090

THESE de DOCTORAT DE L'INSA LYON, membre de l'Université de Lyon

Ecole Doctorale N° ED 34
Matériaux de Lyon

Spécialité de doctorat : Science des Matériaux

Soutenue publiquement le 24/10/2022, par :
Rongrong ZHANG

In situ compression of cerium oxides in environmental transmission electron microscopy

---

Devant le jury composé de :

Olivier THOMAS	Professeur / Aix-Marseille Université	Rapporteur
Anne JOULAIN	Professeur / Université de Poitiers	Rapportrice
Marc LEGROS	Directeur de Recherches / CEMES-CNRS	Examinateur
David COOPER	Docteur / CEA-LETI	Examinateur
David DUNSTAN	Professeur / Queen Mary University of London	Examinateur
Karine MASENELLI-VARLOT	Professeur / INSA Lyon	Directrice de thèse
Lucile JOLY-POTTUZ	Maître de conférences / INSA Lyon	Co-Directrice de thèse

Cette thèse est accessible à l'adresse : https://theses.insa-lyon.fr/publication/2022ISAL0090/these.pdf
© [R. Zhang], [2022], INSA Lyon, tous droits réservés

Cette thèse est accessible à l'adresse : https://theses.insa-lyon.fr/publication/2022ISAL0090/these.pdf
© [R. Zhang], [2022], INSA Lyon, tous droits réservés

Cette thèse est accessible à l'adresse : https://theses.insa-lyon.fr/publication/2022ISAL0090/these.pdf
© [R. Zhang], [2022], INSA Lyon, tous droits réservés

Département FEDORA – INSA Lyon - Ecoles Doctorales

SIGLE	ECOLE DOCTORALE	NOM ET COORDONNEES DU RESPONSABLE
CHIMIE	**CHIMIE DE LYON** **https://www.edchimie-lyon.fr** Sec. : Renée EL MELHEM Bât. Blaise PASCAL, 3e étage secretariat@edchimie-lyon.fr	**M. Stéphane DANIELE** C2P2-CPE LYON-UMR 5265 Bâtiment F308, BP 2077 43 Boulevard du 11 novembre 1918 69616 Villeurbanne **directeur@edchimie-lyon.fr**
E.E.A.	**ÉLECTRONIQUE, ÉLECTROTECHNIQUE, AUTOMATIQUE** **https://edeea.universite-lyon.fr** Sec. : Stéphanie CAUVIN Bâtiment Direction INSA Lyon Tél : 04.72.43.71.70 secretariat.edeea@insa-lyon.fr	**M. Philippe DELACHARTRE** INSA LYON Laboratoire CREATIS Bâtiment Blaise Pascal, 7 avenue Jean Capelle 69621 Villeurbanne CEDEX Tél : 04.72.43.88.63 **philippe.delachartre@insa-lyon.fr**
E2M2	**ÉVOLUTION, ÉCOSYSTÈME, MICROBIOLOGIE, MODÉLISATION** **http://e2m2.universite-lyon.fr** Sec. : Bénédicte LANZA Bât. Atrium, UCB Lyon 1 Tél : 04.72.44.83.62 secretariat.e2m2@univ-lyon1.fr	**Mme Sandrine CHARLES** Université Claude Bernard Lyon 1 UFR Biosciences Bâtiment Mendel 43, boulevard du 11 Novembre 1918 69622 Villeurbanne CEDEX **sandrine.charles@univ-lyon1.fr**
EDISS	**INTERDISCIPLINAIRE SCIENCES-SANTÉ** **http://ediss.universite-lyon.fr** Sec. : Bénédicte LANZA Bât. Atrium, UCB Lyon 1 Tél : 04.72.44.83.62 secretariat.ediss@univ-lyon1.fr	**Mme Sylvie RICARD-BLUM** Institut de Chimie et Biochimie Moléculaires et Supramoléculaires (ICBMS) - UMR 5246 CNRS - Université Lyon 1 Bâtiment Raulin - 2ème étage Nord 43 Boulevard du 11 novembre 1918 69622 Villeurbanne Cedex Tél : +33(0)4 72 44 82 32 **sylvie.ricard-blum@univ-lyon1.fr**
INFOMATHS	**INFORMATIQUE ET MATHÉMATIQUES** **http://edinfomaths.universite-lyon.fr** Sec. : Renée EL MELHEM Bât. Blaise PASCAL, 3e étage Tél : 04.72.43.80.46 infomaths@univ-lyon1.fr	**M. Hamamache KHEDDOUCI** Université Claude Bernard Lyon 1 Bât. Nautibus 43, Boulevard du 11 novembre 1918 69 622 Villeurbanne Cedex France Tél : 04.72.44.83.69 **hamamache.kheddouci@univ-lyon1.fr**
Matériaux	**MATÉRIAUX DE LYON** **http://ed34.universite-lyon.fr** Sec. : Yann DE ORDENANA Tél : 04.72.18.62.44 yann.de-ordenana@ec-lyon.fr	**M. Stéphane BENAYOUN** Ecole Centrale de Lyon Laboratoire LTDS 36 avenue Guy de Collongue 69134 Ecully CEDEX Tél : 04.72.18.64.37 **stephane.benayoun@ec-lyon.fr**
MEGA	**MÉCANIQUE, ÉNERGÉTIQUE, GÉNIE CIVIL, ACOUSTIQUE** **http://edmega.universite-lyon.fr** Sec. : Stéphanie CAUVIN Tél : 04.72.43.71.70 Bâtiment Direction INSA Lyon mega@insa-lyon.fr	**M. Jocelyn BONJOUR** INSA Lyon Laboratoire CETHIL Bâtiment Sadi-Carnot 9, rue de la Physique 69621 Villeurbanne CEDEX **jocelyn.bonjour@insa-lyon.fr**
ScSo	**ScSo*** **https://edsciencessociales.universite-lyon.fr** Sec. : Mélina FAVETON INSA : J.Y. TOUSSAINT Tél : 04.78.69.77.79 melina.faveton@univ-lyon2.fr	**M. Bruno MILLY** Université Lumière Lyon 2 86 Rue Pasteur 69365 Lyon CEDEX 07 **bruno.milly@univ-lyon2.fr**

*ScSo : Histoire, Géographie, Aménagement, Urbanisme, Archéologie, Science politique, Sociologie, Anthropologie

Cette thèse est accessible à l'adresse : https://theses.insa-lyon.fr/publication/2022ISAL0090/these.pdf
© [R. Zhang], [2022], INSA Lyon, tous droits réservés

Acknowledgement

This thesis work is conducted at the Laboratory of Materiaux et Ingénierie et Science and the Centre national de la recherche scientifique for three and a half years. This work would not have been accomplished without the people who gave me much support and assistance. I would like to take this opportunity to express my sincere appreciation.

First of all, I would like to express my profound respect and gratitude to my supervisor, Prof. Karine Masenelli-Varlot, for providing valuable guidance throughout this research. The discussions with her have been a learning experience and have provided another perspective on my results. I sincerely thanks for confirmation and encouragement. She relieved my anxiety and always motivated me.

Second, my deep gratitude goes to my co-supervisor, Dr. Lucile Joly-Pottuz, who always gave me valuable advice and offered her help without reservation when I was in a difficult situation. She has taught me how to carry out the experiment and supplied me with many learning materials.

Working with my supervisors is a valuable experience in life. They were always there when I needed assistance. They taught me data analysis, presentation, and scientific writing with endless patience. I warmly thank them for the suggestions in technical, scientific, professional, and personal fields.

In addition, I would like to express acknowledgment to China Scholarship Council (CSC) for financial support during my Ph.D. period providing a precious opportunity to

Cette thèse est accessible à l'adresse : https://theses.insa-lyon.fr/publication/2022ISAL0090/these.pdf
© [R. Zhang], [2022], INSA Lyon, tous droits réservés

continue my academic study.

Besides my supervisors, I am very grateful to Dr. Jonathan Amodeo, Dr. Tristan Albaret, and Dr. Gaetan Laurens for their contributions to the simulation work and the active discussions with them that led me to a deeper understanding of the experimental results. I am also sincerely grateful to Prof. David Dunstan of Queen Mary University of London for his work and discussion of the section on "Scale Effect." My thanks as well go to Prof. Thierry Epicier, who contributed to the section on EELS experiment and gave a lot of useful advice on the calculation of electron beam dose.

I am particularly grateful to Dr. Lucian Roiban for his training me on ETEM and helping me a lot when I had difficulties with experiments. He also often encouraged and enlightened me. His easy-going and cheerful personality often infects me. My sincere thanks go to Mr. Mimoun Aouine from CNRS, for helping me solve many problems when I'm operating ETEM.

I would like to thank Mr. Thierry Douillard for training me on Ilion, FIB and helping fabricate the indenter. I also would like to thank Ms. Clémentine Fellah for training me on TEM.

I would like to extend my thanks to my colleagues, Akkiz Bekel, Solène Dassonneville, Aslihan Sayilan, Louis-Marie Lebas, and Yangdi Li. Due to the epidemic and building renovations, we didn't work together for long periods, but their mutual concern and smiles make the office ambiance relaxing. Thanks to my Chinese friends in France Zexian Wang, Xiao Peng, Meng Liang, Xiaoting Zhang, Xinyu Li, Yunlong He, Guojian Lv, and Xinyan Zhang, with whom I had a great time in Lyon.

I would also like to take this chance to thank my friends Qiang Wu, Haibo Guo, Yulong Kang and Zhazha, who accompanied me at my loneliest time and gave me a lot of comfort and encouragement. I also want to thank Qiu Qi, who helped me find myself and think

Cette thèse est accessible à l'adresse : https://theses.insa-lyon.fr/publication/2022ISAL0090/these.pdf
© [R. Zhang], [2022], INSA Lyon, tous droits réservés

more about my life.

At last but not least, I would like to express my deepest gratitude to my parents, who always stand behind me and support me. I am grateful to my husband Lie Yang for his unconditional love and care.

Cette thèse est accessible à l'adresse : https://theses.insa-lyon.fr/publication/2022ISAL0090/these.pdf
© [R. Zhang], [2022], INSA Lyon, tous droits réservés

Cette thèse est accessible à l'adresse : https://theses.insa-lyon.fr/publication/2022ISAL0090/these.pdf
© [R. Zhang], [2022], INSA Lyon, tous droits réservés

Abstract

Ceramic materials present excellent mechanical strength and are used in many fields. However, the most detrimental characteristic of ceramics is their brittleness, which restricts their application. Recent investigations have shown that nanoscale ceramic materials display superior plastic deformation than their bulk counterparts. This plastic behavior at the nanoscale might be interesting to improve the ceramic processing either by decreasing the energy needed during the process or by optimizing the microstructure obtained. However, few studies on plastic behavior of ceramic materials have been reported so far.

This study deals with cerium oxides nanocubes with sizes ranging between 20 and 130 nm. We use *in situ* nanocompression tests in Environmental Transmission Electron Microscopy (ETEM) on isolated nanocubes. The cube geometry ensures to test the cube along a known crystallographic direction <001>. During the test, stress/strain curves are obtained from the sensor of the sample holder and coupled with video of the compressed nanoparticle. Due to a reduction effect of the electron beam in the TEM, different structures are tested, from CeO_2 to Ce_2O_3 depending on the experimental conditions (electron dose or presence of gas around the sample).

We conduct compression tests on bixbyite Ce_2O_3 and on fluorite CeO_2. During compression of bixbyite, we observe the formation of perfect dislocations followed by their dissociation into partials with the formation of stacking faults. This mechanism can be compared to what is observed in f.c.c. metals.

On fluorite CeO_2, dislocations appear but rarely dissociate. By using several zone axes, dislocations can be indexed. With our results, the main slip system is identified as

Cette thèse est accessible à l'adresse : https://theses.insa-lyon.fr/publication/2022ISAL0090/these.pdf
© [R. Zhang], [2022], INSA Lyon, tous droits réservés

<110>{111}. CeO_2 also shows a strong size effect on the yield stress. This size effect is discussed using models from the literature and by considering the deformation mechanism.

Cette thèse est accessible à l'adresse : https://theses.insa-lyon.fr/publication/2022ISAL0090/these.pdf
© [R. Zhang], [2022], INSA Lyon, tous droits réservés

Résumé étendu en français

Les matériaux céramiques présentent une excellente résistance mécanique et sont utilisés dans de nombreux domaines. Cependant, la caractéristique la plus préjudiciable des céramiques est leur fragilité, qui limite leur application. Des recherches récentes ont montré que les matériaux céramiques à l'échelle nanométrique présentent une déformation plastique supérieure à celle de leurs homologues à l'état massif. Ce comportement plastique à l'échelle nanométrique pourrait être intéressant pour améliorer le traitement des céramiques, soit en diminuant l'énergie nécessaire au cours du processus, soit en optimisant la microstructure obtenue.

Le premier chapitre de cette thèse présente un état de l'art des propriétés mécaniques des céramiques, avec une attention particulière portée à l'effet de la taille sur les propriétés mécaniques. Comme peu d'études sur le comportement plastique des matériaux céramiques ont été rapportées jusqu'à présent, l'état de l'art inclue aussi plusieurs études effectuées sur les métaux, qu'ils présentent une structure cubique centrée ou une structure cubique à faces centrées.
Au vu de la littérature peu abondante sur la plasticité dans les nano-objets céramiques à température ambiante, et étant donné la grande variété de ses applications, nous avons décidé de focaliser cette étude porte sur des nanocubes d'oxyde de cérium, dont la taille varie entre 20 et 130 nm. Les nanocubes sont testés mécaniquement *in situ* dans un microscope électronique en transmission, car cette technique a montré qu'il était possible à la fois de mesurer la force et le déplacement et de suivre l'évolution de la microstructure dans les nanocubes.

Les caractéristiques principales de l'oxyde de cérium CeO_2 sont détaillées dans le

Cette thèse est accessible à l'adresse : https://theses.insa-lyon.fr/publication/2022ISAL0090/these.pdf
© [R. Zhang], [2022], INSA Lyon, tous droits réservés

deuxième chapitre. Nous présentons tout d'abord sa structure cristalline, avecla position des atomes dans la structure fluorite. La sensibilité sous faisceau électronique de CeO_2 fluorite est ensuite discutée. On retiendra en particulier que la littérature rapporte une réduction de CeO_2-fluorite vers Ce_2O_3-bixbyite sous faisceau.

Une revue de la litérature concernant les grandeurs mécaniques de CeO_2 (dureté, module, module d'Young, module de compressibilité, contrainte à la transition élastique-plastique) sous différentes géométries est ensuite présentée. Pour expliquer la plasticité, une revue des systèmes de glissement dans CeO_2 et d'autres structures fluorite est également donnée. On retiendra que le vecteur de glissement principal est 1/2<110>. En outre, plusieurs études considèrent que les plans {111} sont les plans principaux de glissement dans la structure fluorite. Cependant, d'autres facteurs comme la composition chimique, par exemple le rapport O/U dans UO_2, peuvent avoir une influence sur les plans de glissement.

La dernière partie du chapitre 2 est consacrée à la présentation de la structure cristallographique de la bixbyite et de ses systèmes de glissement. Aucune conclusion claire ne peut être tirée concernant les systèmes de glissement dans la bixbyite et l'évolution de la structure est rarement discutée dans la littérature à cause de sa complexité. On retiendra néanmoins des similarités entre le comportement de CeO_2-fluorite et Eu_2O_3-bixbyite sous irradiation par un faisceau d'électrons.

Dans le troisième chapitre, nous présentons les matériaux et les techniques utilisées. Comme nous utilisons des tests de nanocompression *in situ* en microscopie électronique à transmission environnementale (ETEM) sur des nanocubes isolés, nous présentons tout d'abord le principe de la microscopie électronique en transmission et des tests mécaniques *in situ*. L'obtention de cubes bien dispersés étant une étape très importante, nous détaillons les différentes étapes concernant la préparation du support et le dépôt des nanocubes, fournis grâcieusement par le laboratoire de chimie de l'Ecole Normale Supérieure de Lyon.

Nous donnons ensuite les informations concernant les tests de compression. La géométrie du cube assure de tester le cube le long d'une direction cristallographique connue <001>. L'axe de zone peut être ajusté afin de faciliter le suivi des défauts. Les systèmes de glissement pouvant être activés dans la fluorite sont également listés.

Cette thèse est accessible à l'adresse : https://theses.insa-lyon.fr/publication/2022ISAL0090/these.pdf
© [R. Zhang], [2022], INSA Lyon, tous droits réservés

Enfin, nous détaillons les différentes étapes de traitement des données obtenues pendant les tests. Les courbes de contrainte/déformation sont obtenues à partir du capteur du porte-échantillon et couplées à la vidéo de la nanoparticule comprimée. Le déplacement réel de l'indenteur est mesuré directement sur les vidéos par Corrélation Digitale d'Images (DIC).

Le quatrième chapitre est dédié à l'étude de la fluorite. Les nanocubes initiaux sont tout d'abord caractérisés en terme de structure cristallographique, distribution de taille, type de facettes. Les nanocubes sont également caractérisés après irradiation par le faisceau électronique. Nous observons comme attendu une réduction sous faisceau, qui peut conduire à un changement de phase, de la fluorite vers la bixbyite. Ce changement a cependant été observé uniquement pour certains petits cubes. Nous supposons que la résistance au faisceau de certains cubes est lié au type de facettes. En conclusion de ces tests d'irradiation, nous considérons qu'il est nécessaire de suivre en temps réel la phase cristalline des nanocubes lors de chaque test.

Dans une deuxième partie du quatrième chapitre, nous présentons les résultats de tests de compression effectués sur un nanocube de 62 nm de côté, présentant la structure fluorite. Ces nanocubes sont appelés CeO_2, même si une réduction partielle n'induisant pas de changement de phase peut avoir lieu. Les contrastes correspondant aux dislocations créées pendant le test et celles restant dans les nanocubes après décharge sont analysées. Par comparaison avec les systèmes de glissement qui sont susceptibles d'être activés (facteur de Schmid différent de 0), nous conclusons que les dislocations sont principalement générées dans les plans $\{111\}$. Bien que des dislocations coin et mixtes sont identifiées, les dislocations sont majoritairement de type vis.

Enfin, en dernière partie du chapitre 4, nous nous sommes intéressés à la variation de la contrainte à l'écoulement en fonction de la taille des nanocubes. La contrainte à l'écoulement a été mesurée sur 14 nanocubes et une relation de type $\sigma_y = a + bd^{-c}$ a été trouvée, avec $c = 0.97 \pm 0.15$, ce qui est en accord avec la littérature pour des objets dont la plasticité est régie par la multiplication et le glissement de dislocations. A faible taille, la contrainte à l'écoulement tend à être supérieure à cette loi, ce qui est en accord avec les observations qui montrent un mécanisme de nucléation-dépletion de dislocations,

Cette thèse est accessible à l'adresse : https://theses.insa-lyon.fr/publication/2022ISAL0090/these.pdf
© [R. Zhang], [2022], INSA Lyon, tous droits réservés

avec des étapes de "recuit mécanique".

L'étude de nanocubes présentant une structure bixbyite est présentée dans le cinquième chapitre. Même si la composition en oxygène peut varier, ces cubes sont appelés Ce_2O_3. Au début de ce chapitre, nous utilisons le concept dit "concept d'empilement de couches atomiques" (layered atom stacking concept) pour déterminer les systèmes de glissement possibles dans Ce_2O_3. Pour ce faire, les vecteurs de plus courte périodicité sont déterminés pour les réseaux anioniques et cationiques.

Dans une deuxième partie de ce chapitre, nous présentons les résultats issus d'un test de compression d'un nanocube de 52ñm fortement irradié, présentant la structure bixbyite. Nous observons la formation de dislocations parfaites suivie de leur dissociation en partielles avec la formation de fautes d'empilement. Ce mécanisme peut être comparé à ce qui est observé dans les structures métalliques FCC. Les dislocations sont indexées et un schéma de dissociation est proposé.

Enfin, nous faisons une conclusion générale de ces travaux et proposons plusieurs pistes pour des études futures.

Cette thèse est accessible à l'adresse : https://theses.insa-lyon.fr/publication/2022ISAL0090/these.pdf
© [R. Zhang], [2022], INSA Lyon, tous droits réservés

Table of contents

Liste des écoles doctorales **i**

Acknowledgement **iii**

Abstract **vii**

Résumé étendu en français **ix**

Table of contents **xiii**

List of Figures **xvii**

List of Tables **xxvii**

General Introduction **1**

1 Mechanical properties of submicron-sized ceramics **5**

1.1 Mechanical properties of ceramics 6

1.1.1 Ceramic material applications and significance 6

1.1.2 Mechanical behavior of ceramic materials 10

1.1.3 Plasticity in nano-objects 21

1.2 Size effect on the strength of submicron-sized materials 27

1.2.1 Size effect in metals 27

1.2.2 Size effect in ceramics 30

1.3 General conclusion of Chapter1 31

2 Introduction to cerium oxides **33**

Cette thèse est accessible à l'adresse : https://theses.insa-lyon.fr/publication/2022ISAL0090/these.pdf
© [R. Zhang], [2022], INSA Lyon, tous droits réservés

2.1 Introduction to CeO_2 . . . 33
2.1.1 Structure of CeO_2 . . . 33
2.1.2 Possible structures of CeO_x . . . 34
2.1.3 Electron beam effect on CeO_2 . . . 34
2.2 Mechanical parameters of CeO_2 . . . 36
2.2.1 Slip systems in CeO_2 and other fluorite materials . . . 39
2.3 Introduction to Ce_2O_3 . . . 41
2.3.1 Crystallographic structure of bixbyite . . . 41
2.3.2 Slip systems in bixbyite . . . 42

3 Material and techniques 45
3.1 Transmission electron microscopy (TEM) . . . 45
3.1.1 Principles of TEM . . . 47
3.1.2 Environmental transmission electron microscope (ETEM) . . . 52
3.2 *In situ* mechanical testing methods in TEM . . . 54
3.2.1 Nanocompression TEM sample holder (Hysitron PicoIndenter 95) . 55
3.3 Sample preparation . . . 57
3.4 Data processing . . . 62

4 *In situ* Nanocompression of CeO_2 nanocubes 65
4.1 Characterization of the nanocubes in TEM . . . 65
4.1.1 Characterization of CeO_2 in TEM . . . 65
4.1.2 Electron beam effect on the nanocube structure . . . 68
4.2 Study of the CeO_2 slip systems . . . 74
4.3 Size effect in CeO_2 . . . 85
4.4 General conclusion of Chapter 4 . . . 93

5 *In situ* Nanocompression of Ce_2O_3 nanocubes 95
5.1 Determination of the primary slip system in Ce_2O_3 . . . 95
5.2 *In situ* compression experiments on Ce_2O_3 nanocubes . . . 99
5.3 Discussion of the deformation analysis in Ce_2O_3 . . . 102
5.4 General conclusion of Chapter5 . . . 112

Cette thèse est accessible à l'adresse : https://theses.insa-lyon.fr/publication/2022ISAL0090/these.pdf
© [R. Zhang], [2022], INSA Lyon, tous droits réservés

Conclusion **115**

References **119**

Cette thèse est accessible à l'adresse : https://theses.insa-lyon.fr/publication/2022ISAL0090/these.pdf
© [R. Zhang], [2022], INSA Lyon, tous droits réservés

Cette thèse est accessible à l'adresse : https://theses.insa-lyon.fr/publication/2022ISAL0090/these.pdf
© [R. Zhang], [2022], INSA Lyon, tous droits réservés

List of Figures

1 Magnesium oxide nanocubes present size effect on strength [ISS 21]. 1

1.1 Two kinds of works of art made of ceramic materials 7

1.2 Applications of advanced ceramics in automotive industry 8

1.3 Classification of ceramic materials [REE 88] 9

1.4 Evolution of the market share of different abrasive particle polishing solutions [KIM 18]. 10

1.5 Typical stress-strain curves 11

1.6 Basis of the estimation of the theoretical shear strength, where it is assumed that entire planes of atoms shift simultaneously, one relative to another [MEY 08]. 12

1.7 definition of the angles involved into the computation of the Schmid factor . 15

1.8 (a) Sequence of (100) planes in CeO_2, showing the succession of anion and cations layers. (b) A (110) plane exhibiting neutral charge. (c) (110) plane glide along vector 1/4<110>, with close oxygen ions repelling each other . . 17

1.9 Figure taken from [KAR 87], showing TiO_2 films after bending tests. (a) nanocrystalline TiO_2 film after plastic deformation. The specimen was initially flat. (b) magnified image from (a). After bending, the sample is pre-cracked. (c) Brittle fracture of a TiO_2 single crystal when deformed under the same conditions as in (a). 17

Cette thèse est accessible à l'adresse : https://theses.insa-lyon.fr/publication/2022ISAL0090/these.pdf
© [R. Zhang], [2022], INSA Lyon, tous droits réservés

1.10 Figure taken from [ZHA 13] showing the mechanical response of SiC with different grain sizes subjected to tensile loading. (a–c) Nanocrystalline SiC (NC-SiC) structures with average grain size d = 2, 4 and 6 nm. Grains are shown in different colors. (d–g), Stress-strain curves for NC-SiC with d = 2, 4 and 6 nm, as well as for a-SiC (amorphous SiC) and C-SiC (monocrystal with orientation <100>). Each graph corresponds to a potential (Tersoff-1, Tersoff-2, Tersoff-3 and Vashishta). 18

1.11 Factors affecting the mechanical properties of ceramics[YAN 19]. 19

1.12 compression of a TiO_2 nano-pillar at room temperature. (a) True strain - true stress curve and SEM images at different strains. (b) TEM image showing nanoscale stacking faults and nanotwins. Image taken from [LI 19]. 20

1.13 *In situ* TEM compression of monocrystalline MgO nanocubes. (a) Stress-strain curve for a 140 nm MgO nanocube compressed *in situ*. Five loading-unloading cycles are shown. Black arrows refer to the state at which snapshots were taken. (b)-(e) Images at ϵ = 1.2%, ϵ = 18.7%, ϵ=49.7%,ϵ = 78.9%. Figure taken from [ISS 15]. 21

1.14 Results of compression experiments on Ni single-crystal microcolumns of different diameters. Figure taken from [UCH 04] 22

1.15 summary of the different mechanisms causing size effects 24

1.16 Examples of stress-strain curves obtained from two loading modes 24

1.17 Size effect phenomenon in f.c.c. and BCC metals. 29

1.18 Comparison of the size effect mechanism in b.c.c. and f.c.c. metallic single crystals [GRE 08]. 29

2.1 (a) Fluorite unit cell in the case of CeO_2. (b) Details of the oxygen cube, which includes one cerium atom. (c) Ce tetrahedral structure, which includes one oxygen ion in the CeO_2 unit cell. 34

2.2 Calculated displacements cross-sections for Ce-and O-sublattices in CeO_2 based on Bethe's formula [JIA 16] 36

2.3 EELS spectra of cerium oxides with different oxygen contents [GAR 99] . . 37

Cette thèse est accessible à l'adresse : https://theses.insa-lyon.fr/publication/2022ISAL0090/these.pdf
© [R. Zhang], [2022], INSA Lyon, tous droits réservés

2.4 Stress-strain curve of 8 nm polyhedral nanoparticles; fully oxidized CeO_2 (black curve) and reduced $CeO_{1.9}$ (red curve) [CAD 16]. 38

2.5 (a) Fluorite structure in the case of CeO_2. (b) Ideal bixbyite structure in the case of Ce_2O_3. (c) Real bixbyite structure of Ce_2O_3. (d) Real bixbyite structure with one unit cell of Ce_2O_3.) 41

3.1 Temporal and spatial resolution of several microscopy techniques 47

3.2 Sketch of the two main TEM modes: diffraction mode (left) and imaging mode (right) [WIL 96]. 49

3.3 schematic diagrams of Bragg's law 50

3.4 Examples of cubic diffraction patterns. (a) Top: Area-selected diffraction pattern of the Ti δ-FCC phase. Bottom: dark field image using the g-vector [220][LI 18]. (b) Top: Diffraction pattern of the CeO_2 nanocubes used in this work. Bottom: Crystal structure with the same orientation (zone axis [100]). (c) Top: Diffraction pattern of the Ce_2O_3 nanocubes used in this work. Bottom: Crystal structure with the same orientation (zone axis [100]). 51

3.5 Diagrams of bright-field imaging and dark-field imaging[JAV 18] 51

3.6 Schematic Diagram of an Environmental Transmission Electron Microscope [HAN 16] 53

3.7 Picture of the FEI Titan Environmental Transmission Electron Microscope of the CLYM 53

3.8 Picture of the PI95 holder with an enlarged view of the front of the sample rod 56

3.9 Schematic diagram of the working principle of the PI-95 transducer 57

3.10 Schematic Diagram of the sample preparation and sample mounting used to perform *in situ* mechanical tests in TEM 58

3.11 Comparison of the sapphire substrate surfaces before and after argon beam polishing 59

Cette thèse est accessible à l'adresse : https://theses.insa-lyon.fr/publication/2022ISAL0090/these.pdf
© [R. Zhang], [2022], INSA Lyon, tous droits réservés

3.12 Scheme of the experimental setup. (a) Picture of the front end of the TEM holder with a diamond indenter. (b) Scheme of the compression experiment with electron beam direction [100] and (c) Scheme of the compression experiment with electron beam direction [110]. 60

3.13 Schmid factors for different slip systems. 61

3.14 Comparison of stress-strain curves before and after DIC. The left graph shows the original stress-strain curve, the right one is the curve after DIC processing. 63

4.1 The images from left to right are: TEM images, diffraction patterns (DP) and high-resolution TEM (HRTEM) images of CeO_2 nanocubes along different zone axes(Top is from ZA [100], bottom is from ZA[110]). Both zone axes can be used for the analysis of the same cube only if one zone axis is observed with a tilt of the sample holder of -20° 66

4.2 STEM images at different magnifications. (a) low magnification image with particle size distribution. (b) nanocubes observed along the [100] zone axis. (c) High magnification image, reaching the atomic resolution, of the cube at the botton left part of image (b). The insets confirm the distance of the (100) and (110) planes 67

4.3 The distributions of planes {001} and {110} differ between small and large cubes. 68

4.4 effect of the same irradiation duration (20 s) on different CeO_2 nanoparticles. In the left square, the particles did not exhibit any phase change while on the right one, a structural change from CeO_2 to CeO_x($1.5 \leq x < 2$) is observed. 69

4.5 Dependence of e-beam dose rate on the TEM magnification 70

4.6 CeO_2 particles of several sizes irradiated with different electron beam doses. The black dots represent CeO_2 that retains its structure (fluorite, Fm-3m space group) after irradiation. The red dots present a phase change from fluorite to bixbyite Ia-3. 71

Cette thèse est accessible à l'adresse : https://theses.insa-lyon.fr/publication/2022ISAL0090/these.pdf
© [R. Zhang], [2022], INSA Lyon, tous droits réservés

4.7 a. Selection of five regions including (011) and (011) planes. Region 1 and region 5 include (001) and (011) facets, and the other regions contain only (001). b. Diffraction patterns corresponding to each region after the same time of e-beam irradiation. Region 1 and 5 maintain the original fluorite structure, while other regions undergo a phase change. 72

4.8 Oxygen content x, measured by EELS, in a CeO_x nanocube, as a function of the electron dose. (EELS experiments conducted by Thierry Epicier) . . 73

4.9 Dark-field images of a CeO_2 cube before and after compression. ZA=[110] and g-vector [002]. The stress-strain curve is on the right with corresponding strain and yield stress. 75

4.10 Dark-field images acquired when tilting the cube around the direction [001], at 0°, 10°, 2°, 30° and 45° degree from the zone axis [110]. Below the images are the corresponding crystal structures. The direction of the dislocation lines are marked. 75

4.11 Compression test of CeO_2 along [001]. Cube size: 62 nm (a) Force-time (blue line) and displacement-time (red line) curves. b and c indicate the beginning and the end of the compression test. (b) bright field image of the cube before compression (corresponding to position b on the curve) with the corresponding diffraction pattern showing a zone axis close to [100]. (c) bright field image of the cube after compression (position c on the curve). 77

4.12 Stress-strain curve of the cube before and after DIC processing. 78

4.13 Stress-strain curve derived from the test presented in Fig 4.11. There are four stress drop periods marked by a roman number and a roman number' (like for instance I and I'). The snapshots corresponding to the points marked by roman numbers are also given. 79

4.14 List of the slip systems that can be activated in CeO_2, with the corresponding values of the Schmid factor. For each slip system, the direction of the dislocation lines for screw and edge dislocations are indicated. 80

4.15 Snapshots of the CeO_2 nanocube tested in Figure 4.13, from the original state to stage I. The dislocations are traced out with dotted lines and the corresponding schematic diagrams are depicted below the snapshots. 81

Cette thèse est accessible à l'adresse : https://theses.insa-lyon.fr/publication/2022ISAL0090/these.pdf
© [R. Zhang], [2022], INSA Lyon, tous droits réservés

4.16 Snapshots of the CeO_2 nanocube tested in Figure 4.13, from the I' to stage II. The dislocations are traced out with dotted lines and the corresponding schematic diagrams are depicted below the snapshots. 82

4.17 Snapshots of the CeO_2 nanocube tested in Figure 4.13, from the II' to stage III. The dislocations are traced out with dotted lines and the corresponding schematic diagrams are depicted below the snapshots. 83

4.18 Snapshots of the CeO_2 nanocube tested in Figure 4.13, from the III' to stage IV. The dislocations are traced out with dotted lines and the corresponding schematic diagrams are depicted below the snapshots. 84

4.19 (a-f) Video snapshots extracted of the CeO_2 nanocube tested in Fig 4.13, during the stress drop between stages III and III'. (g) Schematic representation of corresponding dislocation lines. The main dislocation slip plane is (111). 85

4.20 Stress-strain curves of CeO_2 nanocubes of different sizes. All compression directions are [001]. The grey arrows indicate the yield points. The curves in red were obtained after measurement of the real displacement by DIC. DIC could not be successfully performed on the other ones, therefore they are left in black. 87

4.21 Stress-strain curves of CeO_2 nanocubes of different sizes. All compression directions are [001]. The grey arrows indicate the yield points. The curves in red were obtained after measurement of the real displacement by DIC. DIC could not be successfully performed on the other ones, therefore they are left in black. 88

4.22 Dependence of the yield stress on the nanocube size. Labeled beside each dot is the strain corresponding to the yield stress. Black is from the original data and red is from the DIC data. 90

Cette thèse est accessible à l'adresse : https://theses.insa-lyon.fr/publication/2022ISAL0090/these.pdf
© [R. Zhang], [2022], INSA Lyon, tous droits réservés

4.23 Dependence of the elastic strain (yield stress divided by the Young's modulus at bulk, Y = 360 GPa) and the normalized size (nanocube size d divided by the lattice parameter $a_0 = 0.54$ nm). The blue dots come from the experiment, and the orange dots come from simulation results obtained by G. Laurens and T. Albaret at ILM. The blue curve is an empirical curve computed for GaInAs (0.8nm/h) and the green curve is the theoretical curve for Frank-Read dislocation sources (5b/h, with $b = \frac{1}{2}\frac{0.54}{\sqrt{2}}$ nm in our case). The orange curve is the result of the fit with the function a+bx^c, with $c = 0.97 \pm 0.15$. Work performed by Prof. David DUNSTAN from the Queen Mary University in London. 91

4.24 Plastic deformation mechanisms in CeO_2 92

5.1 (a) Kagome lattice of cations in the (111) plane of spinel $MgAl_2O_4$. The characteristic kagome star is shown in yellow.[SIC 06] (b) {111} Kagome lattice in the (111) plane of spinel $MgAl_2O_4$, with all cations and anions. A Perfect ½<110> Burgers vector is shown as well as its possible dissociation schemes [MIT 99] [ESP 12] 96

5.2 (a) Cation arrangement in the {111$_r$*brace* planes in bixbyite, with a triangular lattice (b) Anions arrangement in the {111} planes in bixbyite. (c) Kagome pattern in yellow, revealing a Y-type or wishbone configuration of anions and vacancies. Zone axis [1-11] [SIC 06]. 97

5.3 (100), (110) and (111) planes of the bixbyite structure of Ce_2O_3. The upper row shows the shortest periodicity vectors for the cerium cations, indicated by red arrows. The bottom row shows the shortest periodicity vectors for the oxygen anions, indicated by red arrows. 98

5.4 Initial state of a 52 nm Ce_2O_3 cube before compression. (a) Image of the cube and indenter before compression. (b) High resolution image of the region of interest indicated with a red square in image (a). (c) is DP of the same region of interest. ZA=[110] 99

Cette thèse est accessible à l'adresse : https://theses.insa-lyon.fr/publication/2022ISAL0090/these.pdf
© [R. Zhang], [2022], INSA Lyon, tous droits réservés

5.5 *in situ* generation of a stacking fault in a 52 nm Ce_2O_3 nanocube. (a) Before loading, there is no defect in the cube. (b) Upon loading, a dislocation is created. (c) A stacking fault is created through dissociation of the dislocation 100

5.6 Burgers circuit of the dislocation identified in Fig 5.5b. The circuit is drawn in yellow. The red arrow indicates the projected Burgers vector. The inset shows the corresponding DP and filtered image and filtered using the g-vector 2-22. The frame corresponds to the time 0.52 s. 101

5.7 Stacking fault generated in the Ce_2O_3 cube compressed *in situ* in Fig 5.5. The frame corresponds to the time 1,2s. Two Burgers circuits are drawn in yellow at both ends of the stacking fault. The projected Burgers vectors of the partials are shown in red. The insets give the DP and images filtered with the g-vectors 2-22 (top filtered image) and -222 (bottom filtered image). 102

5.8 HRTEM images of the Ce_2O_3 cube compressed *in situ* in Fig 5.5, with filtered images of the region of interest indicated by white rectangles. (a) stacking fault 1 (SF1) identified by the white arrow. (b) stacking fault 2 (SF2) created near the SF1. A nanotwin is observed between both stacking faults. (c) a new stacking fault 3 (SF3) is created between SF1 and SF2 and the nanotwin is broken. 103

5.9 (a) Scheme of the projected dislocation vector, determined from the TEM image in Fig 5.6. The red dashed line corresponds to the dislocation direction. The red plane corresponds to (110). (b) all possible slip systems, which have their projected vector on the plane (110) equal to [1-12]. The black solid line is the slip vector and the orange plane is the slip plane. . . . 104

5.10 Determination of the real Burgers vector for the perfect dislocation observed during the *in situ* compression of Ce_2O_3 in Fig 5.6. 105

5.11 Determination of the real Burgers vector for the partial dislocations observed during the *in situ* compression of Ce_2O_3 in Fig 5.7. 106

5.12 Schematic diagram illustrating the dissociation in (-111) plane of the 1/4[101] perfect dislocation into the partials 1/12[211] and 1/12[1-12]. 107

5.13 Oxygen ions arrangement in the (1-11) plane of Ce_2O_3. (3X unit cell) . . . 107

Cette thèse est accessible à l'adresse : https://theses.insa-lyon.fr/publication/2022ISAL0090/these.pdf
© [R. Zhang], [2022], INSA Lyon, tous droits réservés

5.14 Evolution of the ratio τ_N/τ_P (critical shear stress for the nucleation of a perfect 1/4 <110> dislocation divided by the critical shear stress for the nucleation of a partial 1/12 <112> dislocation) with the sample size D. . . 110

Cette thèse est accessible à l'adresse : https://theses.insa-lyon.fr/publication/2022ISAL0090/these.pdf
© [R. Zhang], [2022], INSA Lyon, tous droits réservés

Cette thèse est accessible à l'adresse : https://theses.insa-lyon.fr/publication/2022ISAL0090/these.pdf
© [R. Zhang], [2022], INSA Lyon, tous droits réservés

List of Tables

1.1 Slip systems in f.c.c. and b.c.c. metal. 14

2.1 Some of the possible phases in Ce-O system 35
2.2 Mechanical parameters of CeO_2 38
2.3 crystal structure of fluorite CeO_2 and bixbyite Ce_2O_3 42
2.4 Slip systems reported in the literature for the bixbyite structure. 43
2.5 Comparison of the plasticity in the fluorite and bixbyite structures, found in two works [DIN 16] [NIN 90], with the formation of locked <110> dislocations 44

3.1 Features of PI 95 holder provided by Bruker/Hysitron 55

5.1 Shortest periodicity vectors and their magnitudes in Ce_2O_3. 97
5.2 Values of the parameters used for the computation of γ, τ_N and τ_P for bixbyite Ce_2O_3. μ is the shear modulus. D is the sample size. b_N and b_P are the magnitudes of the Burgers vectors of 1/4 [110] perfect dislocations, and 1/12[1-12] partial dislocations, respectively. d is the distance between two partial dislocations. γ is the stacking fault energy. τ_N is the critical shear stress required to generate a 1/4 [110] perfect dislocation and τ_P is critical shear stress required to generate a 1/12[1-12] partial dislocation. . . 109
5.3 Updated values of γ, τ_N and τ_P for bixbyite Ce_2O_3, when the distance d between partials is changed to 0.806 nm (other parameters D, b_N, b_P unchanged). 111

Cette thèse est accessible à l'adresse : https://theses.insa-lyon.fr/publication/2022ISAL0090/these.pdf
© [R. Zhang], [2022], INSA Lyon, tous droits réservés

Cette thèse est accessible à l'adresse : https://theses.insa-lyon.fr/publication/2022ISAL0090/these.pdf
© [R. Zhang], [2022], INSA Lyon, tous droits réservés

General Introduction

Ceramic materials have exceptional mechanical strength and are used in a variety of applications. However, the natural properties of bulk ceramic materials, which are very brittle, have prevented their widespread use up to now. So it has become increasingly important to improve the mechanical properties of ceramics.

It has been found that nano-scale ceramic materials exhibit superior plasticity at room temperature. Moreover, they may show a clear size effect as some metallic materials, as shown in Fig1 in the case of MgO [ISS 21]. However, there are relatively few studies on the nanomechanics of ceramic materials: the deformation mechanisms remain to be determined and may differ from those of metals because of the presence of charged planes in ceramics. The size effect remains also a pending issue. Ceramic processing, especially compaction before sintering, could benefit from a better understanding of such properties.

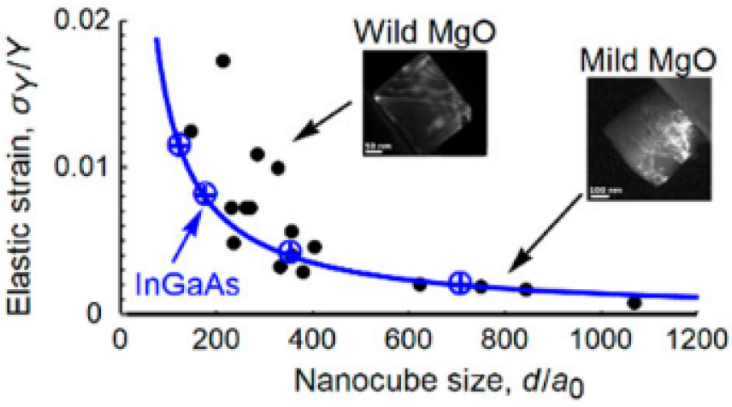

Figure 1 – Magnesium oxide nanocubes present size effect on strength [ISS 21].

In situ mechanical experiments enable investigating the deformation mechanism of nanoscale materials by observing dynamical processes in real time and by obtaining a

Cette thèse est accessible à l'adresse : https://theses.insa-lyon.fr/publication/2022ISAL0090/these.pdf
© [R. Zhang], [2022], INSA Lyon, tous droits réservés

one-to-one connection between mechanical characteristics and microstructure. With the improvement of *in situ* quantitative mechanical testing devices in the last decades, a series of notable advancements in this field has occurred. By performing quantitative tensile or compression tests on various micro- and nano-scale particles, nanowires, and nanopillars in scanning electron microscopy (SEM) and transmission electron microscopy (TEM), extensive research on the size effects and deformation mechanisms of micro- and nano-scale materials has resulted in a new understanding of the mechanics underlying these materials[OH 09][OH 07].

This PhD work is a continuation of the work of two previous PhDs, focused on the development of TEM *in situ* nanocompression experiments of ceramic nanoparticles and its application to the study of alumina [CAL 14][ISS 18] and magnesium oxide [ISS 15]. This work is also part of the MACAO ANR project gathering 3 different teams, and focused on the improvement of the measurements of mechanical properties at small scales, using *in situ* TEM, Brillouin spectroscopy and numerical simulations. In this context, we tested cerium oxides nanocubes, which ranged in size from 20 to 130 nm. Cerium oxides is an important ceramic material that is used as abrasive particles in the manufacturing of semiconductors because it has good mechanical properties. It is also used as a good catalyst in fuel cells, environmental chemistry, and medicine, among other fields.

The dissertation consists of 5 chapters.

In the first one, we provide general information from the literature regarding ceramic materials and their mechanical properties.

The second chapter is focused on cerium oxide and describes two crystallographic phases of interest, as well as pieces of information found in the literature regarding the slip systems.

A third chapter summarizes details regarding the conditions used for sample preparation, *in situ* TEM experiments and data processing.

The results of the compression experiments are given and analyzed in the fourth and fifth chapters:

— The fourth chapter is focused on CeO_2. However, we have to take into account the fact that CeO_2 is sensitive to the electron beam. When CeO_2 is extremely reduced,

Cette thèse est accessible à l'adresse : https://theses.insa-lyon.fr/publication/2022ISAL0090/these.pdf
© [R. Zhang], [2022], INSA Lyon, tous droits réservés

the structure is transformed from the fluorite structure to the bixbyite structure of Ce_2O_3. Conditions allowing the preservation of the fluorite structure are discussed. Afterwards, we present quantitative nanocompression on CeO_2 cubes The activated slip system is identified, as well as the type of dislocation. The variation of the yield strength with the nanocube size is then summarized and analyzed.

— The fifth chapter deals with compression results on irradiated nanocubes, that is to say bixbyite Ce_2O_3. The main slip system of Bixbyite has been rarely reported because of its complexity. Thus we apply the layered atom stacking concept to determine the possible slip systems in Ce_2O_3. We then show a high-resolution *in situ* video and evidence the nucleation of a perfect dislocation. It is then dissociated into two partial dislocations. The Burgers vectors are determined and a dissociation mechanism is proposed. Dislocation dissociation and stacking fault formation in bixbyite Ce_2O_3 is then discussed.

Finally, the general conclusion summarizes the main findings obtained in this dissertation, and perspectives are given.

Cette thèse est accessible à l'adresse : https://theses.insa-lyon.fr/publication/2022ISAL0090/these.pdf
© [R. Zhang], [2022], INSA Lyon, tous droits réservés

Cette thèse est accessible à l'adresse : https://theses.insa-lyon.fr/publication/2022ISAL0090/these.pdf
© [R. Zhang], [2022], INSA Lyon, tous droits réservés

Chapter 1

Mechanical properties of submicron-sized ceramics

This chapter begins with a short introduction presenting the importance of ceramics in human life from ancient times to nowadays. A typical mechanical behavior of macroscopic ceramic materials is first presented. In contrast to metallic materials, ceramic materials usually exhibit high strength and low toughness. However, it has been found that when the characteristic size of bulk ceramic materials decreases, plasticity increases and exhibits the same size effect as the one observed for small size metals:" the smaller the stronger". When the size of metal samples is reduced to the micro-nano scale, they exhibit a different mechanical behavior from the one of bulk samples. Since a number of studies have been conducted to investigate the mechanical properties of metal materials, we present some work on the micro-nano scale metals and summarize the unique mechanical properties they exhibit in the second part of this chapter. In the third part we focus on the size effect. Based on existing research on the mechanical behavior of small-scale metals, this PhD work is an exploration of the mechanical behavior of small-scale ceramics, which has not been well studied.

Cette thèse est accessible à l'adresse : https://theses.insa-lyon.fr/publication/2022ISAL0090/these.pdf
© [R. Zhang], [2022], INSA Lyon, tous droits réservés

1.1 Mechanical properties of ceramics

1.1.1 Ceramic material applications and significance

Ceramic material are essential in human life and modernization. After metals, they are one of the most important class of material that people pay much attention to. The primary usage of ceramics can be dated back to about 26,000 years ago, when most of ceramic objects were made by clay. Clay is a mixture of aqueous aluminosilicate and rocks which is composed of minerals, quartz, carbonate and small amounts of magnesium, iron, sodium, calcium and other elements. Mixed with water, clay can be easily shaped and the material obtained after drying presents good hardness. So at those times, clay was often used for the fabrication of containers, or as raw materials for houses. Afterwards, people found clay can be harder after firing. This kind of products, called pottery, were the most common living utensils at that time. Fig 1.1a shows potteries from early times. Due to the advancement of ceramic processing technology and the combination with colored glazes, ceramic products changed gradually to works of art. Fig 1.1b is a porcelain vase made between 1736 and 1796. From pottery to porcelain, each ancient work of art has witnessed people's exploration of ceramics. The usage of ceramics in industry began during the Industrial Revolution. Although steel was the dominant material during this period, ceramics were used in numerous applications because of their enhanced properties when compared with metals. For example, clay with an increased Al_2O_3 content has a high melting point and is therefore suitable as main material in furnace used to melt metals. In the 15th century, ceramic furnaces could already reach temperatures up to 1500°C. Nowadays, Al_2O_3 is still one of the most popular refractory materials due to its outstanding high temperature resistance [PLE 18].

The first porcelain insulator was invented in 1909 by Edison Electric Company. It opened advanced technologically fields of application for ceramic materials. In the 1970s, as the ceramic engine was developed, researchers made progress in the study of ceramic materials. From the technical point of view, ceramics have been able to basically meet the requirements of various harsh conditions. Take applications of advanced ceramics in cars as an example, as shown in Fig 1.2: advanced ceramics have been basically used in all automotive parts to reduce mass, pollution from oil and gas, and improve the service time

Cette thèse est accessible à l'adresse : https://theses.insa-lyon.fr/publication/2022ISAL0090/these.pdf
© [R. Zhang], [2022], INSA Lyon, tous droits réservés



(a) Pottery from 2500 BC



(b) Chinese porcelain produced between 1736 and 1796

Figure 1.1 – Two kinds of works of art made of ceramic materials

of high wear parts. Nowadays, products made of ceramics play a significant role in many fields, among which additive manufacturing [TRA 14], electrical engineering [GUI 19], environmental engineering [LIN 19].

Why do ceramics have high melting points and high hardnesses? Ionic bonds, covalent bonds and metallic bonds are the three main types of chemical bonds. Ceramics consist mainly of inorganic non-metallic compounds, in which atoms connect to each other with covalent and ionic bonds. The covalent bond is the strongest one, so materials with covalent bonds normally present high hardness and good structure stability. Moreover, as the electrons shared by neighboring atoms are not free to move, ceramics have good electrical insulation, and poor heat conductivity.

According to their chemical composition, ceramics can be divided into two categories: oxidic ceramics and non-oxidic ceramics (Fig 1.3)[REE 88]. Silicon ceramics as natural raw materials are included into traditional ceramic materials. Apart from this classification, advanced ceramics are usually divided into two categories according to their applications: functional ceramics and structural ceramics. Functional ceramics are mainly used for their non-mechanical properties. They are usually developed for one or several functions, such as piezoelectricity, thermoelectricity, piezomagnetism, etc. Functional ceramics have been

Cette thèse est accessible à l'adresse : https://theses.insa-lyon.fr/publication/2022ISAL0090/these.pdf
© [R. Zhang], [2022], INSA Lyon, tous droits réservés

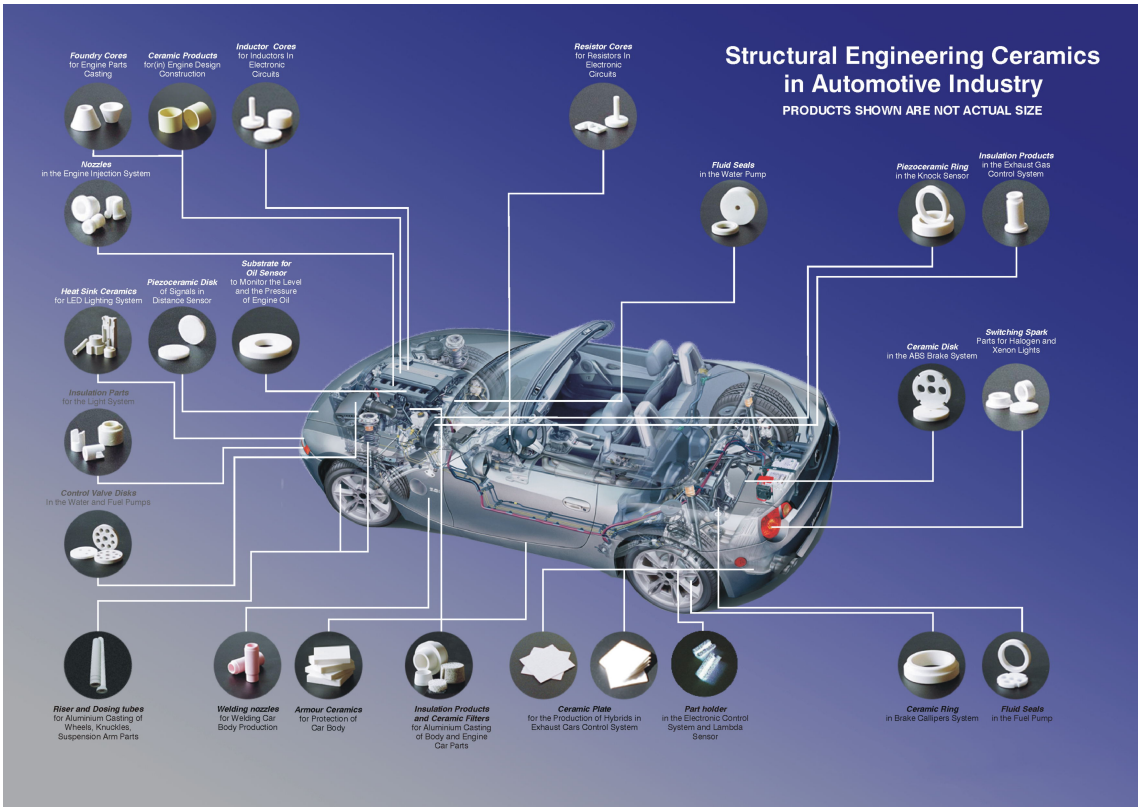

Figure 1.2 – Applications of advanced ceramics in automotive industry

.

widely used in energy, electronics, sensing, infrared technology and other fields. Structural ceramics present good properties, among which high strength, high elastic modulus, high temperature resistance, high corrosion resistance, and so on. Nowadays, many research efforts are focused on the synthesis of more applicable ceramics. For that purpose, it is necessary to analyze their properties and relate them with their microstructure.

Among these advanced ceramic materials, rare-earth oxides are gradually gaining interest in highly technological applications and some special fields. They are composed of rare-earth elements (REEs), which have different chemical properties from the main group elements. There are 17 different REEs including scandium, yttrium and lanthanides. Their electronic layer structures are basically the same for the outermost and second outer layers, with only different numbers of electrons in the 4f orbitals. However, the energy levels are similar, so their properties are very similar. 4f orbitals are wrapped inside 5d, 6s orbitals, which have little effect on the chemistry. However, as the atomic number increases

Cette thèse est accessible à l'adresse : https://theses.insa-lyon.fr/publication/2022ISAL0090/these.pdf
© [R. Zhang], [2022], INSA Lyon, tous droits réservés

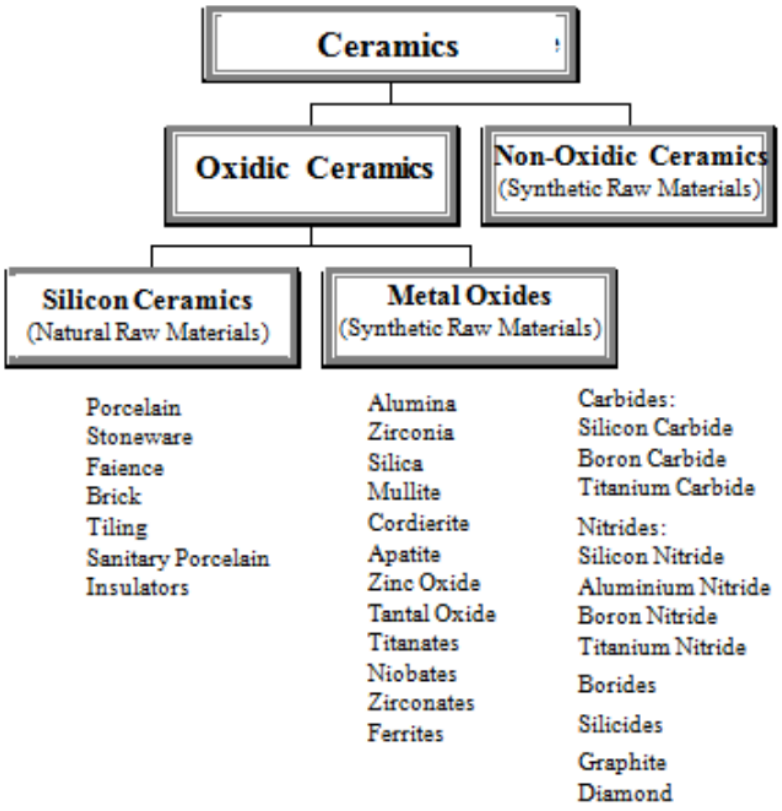

Figure 1.3 – Classification of ceramic materials [REE 88]

(for example in lanthanides, from Lanthanum to Lutetium), the extra electrons will be arranged into seven different 4f orbitals. When the number of electrons in the level 4f is below or equal to 7, every electron occupies one orbital and the system energy is the lowest. However, when the number of electrons increases, electrons need to pair to each other and share orbitals. This results in an increase of the system energy and the system can easily be excited. This gives REEs some catalytic, electronic, magnetic properties that differ from those obtained with other elements.

Cerium (Ce) is one of the most interesting REEs. In principle, it is trivalent and there is a unique electron in a 4f orbital. But the electron often leaves the atom, letting all 4f orbitals available. As a consequence, tetravalent cerium is also stable. This unique chemical structure makes Ce a remarkable catalyst material due to its easy transition between trivalent and tetravalent states.

Cette thèse est accessible à l'adresse : https://theses.insa-lyon.fr/publication/2022ISAL0090/these.pdf
© [R. Zhang], [2022], INSA Lyon, tous droits réservés

Cerium oxides have been widely used in various applications, among which solid-oxide fuel cells(SOFC), oxygen sensors, solar cells. In addition to their excellent chemical properties, cerium dioxide particles can also be used as abrasive slurry in chemical mechanical polishing (CMP), a key process in semiconductor industry. As indicated in Fig 1.4, the market share of ceria gradually increases due to its excellent properties.

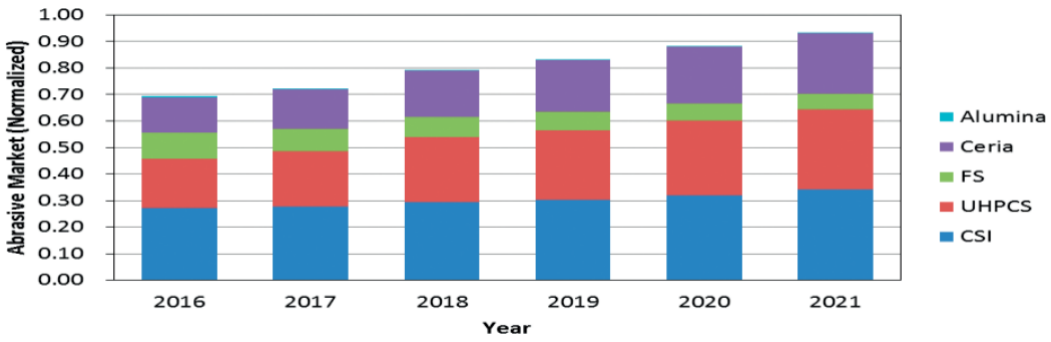

Figure 1.4 – Evolution of the market share of different abrasive particle polishing solutions [KIM 18].

1.1.2 Mechanical behavior of ceramic materials

Fig 1.5a shows the typical stress-strain curve of a metal material obtained from a tensile test. In the stress-strain curve, the abscissa is the strain (ϵ), which measures the amount of deformation. It can be calculated from the displacement changes in the deformed direction divided by the original length ("engineering strain"). The ordinate is the stress (σ), which can be expressed as the force divided by the original area upon which the force is applied ("engineering stress"):

$$\varepsilon_{eng} = \frac{L - L_0}{L_0}$$

It is worth mentioning that strain and stress are respectively called here "engineering strain" and "engineering stress", and are different from "true strain" and "true stress". The true stress is defined as the force divided by the instantaneous cross-section area and the true strain is computed as the instantaneous length divided by the initial length.

Whatever the definition of strain and stress (engineering or true ones), there are three

Cette thèse est accessible à l'adresse : https://theses.insa-lyon.fr/publication/2022ISAL0090/these.pdf
© [R. Zhang], [2022], INSA Lyon, tous droits réservés

stages in the whole deformation:

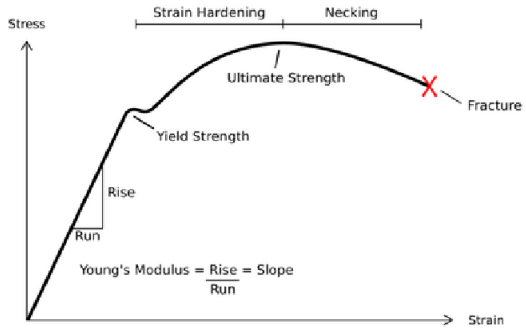

(a) Model stress-strain curve showing various stages of deformation [MAN 15]

.

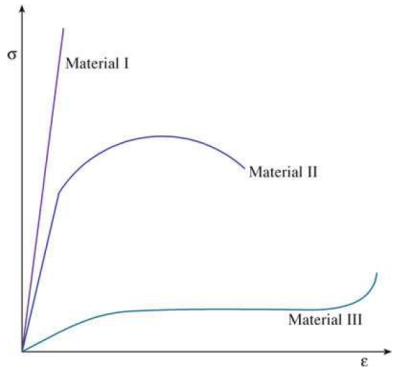

(b) Strain-stress curves for three classical kinds of material. Material I: ceramics, Material II: metals, Material III: elastomers [YAN 19].

Figure 1.5 – Typical stress-strain curves

- **Stage I - Elastic stage**: The elastic deformation corresponds to the region at low strain and stress. At this stage, strain and stress comply with Hook's law and the curve is a straight line. The deformation is reversible, as it is due to bond stretching or bending. The Young's modulus is a mechanical parameter that is used to quantify the elasticity of a material. It is equal to the slope of the stress-strain curve in the elastic stage. The Young's modulus is only related to the material chemical composition and structure, and reflects an inherent property of the material. This elastic stage ends with the yield point, marked as "Yield Strength" on the curve.

- **Stage II - Plastic stage**: After the yield point, the material undergoes permanent deformation. This irreversible deformation is characterized by the fact that bonds between atoms are broken and atoms layers slide. Fig 1.6a-d is a schematic diagram of an ideal shearing process. When the upper atom layer is right on the top of the lower atom layer, there is a strong repulsion between atoms. Fig 1.6e shows the shear stress needed to slide the upper atom layer. It is periodic, with b the distance for which the shear stress is null again. When the upper atom layer moves by the quantity b, it comes back to an equilibrium position. b is called the Burgers vector.

Cette thèse est accessible à l'adresse : https://theses.insa-lyon.fr/publication/2022ISAL0090/these.pdf
© [R. Zhang], [2022], INSA Lyon, tous droits réservés

When the displacement is close to b/4, the corresponding shear stress represents the theoretical shear strength of the material. The theoretical shear strength can be calculated using the following formula:

$$\tau = \tau_b \sin \frac{2\pi x}{b}$$

Where τ is the shear stress, τ_b is the theoretical shear stress, x is the displacement and b is the Burgers vector. The theoretical yield stress is equal to the theoretical shear strength. However, the shear stress obtained from experiments is much lower than the theoretical shear stress. Take Aluminum as an example [COU 05]: the theoretical shear strength is close to 9 GPa, but the shear strength measured in experiments is 7.8×10^{-4} GPa. The discrepancy between the theoretical and experimental values is attributed to movement of defects, such as dislocations.

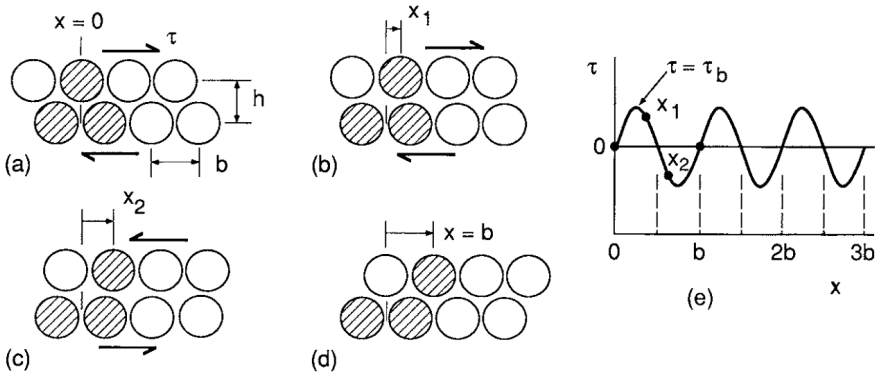

Figure 1.6 – Basis of the estimation of the theoretical shear strength, where it is assumed that entire planes of atoms shift simultaneously, one relative to another [MEY 08].

After the yield stage, the density of dislocations is sharply increased. Dislocations and jogs originating from interactions between dislocations can also be obstacles for dislocation sliding. Residual stress is generated inside the material, which can supply resistance to continuous deformation. This effect may make the tensile stress rise again. If unloaded at this stage, the elastic deformation disappears and the unloading curve is parallel to the elastic stage. If it is reloaded after unloading, the elastic phase line of the material is lengthened, the yield strength is significantly

Cette thèse est accessible à l'adresse : https://theses.insa-lyon.fr/publication/2022ISAL0090/these.pdf
© [R. Zhang], [2022], INSA Lyon, tous droits réservés

increased, and plasticity is reduced. This phenomenon, called strain hardening or work hardening, can be used to increase the strength of a material. The stress of the tensile curve reaches the strength limit, which is the maximum resistance of the material to uniform plastic deformation, and is the sign that the material enters the necking stage.

- **Stage III - Necking stage**: After the stress reaches the strength limit, local deformation begins to occur at the weakest point on the sample surface, resulting in a sharp necking of the local section of the sample. A rapid decrease on the stress may occurs before the sample fails.

The curve displayed in Fig 1.5a was obtained from a tensile test. The compression curve would be slightly different. Indeed no necking behavior happens, and the final failure often takes the form of slipped or collapsed structures. Moreover, Fig 1.5a and the discussion above refer to metal samples. Fig 1.5b presents different typical mechanical curves for three classical materials tested at room temperature. The curve from Material II shows a typical stress-strain curve of a metal and is similar to the curve presented in Fig 1.5a. Material I is a ceramic material and its stress-strain curve shows no yield point and no plastic stage. Contrarily to metal materials, ceramic materials normally show brittle behaviors when loaded at room temperature. This can be attributed to the fact that less mobile dislocation are available to undertake plasticity.

We have seen that plastic deformation in metals is attributed to dislocation movements and multiplication.

From a general point of view, the basic types of dislocations in crystals are classified into edge dislocation and screw dislocation. The Burgers vector and the dislocation line of the edge dislocation are perpendicular to each other, and the Burgers vector and the dislocation line of the screw dislocation are parallel to each other. In fact, dislocations are often a combination of two basic types, called mixed dislocations, and the angle between the Burgers vector and the dislocation line is between 0° and 90°. Dislocations can only move on crystallographic planes that contain the Burgers vector and dislocation line. These special crystallographic planes are called slip planes, and the direction of the Burgers vec-

Cette thèse est accessible à l'adresse : https://theses.insa-lyon.fr/publication/2022ISAL0090/these.pdf
© [R. Zhang], [2022], INSA Lyon, tous droits réservés

tor is defined as the slip direction. The combination of slip plane and slip direction is called a slip system. Since the slip plane and the slip direction are usually the plane and direction where the atoms are most densely arranged, the slip plane and the slip direction are different for different metal crystal structures.

Table 1.1 lists the slip systems in two crystal structure metals, f.c.c. and b.c.c. When a metal material is loaded (during tensile or compression tests), plastic deformation occurs on one or more slip systems. In metals, plasticity occurs through dislocation motion usually along the closet atomic direction in the densest atomic planes. In f.c.c. metals, the most densely packed atomic plane family is {111}. The most densely packed direction family is <110>, so there are 12 possible slip systems.

Crystal structure	Slip plane	Slip direction	Number of slip systems
f.c.c.	{111}	⟨110⟩	12
b.c.c.	{110}	⟨111⟩	12
	{112}	⟨111⟩	12
	{123}	⟨111⟩	24

Table 1.1 – Slip systems in f.c.c. and b.c.c. metal.

In b.c.c. metals, slip always occurs on the {110} planes, where the atoms are most densely packed. However, it may also occur on other planes, namely {112} and {123}. It has been found that at low temperatures, dislocations are prone to slip on the {110} planes, and at high temperatures, the {112} slip planes are more likely to be activated[SEE 02]. The slip direction is always <111>, so the b.c.c. metals have possible 48 slip systems.

However, slip occurs only when the shear stress along the slip direction in a specific slip plane reaches a certain critical value. Schmid's law states that in a material under stress, the dislocation slip plane and slip direction must correspond to the maximum shear stress. The resolved shear stress (RSS) is the projection of the applied stress onto a slip plane. From Schmid's law, it is possible to compute the RSS from the applied stress and the Schmid factor. The Schmid factor is equal to the cosine of the angle ψ between the applied force and the vector normal to the glide plane, multiplied by the cosine of the

Cette thèse est accessible à l'adresse : https://theses.insa-lyon.fr/publication/2022ISAL0090/these.pdf
© [R. Zhang], [2022], INSA Lyon, tous droits réservés

angle λ between the applied force and the slip direction (Fig 1.7):

$$\tau_{CRSS} = F_r/A$$

Where:

$F_r = F \cdot \cos \lambda$ is the projection of the applied force onto the slip plane,

$A = A_0 \cdot \cos \Psi$ is the area of slip plane,

$\sigma_{app} = F \ / \ A_0$ is the applied stress

From the formula above, $\tau_{CRSS}=\sigma_{app} \cdot \cos \lambda \cos \Psi$, where $\cos \lambda \cos \Psi$ is the defined as Schmid factor S.

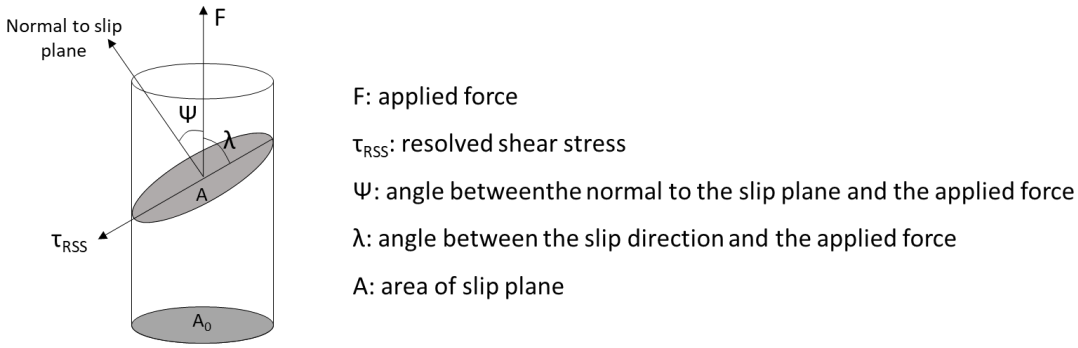

Figure 1.7 – definition of the angles involved into the computation of the Schmid factor

The applied stress σ_{app} multiplied by the Schmid factor S gives access to the resolved shear stress $\tau_{RSS} = \sigma_{RSS} \cdot$S on a specific slip plane. The critical resolved shear stress (CRSS) is the RSS value that is required to initiate plasticity. It depends neither on the applied force, nor on crystal orientation. It is equal to the product of the yield strength and the maximum Schmid factor.

Why do dislocations not glide easily in ceramic materials? Because the bonds in ceramics differ from those in metals. In fact, metal atoms are linked to each other by metallic bonds. Positive ions are immersed in a cloud of electrons and the electrostatic attraction between them makes the metal atoms bond to each other. When the metal crystal is distorted, the displacement of metal ions occurs, but the binding effects of the free electrons

Cette thèse est accessible à l'adresse : https://theses.insa-lyon.fr/publication/2022ISAL0090/these.pdf
© [R. Zhang], [2022], INSA Lyon, tous droits réservés

do not change, so the metal crystal has good ductility. However, in ceramic materials, it must be taken into account that the covalent bond is too strong to move an atom. Alternatively, the electrostatic effect of the ionic bond makes the dislocations difficult to slip.

However, the criteria does not always work in ionic crystals. For example, MgO is one of the most known ceramics and its mechanical properties have attracted much attention. Many studies consider MgO as a model for ionic ceramic material in order to study plastic deformation. MgO has a cubic structure and cations are the most densely packed in the {111} planes, which are the the primary slip planes according to the slip system definition. However, due to electrostatic repulsion between ions of the same kind, dislocations are more likely to slip on the planes {110} and {100}. Many experiments and simulations have shown that the plastic behavior of MgO is mainly governed by the <110>{110} slip systems[AMO 21]. Because of the ionic nature, the definition of ion crystal slip systems can be more complex than that of metals. Take CeO_2 as an example. Along [001], there is a continuous sequence of anion and cations layers. This means that the {100} planes contain only one type of ions, namely anions or cations (Fig1.8a). Such {100} planes can slip in a relatively stable way along the vector 1/2<110> because planes with opposite charges are on both sides. It is different on {110} planes. To translate {110} planes by the vector 1/2<110>, electrostatic forces have to be considered especially when the planes slip by the vector 1/4<110>, as shown in Fig 1.8b and Fig 1.8c. Indeed, The near-field oxygen ions repel each other, causing slipping imbalances. From this point of view, a slip system can not only judged according to elastic criteria but also based on electrostatic considerations.

Movement of dislocations in crystalline materials is characteristic of displacive deformation. It has to be noted that plastic deformation can also take place by atom diffusion, which is more common at high temperatures. Some examples of bulk ceramics show ductility at elevated temperatures. At high temperatures, they all have improved plastic deformation capabilities [COP 65][CRA 80][BEC 71].

Subsequently, it was found that even at room temperature, polycrystalline ceramics can also exhibit plasticity when their grain size is decreased. In 1987, Karch et al. tested

Cette thèse est accessible à l'adresse : https://theses.insa-lyon.fr/publication/2022ISAL0090/these.pdf
© [R. Zhang], [2022], INSA Lyon, tous droits réservés

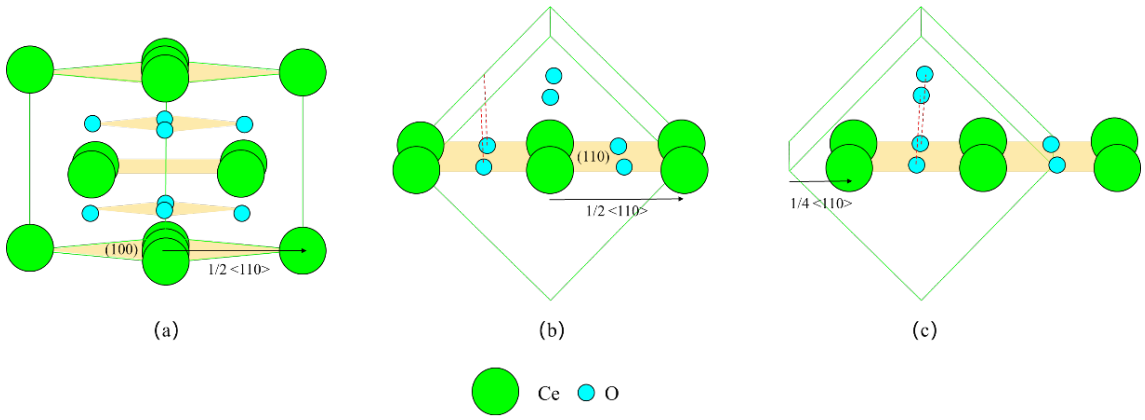

Figure 1.8 – (a) Sequence of (100) planes in CeO_2, showing the succession of anion and cations layers. (b) A (110) plane exhibiting neutral charge. (c) (110) plane glide along vector 1/4<110>, with close oxygen ions repelling each other

nanocrystalline TiO_2 with small grain sizes (1-10 nm) at low temperatures [KAR 87]. The diffusion rate increased by a factor of 10^{12} by reducing the grain size to a few nanometers. Fig 1.9(a) is the result of deformation. The sample was originally an ultrafine-grained polycrystalline TiO_2 layer sandwiched between two flat Al layers. One can see that it has a certain degree of curvature after deformation. From the image at higher magnification in Fig 1.9 (b), some pre-cracks are visible in TiO_2 after deformation. However, when compared to a monocrystalline sample in (c), under the same test conditions, a polycrystalline sample has higher ductility and does not show an obvious fracture.

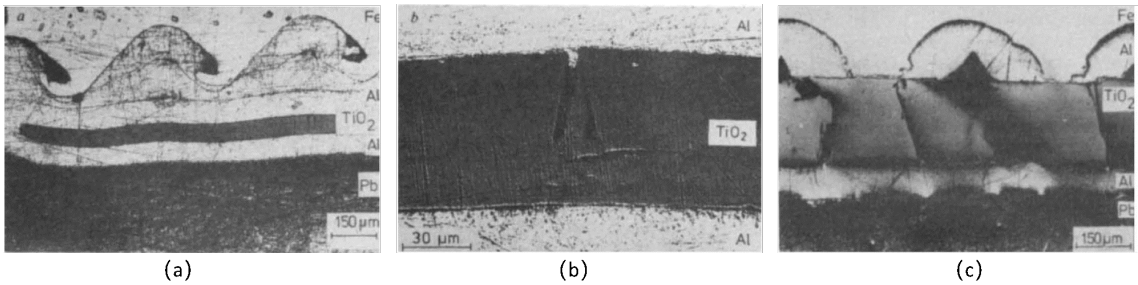

Figure 1.9 – Figure taken from [KAR 87], showing TiO_2 films after bending tests. (a) nanocrystalline TiO_2 film after plastic deformation. The specimen was initially flat. (b) magnified image from (a). After bending, the sample is pre-cracked. (c) Brittle fracture of a TiO_2 single crystal when deformed under the same conditions as in (a).

Cette thèse est accessible à l'adresse : https://theses.insa-lyon.fr/publication/2022ISAL0090/these.pdf
© [R. Zhang], [2022], INSA Lyon, tous droits réservés

Many simulation studies have explored the impact of grain size on the plastic behaviour of ceramic materials. Zhang et al. [ZHA 13] used molecular dynamics simulations and performed numerical tensile tests on nanocrystalline SiC at room temperature and high strain rate. The result is shown in Fig 1.10. They tested several samples with different size grains, namely 2 nm, 4 nm, and 6 nm. Tersoff-1, Tersoff-2, Tersoff-3, and Vashishta are different potentials. All the results show that the sample with a smaller grain size exhibits better plastic deformation.

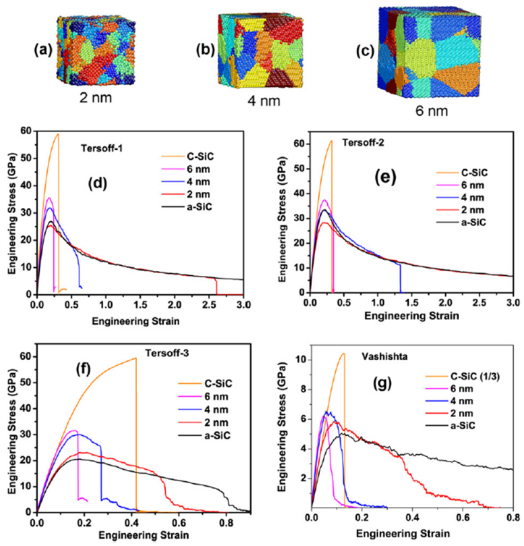

Figure 1.10 – Figure taken from [ZHA 13] showing the mechanical response of SiC with different grain sizes subjected to tensile loading. (a–c) Nanocrystalline SiC (NC-SiC) structures with average grain size d = 2, 4 and 6 nm. Grains are shown in different colors. (d–g), Stress-strain curves for NC-SiC with d = 2, 4 and 6 nm, as well as for a-SiC (amorphous SiC) and C-SiC (monocrystal with orientation <100>). Each graph corresponds to a potential (Tersoff-1, Tersoff-2, Tersoff-3 and Vashishta).

In addition to the mechanism of plasticity due to small grain size, other factors are gradually being evidenced. Researchers proved that brittle-ductile transformation in ceramics can be caused by phase changes. For instance, a SiC nanowire was bent by Han et al. in a TEM, and it showed an excellent plastic deformation ability due to the process of crystalline-amorphous phase change [HAN 07]. Similar results in SiC were also obtained in another experiment [ZHA 07].

Cette thèse est accessible à l'adresse : https://theses.insa-lyon.fr/publication/2022ISAL0090/these.pdf
© [R. Zhang], [2022], INSA Lyon, tous droits réservés

The effect of defects on the plastic deformation behavior of ceramic materials has also been studied using TEM. Hsiao et al. [HSI 19] compressed ZrN nanopillars in TEM. They observed that dislocations were generated from the top of the pillar at the beginning of the loading. The dislocations gradually moved forward the bottom of the pillar during the continuous compression process. At the end, microcracks nucleated due to the interactions between dislocations and grain boundariess.

The deformation mechanisms mentioned above are related to grain boundaries. With these works, we can see that no matter which deformation mechanism occurs, it is mainly affected by the grains. Actually, there are many factors that can influence the mechanical behavior of ceramics, as shown in Fig 1.11 [YAN 19].

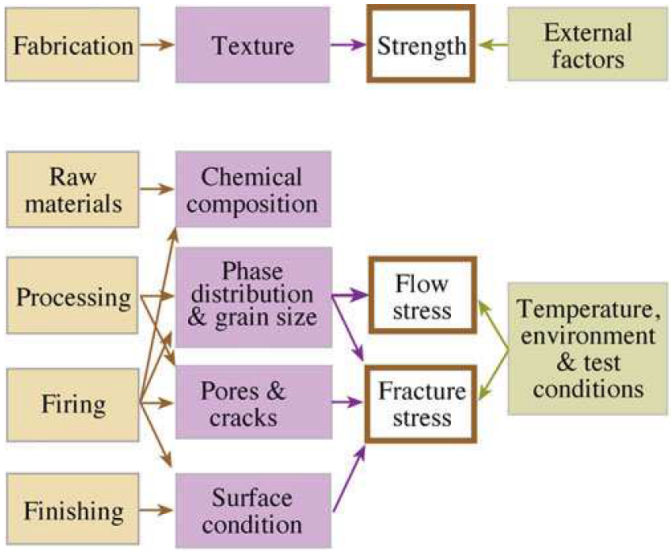

Figure 1.11 – Factors affecting the mechanical properties of ceramics[YAN 19].

It is critical to explore the fundamental nature of plasticity in ceramics using a sample with a monocrystalline structure. In order to explore the influence of dislocations on the mechanical behavior of single crystal ceramics, tremendous researches have been conducted for a long time. In the 1960s, Meldelson et al. used etching technology and found that dislocations could easily move in LiF single crystals [MEN 62]. In another study performed by Brunner et al., the type of dislocation movement was found to directly affect the mechanical behavior of $SrTiO_3$ [BRU 01]. Jin Li et al. [LI 19] used flash-sintering to obtain TiO_2 samples and compressed TiO_2 nano-pillars in a scanning electron microscope (SEM).

Cette thèse est accessible à l'adresse : https://theses.insa-lyon.fr/publication/2022ISAL0090/these.pdf
© [R. Zhang], [2022], INSA Lyon, tous droits réservés

The pillars exhibited good plasticity at room temperature. The mechanical curve and SEM images are shown in Fig 1.12. In addition, the authors observed that plasticity was dominated by the formation of nanoscale stacking faults. The author thought that flash-sintering could effectively introduce many defects, as pre-existing seeds are very beneficial to the later emergence of plastic deformation. However, the formation of stacking faults and twins is not common in ceramic materials, and plasticity is very rare.

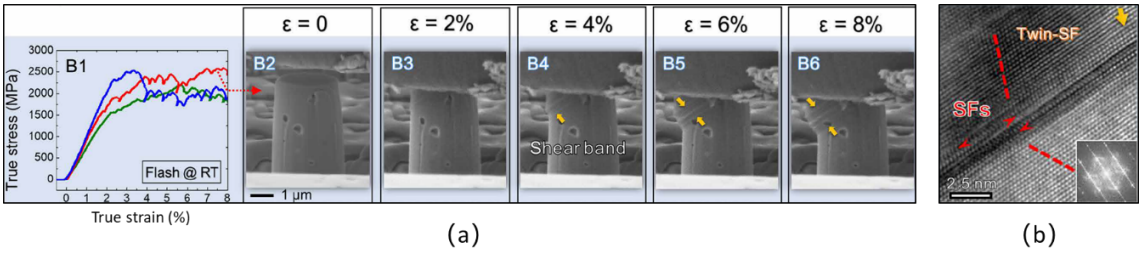

Figure 1.12 – compression of a TiO_2 nano-pillar at room temperature. (a) True strain - true stress curve and SEM images at different strains. (b) TEM image showing nanoscale stacking faults and nanotwins. Image taken from [LI 19].

More recent technologies have also been used to explore the mechanical behavior of materials. Inas et al. [ISS 16] investigated the mechanical behavior of monocrystalline MgO nanocubes of size around 100 nm using *in situ* TEM. The experiments clearly revealed the process of deformation during the whole compression test. It was found that the deformation was very uniform and presented high strength, see Fig1.13. After compression, no failure was found. By the contrast of the TEM images, it can be observed that a lot of dislocations were nucleated. Then the Burgers vector of dislocations are characterized thanks to the comparison with Molecular Dynamics simulations. This result provides a direct insight for the deformation process of monocrystalline MgO nanocubes and gives us a new understanding and evidence for the mechanism of plastic deformation behavior of ceramics: Nano-scaled ceramic material could present good plasticity dominated by dislocations, similarly to metals.

Cette thèse est accessible à l'adresse : https://theses.insa-lyon.fr/publication/2022ISAL0090/these.pdf
© [R. Zhang], [2022], INSA Lyon, tous droits réservés

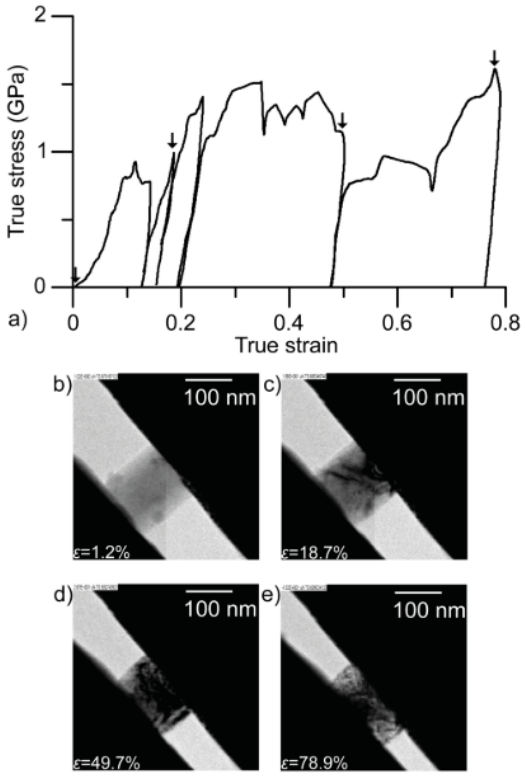

Figure 1.13 – *In situ* TEM compression of monocrystalline MgO nanocubes. (a) Stress-strain curve for a 140 nm MgO nanocube compressed *in situ*. Five loading-unloading cycles are shown. Black arrows refer to the state at which snapshots were taken. (b)-(e) Images at $\epsilon = 1.2\%$, $\epsilon = 18.7\%$, ϵ=49.7%,$\epsilon = 78.9\%$. Figure taken from [ISS 15].

1.1.3 Plasticity in nano-objects

On the contrary to ceramics, the mechanical behavior in submicron-scale metals has been widely studied. As early as in the 1950s, Brenner et al. [BRE 58] conducted tensile tests on iron whiskers of different diameters at the micron scale. It was found that their strength increased rapidly with decreasing diameters, exhibiting a significant size effect. In particular, when the whisker diameter was reduced to about 1.6 μm, the strength was as high as 13.5 GPa, which largely exceeds the tensile strength of bulk iron (200 MPa). More and more experimental studies have shown that submicron metal materials often exhibit plastic deformation behaviors different from those of their bulk counterparts. To better investigate the mechanical properties of materials at the submicron scale, Uchic et al. [UCH 04] pioneered a new approach to microcompression testing. They first processed

Cette thèse est accessible à l'adresse : https://theses.insa-lyon.fr/publication/2022ISAL0090/these.pdf
© [R. Zhang], [2022], INSA Lyon, tous droits réservés

micron-sized pillars made of face-centered cubic (FCC) Ni, Ni_3Al single crystals using focused ion beam (FIB). The mechanical properties of the samples were tested under uniaxial compression with a planar indenter. This method eliminates many drawbacks associated with other techniques and ensures that no strain gradients are affected. As shown in Fig1.14, the experimental results show a significant increase in strength as the material size decreases. This phenomenon has attracted wide attention, and many research groups reported similar results with similar testing methods [FRI 07][GRE 05][VOL 06b][DIM 05]. The researchers also noted that the stress-strain curves of submicron specimens no longer show smooth continuity, but exhibit discrete step-like steep strain increase [CSI 07].

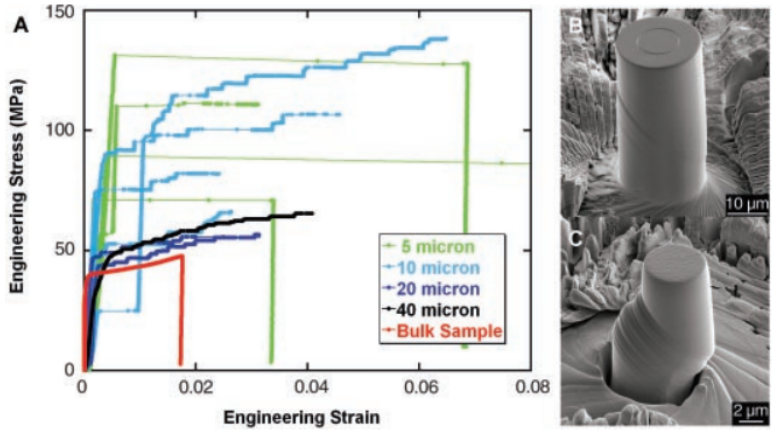

Figure 1.14 – Results of compression experiments on Ni single-crystal microcolumns of different diameters. Figure taken from [UCH 04]

In the following, three typical anti-conventional plastic behaviors observed at the submicron scale are detailed: size effect on the strength, strain bursts and size effect on the cyclic response.

Size effect on strength

The flow stress(σ) varies with the sample diameter according to a power law, that is to say $\sigma \propto D^{-a}$, where a is the size effect strengthening index [KRA 10]. Depending on the mechanism, the size effect can be classified into three categories.

Within the first category, the size effect is caused by microstructural inhomogeneities

Cette thèse est accessible à l'adresse : https://theses.insa-lyon.fr/publication/2022ISAL0090/these.pdf
© [R. Zhang], [2022], INSA Lyon, tous droits réservés

or boundary conditions in single crystals. For example, in nanoindentation experiments, it is necessary to store a large number of dislocations inside the specimen to coordinate the plastic deformation gradient, thereby causing the hardening effect [BUS 04]. This size effect can be described by the strain gradient plasticity theory [NIX 98].
In the second category, the size effect can be attributed to the internal microstructure such as grain boundaries or second-phase particles, which can hinder dislocation slip. The finer the grains and the more diffusely distributed the particles are, the more pronounced the strengthening will be. Usually, it can be predicted with the help of the Hall-Petch relationship [HAL 51][PET 53] and Orowan mechanism [KEL 71].
The third category contains defect-free single crystals, with dimensions close to the dislocation configuration. Initially, the study focused on thin film specimens, and a dislocation channel model was proposed to predict the opening stress of dislocations in films with passivated layers and free surface films. This size effect in thin films is also attributed to the hindering dislocation gliding from the interfaces or passivated layer [NIX 89]. From these results, the size effect seems to be mainly caused by two phenomena: (i) strain gradient, (ii) hindering effect to dislocation gliding (Hall-Petch effect and Orowan mechanism).

In addition to thin film samples, size effects have also been observed in samples prepared from bulk single crystals by FIB [UCH 04]. Uniaxial compression of submicron single-crystal pillar has shown size effect that are completely dominated by geometric constraints. Many research studies have been carried out to investigate this new kind of size effect. A review will be given in chapter 1.3. Fig1.15 summarizes the 3 different mechanisms giving rise to size effect.

However, there is a critical factor that cannot be ignored during FIB experiments: FIB uses an ion beam to mill the samples. Some ions from the FIB ion beam are implanted into the sample surface during milling and may produce dislocation loops in the sample surface layer. The introduction of these dislocation loops may affect the deformation behavior of the sample [LEE 16]. To exclude the influence of these factors, this PhD work is focused on the uniaxial compression on the single crystal nanocubes produced without any FIB milling.

Strain bursts Many experiments show that plasticity of submicron crystals is not con-

Cette thèse est accessible à l'adresse : https://theses.insa-lyon.fr/publication/2022ISAL0090/these.pdf
© [R. Zhang], [2022], INSA Lyon, tous droits réservés

Reason of origin	Description	Mechanism Model	Examples
Deformation restraint	By the microstructural inhomogeneities or border conditions that cause massive dislocation plugging	Strain gradient plasticity theory	Nanoindentation 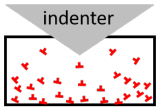
Microstructural constraints	By the internal hindering effect of microstructure on dislocation slip.	For grain boundary: Hall-Petch effect For precipitates: The dislocation bow-out model. (Orowan mechanism)	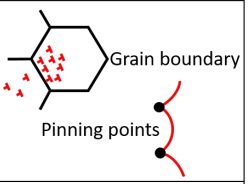
Geometrical constraints	When the geometry of the specimen is close to the dislocation configuration	For thin film: Orowan mechanism For micropillar: depletion of dislocation Single-arm source mechanism	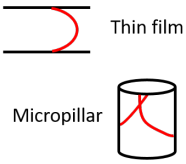

Figure 1.15 – summary of the different mechanisms causing size effects

tinuous. As shown in Fig1.16, whatever the type of test (displacement- or force-controlled experiments), all stress-strain curves exhibit strain bursts. [SOE 07]

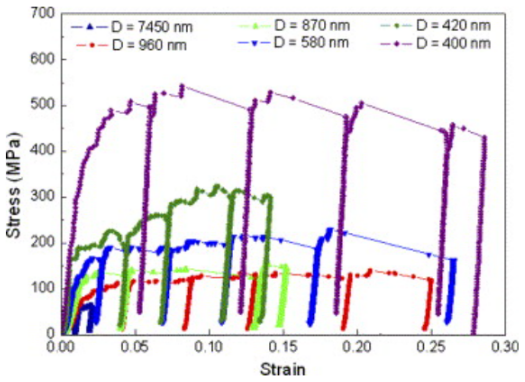

(a) Stress-strain curve of Au single crystal pillars obtained from displacement-controlled tests [GRE 05]

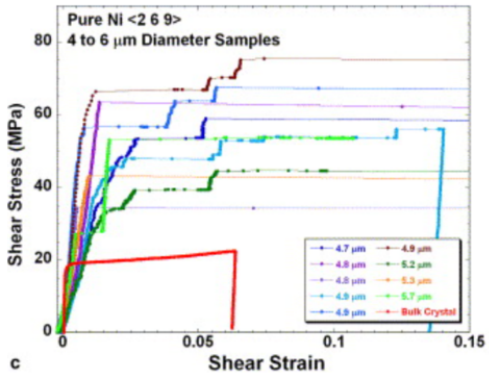

(b) Stress-strain curve of Ni single crystal pillars obtained from force-controlled tests [DIM 05].

Figure 1.16 – Examples of stress-strain curves obtained from two loading modes

.

Strain bursts can be explained using two different mechanisms. In the first mecha-

Cette thèse est accessible à l'adresse : https://theses.insa-lyon.fr/publication/2022ISAL0090/these.pdf
© [R. Zhang], [2022], INSA Lyon, tous droits réservés

nism, the crystal already includes many dislocations. Csikor et al. [CSI 07] suggested that the appearance of a strain burst depends on the generation and rapid aggregation of avalanches of dislocations. Tang et al. [TAN 08] suggested that the initial small strain bursts are controlled by the annihilation of individual dislocations on the free surface, while the larger strain bursts are controlled by the nucleation of dislocation sources. Rao et al. [RAO 07] also found a correlation between strain bursts and dislocation sources. Maaß et al. [MAA 07] proposed that the strain bursts are related to strain gradients and complex dislocation interactions in small localized areas.

In the second mechanism, the crystal contains no defect before compression. Researchers have found that not only strain bursts exist in such crystals, but also instantaneous changes in specimen morphology may be induced by strain bursts. Mook et al. [MOO 09] and Wang et al. [WAN 12] observed serious collapse behavior in Au submicron single crystals that were initially defect-free. To explain this phenomenon, they calculated the energy release rate corresponding to the local slip steps generated during a strain burst. They suggested that the energy release rate of the strain burst is very similar to the macroscopic fracture process of semi-brittle materials. Wang et al. also suggested that this phenomenon occurs because the sample undergoes a highly correlated nucleation of dislocations under high stresses, which converge to the theoretical strength. However, due to the limitation of the specimen size, the dislocations cannot form a dislocation lock and slip out instantaneously of the specimen surface . Hu et al. [HU 14] discussed the effect of strain gradients on dislocations through molecular dynamics simulations and finite element analysis. They discussed the effect of strain gradient on the dislocation distribution, and used an energy analysis method based on the potential energy standing value. A principle-based energy analysis method was used to predict the critical load for large bursts or collapses.

Size effect on the cyclic response

In actual use, devices are also often subjected to cyclic loading. Conventional bulk materials may be subjected to fatigue damage under cyclic loading. Wang et al. [WAN 08] showed that the fatigue life under high circumferential cyclic loading also has a size effect. When the film thickness is small, the fatigue life is significantly increased. Muhlstein et al. [MUH 01] showed that although bulk Si single crystal is brittle, it can withstand high

Cette thèse est accessible à l'adresse : https://theses.insa-lyon.fr/publication/2022ISAL0090/these.pdf
© [R. Zhang], [2022], INSA Lyon, tous droits réservés

circumferential cyclic loads when the Si film thickness is reduced to about 20 μm. Zhang et al. [ZHA 06] found that polycrystalline Cu films of different thicknesses exhibit different characteristic dislocation patterns when cyclically loaded. Dislocation walls appeared when the film thickness is 3 μm, dislocation structures appeared as diffuse cells when the thickness is 1 μm, and only isolated dislocation lines could be observed when the thickness was reduced to 0.4 μm. Kiener et al. [KIE 10] analyzed the envelope response of Cu single-crystal microbeams subjected to cyclic bending loads. Namazu et al. [NAM 08] studied the cyclic tensile response of single-crystal Si, but the smallest feature size of their tensile specimens was 76 μm.

When the specimen size is further reduced, the effective free range of dislocation sliding in the specimen is shorter, and the mirror attraction of the free surface to the dislocation is more significant, leading to an easier surface annihilation. Kiener et al. [KIE 11] performed multiple tensile tests on single crystal specimens with minimum feature sizes of 100-200 nm and showed that the initially high dislocation density decreases with multiple loading. This is quite different from the dislocation accumulation process in macroscopic bulk materials. More interestingly, Wang et al. [WAN 15b] recently performed cyclic tensile experiments at lower amplitudes on single-crystal Al columns with a characteristic size of 387 nm and observed that internal dislocations gradually annihilated with cyclic loading, letting the crystal eventually completely depleted. They also performed uniaxial tensile tests after cycling and showed that the dislocation-free specimens exhibited very high yield strengths and significant necking characteristics. This finding is of great importance for the application of submicron devices, as it provides a new method to regulate the internal defect density with the help of mechanical loading, which has a significant effect on their mechanical, thermal, and electrical properties. It is worth mentioning that the overall deformation of the specimen was small due to the low amplitude of cyclic stresses in the experiments of Wang et al. This indicates that the method can be used to obtain dislocation-free specimens with little change in the machined morphology of the specimens.

Cette thèse est accessible à l'adresse : https://theses.insa-lyon.fr/publication/2022ISAL0090/these.pdf
© [R. Zhang], [2022], INSA Lyon, tous droits réservés

1.2 Size effect on the strength of submicron-sized materials

In section 1.1.3, three categories of size effect were introduced, depending on the influence of strain gradient or hindering effect to dislocation gliding. With the development of FIB machining, it is possible to decrease the influence from the strain gradient and prepare single-crystal specimens, with no interfaces and secondary phases that could hinder dislocation movement. However, due to their small dimensions, the samples may also present an effect of the size onto their strength. Therefore in this section, we mainly introduce the influence of the sample size due to geometric constrains. At this point, it is noteworthy that FIB processing also can introduce strain or defects into the sample. Nanoparticles are the optimal solution for these issues, despite the fact that they may include defects.

1.2.1 Size effect in metals

Researchers have proposed different models to explain the effect of size onto strength. The earliest model is dislocation starvation [GRE 05]. It assumes that dislocations can easily escape from the surface of small samples and the associated velocity is faster than that of dislocation multiplication. It results in a decreasing of the density of dislocations, leading even to a depleted state. In order to reach further plastic deformation, an extra force is needed to nucleate new dislocations. Afterwards, Shan et al. [SHA 08] confirmed the dislocation nucleation-starvation model. During uniaxial compression experiments on 160 nm diameter nickel pillars in TEM, they observed the escape of dislocations through the surface, which resulted in a gradual dislocation depletion. Subsequently, three-dimensional dislocation simulations by Liu et al. [LIU 09] also confirmed dislocation depletion during compression and its induced hardening effect. Benzerga [BEN 09] further pointed out that dislocation depletion is more likely to occur in specimens with lower initial dislocation densities. Nix et al. [NIX 11] developed a plasticity model for submicron single-crystal pillars controlled by dislocation surface nucleation with the help of image-only descriptions, and predicted this kind of size effect.

Another model used to account for the size effect is the single-arm source model. Simulation works and experiments in TEM found that dislocation sources present new characteristics in submicron samples. In bulk samples, Frank-Read dislocation is a common

Cette thèse est accessible à l'adresse : https://theses.insa-lyon.fr/publication/2022ISAL0090/these.pdf
© [R. Zhang], [2022], INSA Lyon, tous droits réservés

dislocation source pinned on two defect points. The pinned dislocation expands under force and entangles with itself, creating a new dislocation loop. However, in small-scale samples, there are not two pinning points but only one. When the dislocation expands, the dislocation that is not entangled yet will be truncated by the surface first. The dislocation becomes a single-arm dislocation source with only one pinning point. Truncation hardening occurs in the distribution of arm lengths. Rao et al. [RAO 07] discussed the effect of the anisotropy of dislocation line tension on the single-arm source opening stress based on 3D dislocation dynamics simulations. Parthasarathy et al. [PAR 07] proposed a statistical-based single-arm source model, which can be found also for the initial yield strength of face-centered cubic crystals and its size effect according to the weakest single-arm source strength. Lee et al. [LEE 12] found that this single-arm source model is also applicable to body-centered cubic crystals and used it to discuss the exponential form of the size effect on the material constant.

In practice, the size effect phenomenon has been found in f.c.c and b.c.c.materials [BRI 08] [SCH 09a], but the dependence of strength on size in b.c.c materials is lower than the one in the f.c.c. ones. Indeed, uniaxial compression experiments of b.c.c. Mo metal and f.c.c. Au metal pillars with micrometer sizes were conducted in the literature [BRI 08]. As shown in Fig 1.17, the size strengthening index a is 0.45 in Mo. This value is smaller than that in Au, which is 0.97. A series of experimental results indicates that for f.c.c. metals, a lies in the range 0.6-0.97 [UCH 06] [VOL 06a] [KIE 06] but for b.c.c. metals, a ranges from 0.22 to 0.48 [BRI 08] [SCH 09a] [SCH 09b]. The difference is speculated to be due to differences in the mechanisms involved.

As shown in Fig 1.18a, for f.c.c. metals, plasticity is found to be dominated by the slip of dislocations to the free surface. Dislocations glide on the (111) plane. During movement, the dislocations may decompose into pairs of partials with the appearance of stacking faults. The whole dislocation movement is limited in the (111) slip plane due to the coplanar dislocation cores. It is considered that the velocities of edge and screw dislocations are equal, so the dislocation continues to slip until it reaches the pillar surface and escapes. The pillar becomes thus depleted, which confirms the previously proposed mechanism of dislocation nucleation-starvation.

Cette thèse est accessible à l'adresse : https://theses.insa-lyon.fr/publication/2022ISAL0090/these.pdf
© [R. Zhang], [2022], INSA Lyon, tous droits réservés

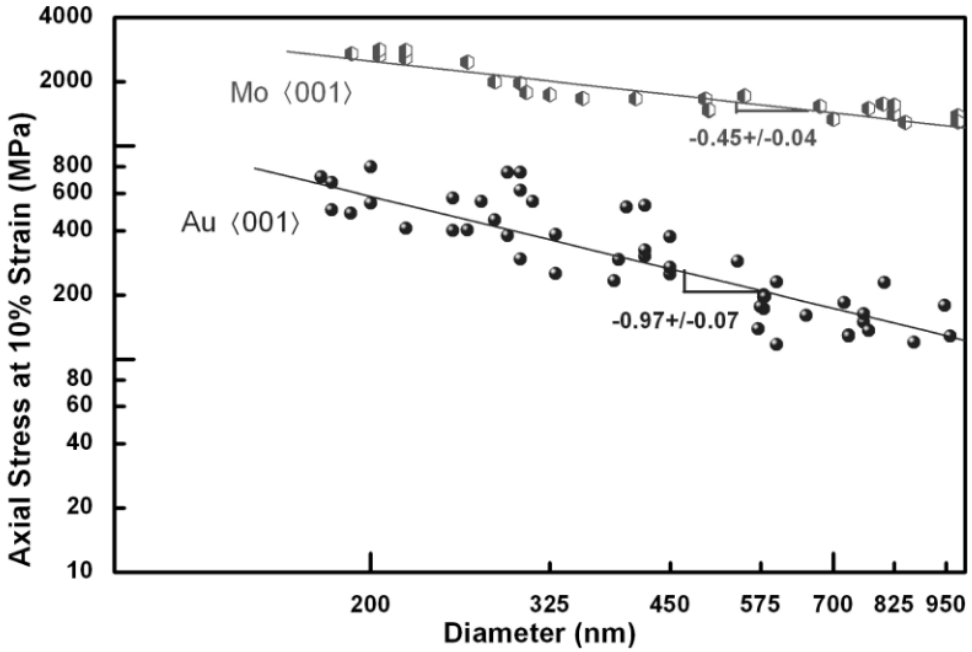

Figure 1.17 – Size effect phenomenon in f.c.c. and BCC metals.

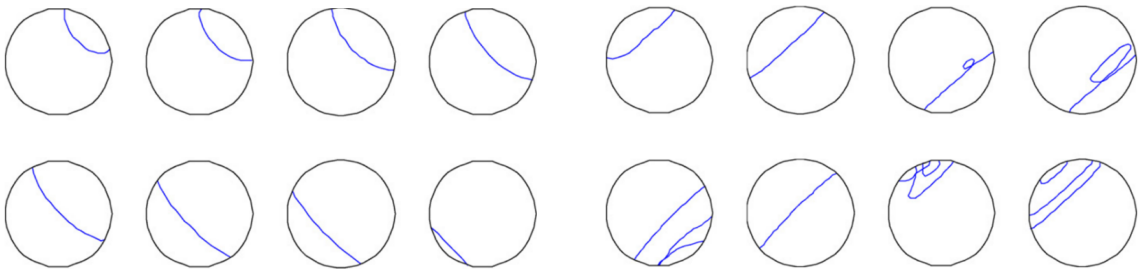

(a) Dislocation gliding along the (1 1 1) plane in an f.c.c. Crystal (observed along the axial direction of the cylinder). f.c.c. dislocations quickly escape to the surface, leaving a dislocation-starved cylinder.

(b) Dislocation gliding along the (0 -11) plane in a b.c.c. pillar. The b.c.c. screw dislocation emits additional dislocations, promoting strain hardening.

Figure 1.18 – Comparison of the size effect mechanism in b.c.c. and f.c.c. metallic single crystals [GRE 08].

.

In b.c.c. metals, as shown in Fig1.18b a long and slow screw dislocation is left in the process of slip because the speed of the edge part of dislocation is larger than that

Cette thèse est accessible à l'adresse : https://theses.insa-lyon.fr/publication/2022ISAL0090/these.pdf
© [R. Zhang], [2022], INSA Lyon, tous droits réservés

of the screw one. In the literature, experimental [LUF 70a] [LUF 70b] and simulation works [LAW 64] confirmed that plastic deformation in b.c.c. metals at room temperature is mainly controlled by screw dislocations. A screw dislocation with long and slow slip velocity moves to another plane through cross slip. Thus a cross twist is generated and gradually evolves into a dislocation loop. The edge part of the dislocation loop quickly escapes from the free surface. It leaves two new screw dislocations segments on the slip plane, which means the dislocation self-proliferates. The same result was confirmed in the work published by Weinberger and Cai [WEI 08].

In short, in small-size metal samples, the size effect mechanisms are found to be different in f.c.c. and b.c.c. single crystals. For f.c.c. lattices, the dislocation nucleation-starvation model is used to explain the size effect. However, in b.c.c. metals, a traditional dislocation forest hardening mechanism is more often used to explain the size effect phenomenon.

1.2.2 Size effect in ceramics

First *in situ* compression experiments on alumina nanoparticles revealed a peculiar behaviour for ceramics known as brittle material: plasticity was observed at room temperature. A 100 nm alumina single crystal particle, which had not undergone special processing before testing, exhibited impressive ductility during the compression [CAL 14] [CAL 12]. By combining experimental data and Finite element simulations, the result showed a complete elastic-plastic deformation. Issa et al. [ISS 18] used the same test conditions to compress *in situ* MgO monocrystalline cubes. It was discovered that such behavior was related to the strong influence of dislocation starvation in smaller nanocubes (smaller than about 200 nm). The experiments and MD simulation results also revealed the relationship between strain bursts and avalanches of perfect dislocations. In larger nanocubes, it appears that dislocation already exist in the sample before compression, so plasticity is mainly governed by dislocation multiplication, as in bulk materials.

And size effect is further discussed. The work published by Issa et al. [ISS 21] dealt with the size effect in MgO single crystals. For the bigger cubes, the size effect matches the trend predicted by the formula (σ=σ_0 +Ad^{-1}). This is attributed to geometrical constraints affecting pre-existing dislocations. For smaller samples, their yield points are

Cette thèse est accessible à l'adresse : https://theses.insa-lyon.fr/publication/2022ISAL0090/these.pdf
© [R. Zhang], [2022], INSA Lyon, tous droits réservés

randomly dispersed above the curve. The yield points are however limited by an upper bound corresponding to the same formula $\sigma=\sigma_0 + Ad^{-1}$, modified by the rarefaction of dislocation sources.

1.3 General conclusion of Chapter1

Improving the material strength and ductility is the quest of most materials scientists. Ceramic materials are of interest because of their excellent strength but their main problem is their brittleness at room temperature. Indeed, due to the ionic or covalent bonds, which make dislocation motion difficult, ceramic materials often fail to reach the plastic deformation stage.
The improvement of the deformability of ceramic materials would be interesting for numerous applications, among which their fabrication. The first stepp is to better understand the plastic behaviour of ceramic nanoparticles, as they are used as building blocks for bulk ceramics fabrication.

Because the crystal structure of ceramics is more complex than that of metals, some theories applied in metals may not be directly applicable to ceramic materials. For nanoscale ceramic samples with monocrystalline structures, many research are confined to theoretical studies and experiments evidence remains scarce.

In such context and in view of the literature presented in this chapter, this work aims at studying the room-temperature plastic behavior of ceramic nano-objects. We selected cerium dioxide (CeO_2) as research subject because of its wide application range and because there are few experimental results in the literature. In the next section, we present a bibliographic study of the structure and mechanical properties of CeO_2 monocrystals and other fluorite oxides.
We decided to use *in situ* mechanical tests in transmission electron microscopy, as this technique has already proven its capabilities in this field during the PhD works of E. Calvié and I. Issa in the MATEIS laboratory. Moreover, this PhD is part of an ANR project and benefits from simulation works performed at Institut Lumière Matière by G. Laurens and T. Albaret.

Cette thèse est accessible à l'adresse : https://theses.insa-lyon.fr/publication/2022ISAL0090/these.pdf
© [R. Zhang], [2022], INSA Lyon, tous droits réservés

Cette thèse est accessible à l'adresse : https://theses.insa-lyon.fr/publication/2022ISAL0090/these.pdf
© [R. Zhang], [2022], INSA Lyon, tous droits réservés

Chapter 2

Introduction to cerium oxides

This chapter aims at presenting the main characteristics of cerium oxide - ceria - CeO_2 in the fluorite structure. As CeO_2 may be reduced under the electron beam, the different structures of CeO_x will also be introduced, with a focus on bixbyite. In both cases - fluorite and bixbyite - an overview of the mechanical properties will be given with a particular attention to the possible slip systems.

2.1 Introduction to CeO_2

2.1.1 Structure of CeO_2

Usually, CeO_2 keeps the fluorite structure from room temperature to its melting point (2750 K) [MOG 00]. The fluorite structure corresponds to the space group Fm-3m. As shown in Fig 2.1a, cations are in a face-centered cubic (f.c.c.) unit cell and the O^{2-} anions in octahedral positions inside a f.c.c. unit cell. There are eight oxygen anions coordinated to the nearest cation (Fig 2.1b), while one anion is in the middle of a tetrahedron formed by four oxygen cations, see Fig 2.1c.

It can be mentioned here that the unit cell parameter of CeO_2 in the fluorite structure depends on the temperature. Yashima et al. [YAS 03] used a neutron powder diffraction technique to explore the relationship between the structural parameter of cerium oxides and temperature (from room temperature to 1770 K). They found that the unit cell parameter of ceria increases evenly with the temperature. The experimental results

Cette thèse est accessible à l'adresse : https://theses.insa-lyon.fr/publication/2022ISAL0090/these.pdf
© [R. Zhang], [2022], INSA Lyon, tous droits réservés

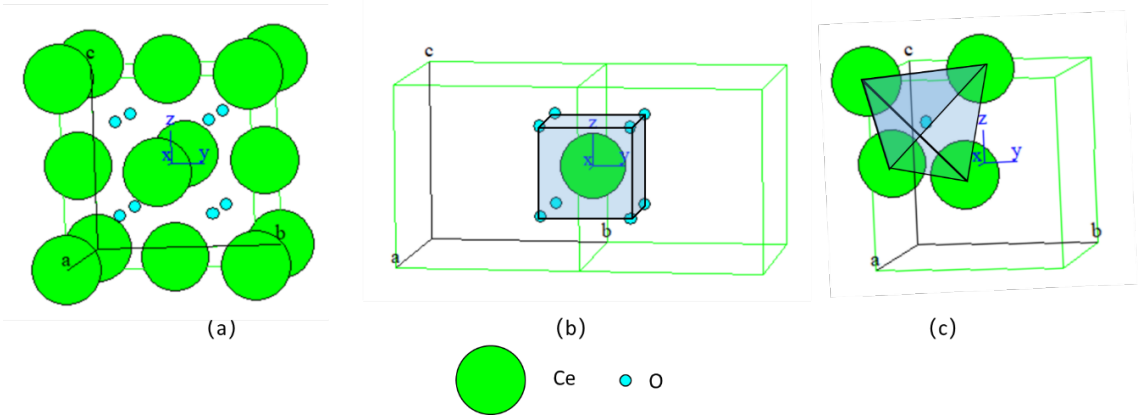

Figure 2.1 – (a) Fluorite unit cell in the case of CeO_2. (b) Details of the oxygen cube, which includes one cerium atom. (c) Ce tetrahedral structure, which includes one oxygen ion in the CeO_2 unit cell.

are consistent with those calculated using the thermal expansion formula. The unit cell parameter of CeO_2 is generally considered as 5.411 Å, value at room temperature.

2.1.2 Possible structures of CeO_x

Under reducing conditions, due to the similar energy states of the 4f and 5d bands in Ce^{3+} and Ce^{4+} [SAN 16], CeO_2 can easily change its valence state and transform into Ce_2O_3. There exists a large number of intermediate phases CeO_x ($1.5 \leq x \leq 2$). Since there is no clear consensus on the structure of these intermediate phases, many studies are still devoted to figuring them out. Table 2.1 shows the characteristics found in the literature of several phases at ambient temperature [MOM 08] [KÜM 99] [DAS 07] [QI 13].

2.1.3 Electron beam effect on CeO_2

Because cerium oxide is known to be sensitive to the electron beam when analysed in TEM, we have to consider the electron beam effect. The main consequence of electron irradiation on oxides may be atom displacement due to collisions between the incident electrons and the atoms (knock-on damage) [JIA 16].

Syo Matsumura et al. [MAT] found a relationship between the electron energy and the displacement cross-section induced by the electron beam. Fig2.2 shows calculated dis-

Cette thèse est accessible à l'adresse : https://theses.insa-lyon.fr/publication/2022ISAL0090/these.pdf
© [R. Zhang], [2022], INSA Lyon, tous droits réservés

Phase	O/Ce ratio	Lattice type	Space group	Unit cell parameters	Reference
CeO2	2	cubic	Fm-3m	a=5.411Å	[MOM 08]
Ce11O20	1.81	triclinic	P-1	a=5.411Å b=10.26Å c=6.732Å α=90.04°β=99.80°γ=96.22°	[KÜM 99]
Ce7O12	1.71	rhombohedral	R-3	a=6.785Å α=99.42°	[KÜM 99]
CeO1.68	1.68	cubic	Ia-3	a=11.111Å α=99.42°	[KÜM 99]
Ce2O3	1.5	cubic	Ia-3	a=10.89-11.42Å	[DAS 07]
Ce2O3	1.5	hexagonal	P-3m1	a=3.89Å c=6.06Å	[QI 13]

Table 2.1 – Some of the possible phases in Ce-O system

placements cross-sections for the Ce-and O-sublattices in CeO_2 based on Bethe's formula. We can see that oxygen atoms start be pushed out of their site in the oxygen sublattice when the electron energy is around 200 keV. The displacement of cerium atoms occurs when the electron energy is above around 1500 keV. Among the current various transmission electron microscopes (except in High Voltage transmission electron microscope), the energy of electron will therefore only lead to the displacement of O ions in CeO_2 structure.

The shape of the Ce $M_{4,5}$-edges obtained with electron energy-loss spectroscopy (EELS) are different between Ce^{3+} and Ce^{4+}. They can be used to determine the oxidation states in cerium oxides. Garvie and Bruseck used EELS to follow the oxidation changes in cerium dioxide, with an acceleration voltage of 100 kV [GAR 99]. From Fig2.3, besides CeO_2 and Ce_2O_3, they used Monazite-$CePO_4$, loparite-(Ce, Na, Ca)$_2$(Ti, Nb)$_2O_6$, and cerianite-CeO_2 as reference materials. It is clear that after electron beam irradiation with a short time (5 s), the peaks in damaged CeO_2 are shifted from those of CeO_2 and are closer to those of Ce_2O_3, which means the Ce^{3+} content increases after electron beam damage in CeO_2.

The following question is noteworthy: how will the structure change when CeO_2 is reduced into Ce_2O_3 under the electron beam? Usually, rare-earth sesquioxides (R_2O_3

Cette thèse est accessible à l'adresse : https://theses.insa-lyon.fr/publication/2022ISAL0090/these.pdf
© [R. Zhang], [2022], INSA Lyon, tous droits réservés

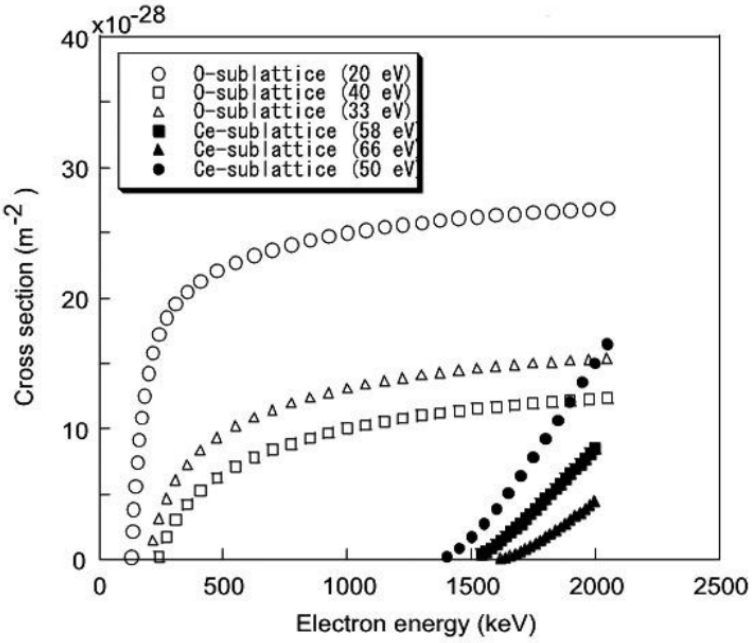

Fig. 1. Calculated displacements cross section for Ce- and O-sublattices in CeO_2 based on Bethe's formula

Figure 2.2 – Calculated displacements cross-sections for Ce-and O-sublattices in CeO_2 based on Bethe's formula [JIA 16]

R=Lanthanide) have three types of crystal structures: the A-type is hexagonal (space group is P-32/m), the B-type is monoclinic (space group is C2/m), and the C-type is body-centered cubic (space group is Ia-3) [ZIN 07]. Lijun Wu et al. [WU 04] also used EELS to confirm the structure changes in High Resolution Transmission Electron Microscopy (HRTEM) at 300 kV. With a short period (2 s) of electron beam irradiation, they found that the fluorite structure in a CeO_2 particle changed to a C-type structure and its lattice parameter was twice that of CeO_2.

2.2 Mechanical parameters of CeO_2

Table 2.2 lists the mechanical parameters of different forms and sizes of CeO_2 including hardness, Young's modulus, bulk modulus and the stress for transition from elastic to plastic. It is obvious that the Young's modulus gradually decreases with the size, from

Cette thèse est accessible à l'adresse : https://theses.insa-lyon.fr/publication/2022ISAL0090/these.pdf
© [R. Zhang], [2022], INSA Lyon, tous droits réservés

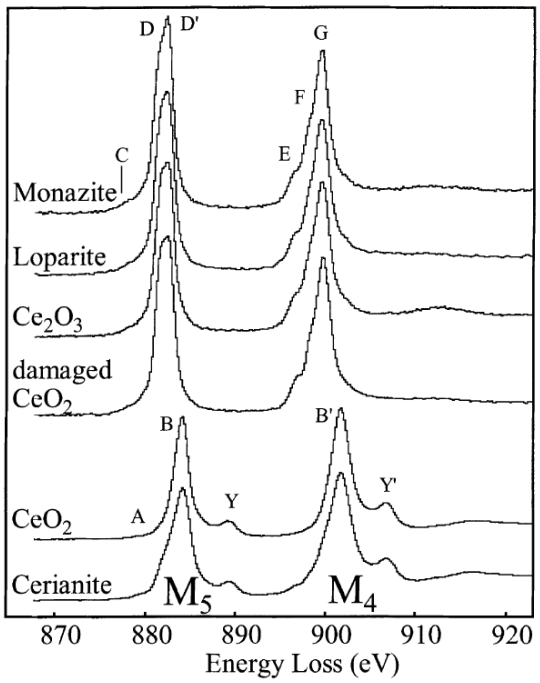

Figure 2.3 – EELS spectra of cerium oxides with different oxygen contents [GAR 99]

bulk sample to CeO_2 nanoparticles. However, no definitive study has been conducted to explore the mechanism of how the size affects the mechanical behavior of CeO_2 nano-objects.

Xiao et al. [HAO 18] found the content of Ce^{3+} increased when the CeO_2 cube size decreased. In other words, the change in size affects the phase structure of CeO_2. As explained above, it cannot be ignored that CeO_2 can be reduced under certain conditions. CeO_2 will be reduced limitedly to Ce_2O_3, which has a different structure from CeO_2. Therefore it raises a question: will the mechanical behavior of cerium dioxide be affected when it is reduced? Some simulation works studied this impact. Yuan et al. [QI 13] calculated the elastic modulus of Ce_2O_3 and found a value ranging from 131.9 to 178.1 GPa, which is lower than the 207-228 GPa range in CeO_2 [SUZ 19]. A recent simulation work dealt with compression of individual nanoparticles. Caddeo et al. [CAD 16] calculated the mechanical properties of CeO_2 and partially reduced $CeO_{1.9}$ polyhedral nanoparticles under uniaxial compression. Fig 2.4 shows a comparison of stress-strain curves of 8 nm polyhedral NP fully oxidized CeO_2 (black curve) and reduced $CeO_{1.9}$ (red curve). It confirms that the yield stress of $CeO_{1.9}$ is lower than that of CeO_2.

Cette thèse est accessible à l'adresse : https://theses.insa-lyon.fr/publication/2022ISAL0090/these.pdf
© [R. Zhang], [2022], INSA Lyon, tous droits réservés

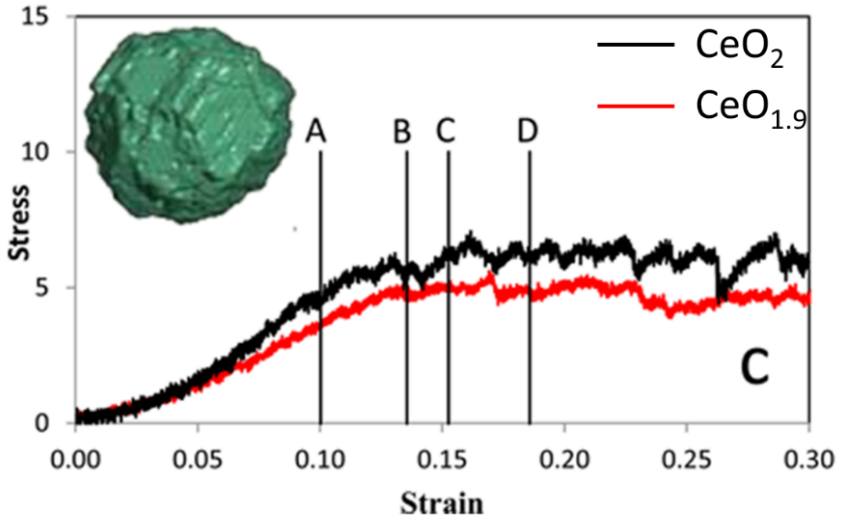

Figure 2.4 – Stress-strain curve of 8 nm polyhedral nanoparticles; fully oxidized CeO_2 (black curve) and reduced $CeO_{1.9}$ (red curve) [CAD 16].

Sample	Size (D:diameter T:thickness)	Hardness (GPa)	Young's modulus (GPa)	Bulk modulus (GPa)	Stress of transition from elasticity to plasticity (GPa)	Reference
CeO2 disk	D:10mm T:9.2mm		207-228	185-208		[SUZ 19]
CeO2 disk	D:10mm T:1mm	6.2				[TIW 18]
CeO2 disk	T:1um	15.76	213			[FRA 21]
CeO2 particles	D:5um			235	3.3	[LIU 12]
CeO2 tip	D:180nm			235	1.6	[XU 17]
CeO2 film	T:100nm	2.28	145-150	235		[ROA 09]
CeO2 film	T:100nm	21.16-22.33				[XIE 21]
CeO2 particle	D:94.6nm		54.67		5.0	[XU 22]
CeO2 particle	D:90nm		56.11		6.3	[XU 22]
CeO2 particle	D:80nm		68.71		9.8	[XU 22]

Table 2.2 – Mechanical parameters of CeO_2

Cette thèse est accessible à l'adresse : https://theses.insa-lyon.fr/publication/2022ISAL0090/these.pdf
© [R. Zhang], [2022], INSA Lyon, tous droits réservés

2.2.1 Slip systems in CeO_2 and other fluorite materials

There have already been many research studies on the determination of the slip systems in fluorite structure materials, like for instance in CaF_2, BF_2, ZrO_2, UO_2. In the literature [MUN 94], authors compressed CaF_2 single crystals along several axes at temperatures ranging from 20°C to 600°C. They showed that slips along the {100} family plane occurred more frequently. Similarly, other people observed that the glide takes place in the {100} planes and the slip direction is <110> in BaF_2 [LIU 64]. {110} is reported as secondary slip plane in another work [SHE 79]. There are also extensive studies in ZrO_2 showing that the primary slip system is <110>{100} [FRI 89] [CHE 89] [CHE 91] [DOM 91a] [DOM 91b]. Some experiments were also conducted on zirconia doped with yttria [BAU 98] [BAU 94] [BAU 95]. The compression axis was [112] in these experiments, leading to corresponding Schmid factors of 0.41 and 0.35 for {111} and {100} family planes, respectively. The results indicate that 1/2<110>{100} is the primary slip systems.

UO_2 is one of the most important fuel materials applied in nuclear reactors and is thus attracting more and more attention. There is a consensus that the slip vector in UO_2 is also ½<110> [WAN 17a]. The primary slip plane is different and many factors that may influence the slip plane in UO_2 have been taken into account. Some studies indicated that temperature and stoichiometry affect the slip system. The <110>{100} slip system is the easiest one to be activated at high temperature and low O/U ratio. The <110>{111} slip system dominates when the O/U ratio is increased and at low temperature [KEL 81]. Keller and co-workers conducted a series of experiments to find the influence of temperature on uranium oxides [KEL 88] [KEL 88]. At "low" temperature (300 K and 873 K), in all testing configurations (compression and microhardness indent), the primary glide plane family was {111}. However at higher temperatures (1273 K and 1673 K), the specimen with the same O/U ratio (2.0001) deformed along the {110} planes. The primary slip system in this work is different from the slip system commonly considered. However, the authors also indicated that the critical resolved shear stress of {100} is lower than that on {110} and {111} planes. This result is similar to the one found in CaF_2, according which the {110} planes are the least slippery planes [MUN 94].

Cette thèse est accessible à l'adresse : https://theses.insa-lyon.fr/publication/2022ISAL0090/these.pdf
© [R. Zhang], [2022], INSA Lyon, tous droits réservés

Some simulations also focused on the understanding of the slip systems of UO_2. Luc and co-workers [POR 18] studied the role of two slip systems, ½<110>{100} and ½<110>{110}, on the viscoplastic behavior of UO_2. They studied the secondary slip system ½<110>{111} as well because some experiments showed that there is a transition from the primary slip system to the secondary slip system ½<110>{111} in hyper stoichiometric UO_{2+x}. However, there was a clear difference between the experimental and calculated results, so the authors proposed that the slip system ½<110>{111} is likely to have an important impact on mechanical behavior in UO_2.

About plastic anisotropy, Sawbridge et al. [SAW 71] compressed UO_2 samples along different directions, and found that, in all cases, the Burgers vector is ½ <110> with {100} planes as primary glide planes. The experiments were conducted at 1600 K, but the primary slip system is the same than the one found in CaF_2 or BaF_2 tested at room temperature. Dislocation Dynamics (DD) [POR 20] was also used to study the mechanical behavior of UO_2 single crystals. They calculated and discussed the relationship between the sample orientation and the average strengthening coefficients. Their conclusions are consistent with the experimental results from Sawbridge's work [SAW 71]. Concerning deformation in bulk samples, the slip process is complexified due to dislocation interactions. So, the slip system in UO_2 still needs to be confirmed. Recently, Frazer et al. compressed single-crystalline UO_2 nanopillars [FRA 19b]. Cracks appeared at room temperature, while the pillar plastically deformed when the temperature increased to 350°C (0.122Tm). According to the slip traces, they indicated that the slip system is ½ <110> {100}.

In summary, in almost all cases, the slip vector in fluorite is 1/2<110> and many studies have found that the {100} planes are the primary slip planes in typical fluorite materials. However, due to the influence of other factors, such as temperature, crystal orientation, and chemical composition of the sample, research on the mechanical behavior in fluorite materials still needs to be explored.

Cette thèse est accessible à l'adresse : https://theses.insa-lyon.fr/publication/2022ISAL0090/these.pdf
© [R. Zhang], [2022], INSA Lyon, tous droits réservés

2.3 Introduction to Ce_2O_3

Under the electron beam, we have seen that CeO_2 may be reduced down to cubic Ce_2O_3 (bixbyite). Therefore, it is important to provide here information regarding the crystallographic structure and mechanical properties of such phase.

2.3.1 Crystallographic structure of bixbyite

The bixbyite structure is one of the typical cubic-defective fluorite-type structures among the anion-deficient type oxides. As shown in Fig2.5, the bixbyite structure can be obtained by removing 25 oxygen atoms from the fluorite structure. More specifically, one fourth of the oxygen anions are pushed away from their ordered positions. That is the reason why bixbyite is called an "anion-defective fluorite-type structure". Due to oxygen vacancies created by the missing oxygen atoms, the structure is distorted, as shown in Fig2.5c. One bixbyite unit cell contains eight subcells of fluorite structure that have lost two oxygen atoms. Using Wyckoff notation [WYC 63], cerium cations occupy 24d and 8b sites, and oxygen anions occupy 16c sites (Fig2.5d). Because the bixbyite structure is very similar to the fluorite structure, it is necessary to compare them to provide basic ideas and inspiration for the study of this complex structure. Table2.3 lists the atomic positions in both structures.

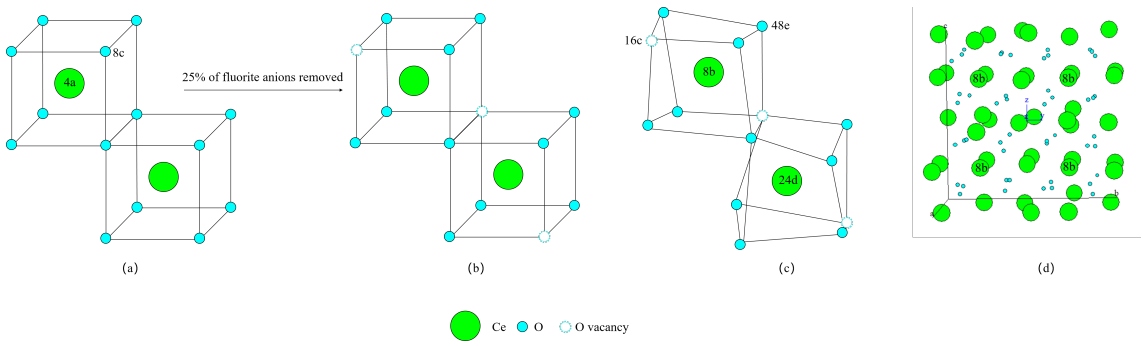

Figure 2.5 – (a) Fluorite structure in the case of CeO_2. (b) Ideal bixbyite structure in the case of Ce_2O_3. (c) Real bixbyite structure of Ce_2O_3. (d) Real bixbyite structure with one unit cell of Ce_2O_3.) .

Cette thèse est accessible à l'adresse : https://theses.insa-lyon.fr/publication/2022ISAL0090/these.pdf
© [R. Zhang], [2022], INSA Lyon, tous droits réservés

	Fluorite	Bixbyite
Space group	Fm-3m	Ia-3
Number of atoms in a unit cell	12	80
Lattice parameter	5.41Å	11.41Å
Ce position (Wyckoff notation)	4a	8b and 24d
O position (Wyckoff notation)	8c	48e and 16c

Table 2.3 – crystal structure of fluorite CeO_2 and bixbyite Ce_2O_3

2.3.2 Slip systems in bixbyite

The effect of pressure and irradiation on the stability of the bixbyite structure has been well documented in many studies. Under some conditions, the phase undergoes changes [TRA 15] [JUB 07] [MAN 74] [GAB 12] [REI 20] [GOM 14] [ISL 19]. However, there is no clear conclusion about slip systems in the bixbyite structure and the evolution of the nanostructure is rarely discussed due to its complex structure. Here we focus on the slip systems and the effect of defects on the mechanical behavior of the bixbyite structure.

In Er_2O_3 compressed at high temperature (T=0.67 Tm), dislocations with vectors 1/2<1-11> in the 110 planes were observed. The authors found dislocations as double lines, and explained this observation by dislocation dissociation [SHA 00]. Dislocations with Burgers vector 1/2<1-11> can indeed dissociate into ¼<110> and ¼<112> partials to reduce their energy. Such dissociation also occurs in Y_2O_3 at 0.58 Tm [GAB 78]. Interestingly, there is no plastic deformation observed for temperatures below 0.67 Tm. At lower temperature, the slip system <110>100 is reported in Y_2O_3 [GAB 79]. Regarding dislocations having large Burgers vectors, they were found to dissociate into four partials, which could glide in {100} planes. Table 2.4 summarizes some of the results found in the literature.

From Table 2.4, it not possible to conclude on the slip systems in bixbyite because the samples were tested under different conditions. There is still no clear conclusion about the slip systems in the bixbyite structure. Two exciting experiments are worth to be

Cette thèse est accessible à l'adresse : https://theses.insa-lyon.fr/publication/2022ISAL0090/these.pdf
© [R. Zhang], [2022], INSA Lyon, tous droits réservés

Sample	Temperature	Slip plane	Dislocation Burgers vector	Reference
Er_2O_3	T=0.67 Tm	{110}	½<111>=1/4<110>+1/4<112>	[SHA 00]
Y_2O_3	T=0.64-0.75 Tm	{110}	½<111>;<100>	[GAB 79]
Y_2O_3	T=0.58 Tm	{100}	½<111>=1/4<110>+1/4<112> ; <100>; <110> dissociated into four partials	[GAB 78]
Y_2O_3	T=0.45 Tm	{110} when compression axis is [100]	1/2<111>	[GAB 79]
Y_2O_3	Room temperature to T=0.37 Tm	{110} when compression axis is [110]	<110>	[GAB 79]
Y_2O_3	Room temperature	{100}	½<111>=1/4<110>+1/4<112>	[GAB 09]
Eu_2O_3	Room temperature	{111}	¼<011>	[NIN 90]

Table 2.4 – Slip systems reported in the literature for the bixbyite structure.

mentioned. Ye et al. [NIN 90] used HRTEM to observe dislocation movements in a Eu_2O_3 single crystal at room temperature. Under the electron beam, 60° mixed dislocations appeared on {111} planes, and they interacted with each other to form "locked" dislocations in {001} planes. A similar phenomenon was found in CeO_2, in the fluorite structure: Ding et al. [DIN 16] also observed 60° mixed dislocations formed under the electron beam, and they also observed locked dislocations. In Ye's work, the locked dislocation did not slip along the (001) plane but decomposed into two mixed dislocations again. In Ding's work, the locked dislocation annihilated at the sample surface. They supposed this phenomenon was due to the strain field induced from the phase change of the redox process under the electron beam. Table 2.5 compares their experimental conditions and results.

From Table 2.5, the environmental conditions are similar in both experiments. The results show that the Burgers vectors of the dislocations and their partials are the same, although the Burgers vectors of the dislocations in Eu_2O_3 are 1/4<011> and not 1/2 <011>, owing to its large unit cell. Regarding locked dislocation created from the interaction of 60° mixed dislocation, the Burgers vectors are the same. The only difference is

Cette thèse est accessible à l'adresse : https://theses.insa-lyon.fr/publication/2022ISAL0090/these.pdf
© [R. Zhang], [2022], INSA Lyon, tous droits réservés

Sample	CeO_2	Eu_2O_3
Structure	Fluorite	Bixbyite
Condition	Under electron beam (300 keV)	Under electron beam (200 keV)
Zone axis	[101]	[110]
Dislocation slip system	1/2 <1-10>{111} 60° mixed	1/4<011>{111} 60° mixed
Partials Burgers vector	1/6 [1-2-1]+1/6[2-11]	1/12[-112]+1/12 [121]
"locked dislocation"	1/4[-110]; Created from 60° mixed interacted with each other. Annihilated from the surface	1/4[-110]; Created from 60° mixed interacted with each other. Decomposed into 60° mixed dislocation again

Table 2.5 – Comparison of the plasticity in the fluorite and bixbyite structures, found in two works [DIN 16] [NIN 90], with the formation of locked <110> dislocations

the behavior of the locked dislocation. In CeO_2, they annihilated from the sample surface whereas in Eu_2O_3, the locked dislocation decomposed into 60° mixed dislocations again. Comparing the differences and connections in both materials with similar structures will therefore guide the study of mechanism in bixbyite structure when the slip systems are not perfectly known.

Cette thèse est accessible à l'adresse : https://theses.insa-lyon.fr/publication/2022ISAL0090/these.pdf
© [R. Zhang], [2022], INSA Lyon, tous droits réservés

Chapter 3

Material and techniques

This chapter first describes the experimental equipment, which includes the transmission electron microscope (FEI-TITAN) and the mechanical test system inside a TEM sample holder provided by Brucker/Hysitron, as well as sample information and instructions to perform compression tests.

In the second part, the processing of the data is detailed. Data are of two types: TEM images or movies obtained from the camera and mechanical data gained from the TEM sample holder. Digital imaging correlation is performed on the movies to correct the displacement of one plateau of the mechanical system during the compression experiment, thus correcting the deformation of the sample. .

3.1 Transmission electron microscopy (TEM)

Conventional imaging gives information about the morphology or structure of a material under static conditions. The dynamic evolution of the microstructure under external active fields and its relation to properties is often based on existing experience or speculation based on partial evidence. However, this often leads to a biased understanding of the real mechanisms. In order to obtain structural changes of materials in real time, many *in situ* techniques were developed, among which *in situ* X-ray techniques, *in situ* scanning electron microscopy (SEM), *in situ* atomic force microscopy (AFM), or *in situ* transmission electron microscopy (TEM). X-ray is a characterisation tool for the qualitative

Cette thèse est accessible à l'adresse : https://theses.insa-lyon.fr/publication/2022ISAL0090/these.pdf
© [R. Zhang], [2022], INSA Lyon, tous droits réservés

analysis of crystalline types, crystal parameters, crystal defects. It also allows the quantitative analysis of the relative content of different structural phases, using the position and intensity of the diffraction peaks. It is generally used for the analysis of bulk samples due to the spatial resolution in the 10 micrometers range.Scanning Electron Microscopes can present a large sample chamber. It is, thus, possible to extend their capabilities by using special stages (heating, cooling or tomographic stages...). With mechanical stages, it is possible to obtain information of mechanical properties and topography at the same time. However, with such stages, the information obtained with SEMs are only from the material surface and the spatial resolution is about 1 nm. It is not possible to characterize the inner microstructure. Compared with SEM, AFM has a very high resolution (0.1 nm)[BUT 05]. However, the scanned area size of AFM is small, leading to a very localized characterization.

The information obtained from *in situ* TEM technique is different from the methods mentioned above (X-ray SEM, AFM)). It is possible to reach the atomic resolution with TEM[HAO 18]. By performing diffraction, it is possible to characterize the structure in a precise orientation (zone axis). Defects like dislocations can be characterized, which is of much interest for the characterization of plasticity mechanisms. Coupled with EDS or EELS, chemical composition can be obtained. TEM is most widely used due to its good resolution on both time and space scales (as shown in Fig3.1).

It is worth mentioning that X-ray can have much better temporal resolution,for example,the time resolution of X-ray free-electron laser (XFEL) can achieve 15 femtoseconds. [RIV 22]

In 1926, Garbor and Busch discovered that a copper coil encased in an iron shell could refract a stream of focused electron beams [BUS 26]. They were followed in 1932 by Ruska and Knoll [KNO 32], who used this principle to built the world's first TEM. Since then, the development of TEMs has been widespread and it is today still a very important tool for researchers to analyse the microstructure of materials. The structure of a TEM is similar to that of an optical microscope. The basic imaging principle and the basic magnification principle are the same, but the light sources and lenses used are different. The light path system of a TEM consists of three main parts: the illumination unit, the imaging unit, and the observation recording unit. The illumination unit mainly consists of an electron

Cette thèse est accessible à l'adresse : https://theses.insa-lyon.fr/publication/2022ISAL0090/these.pdf
© [R. Zhang], [2022], INSA Lyon, tous droits réservés

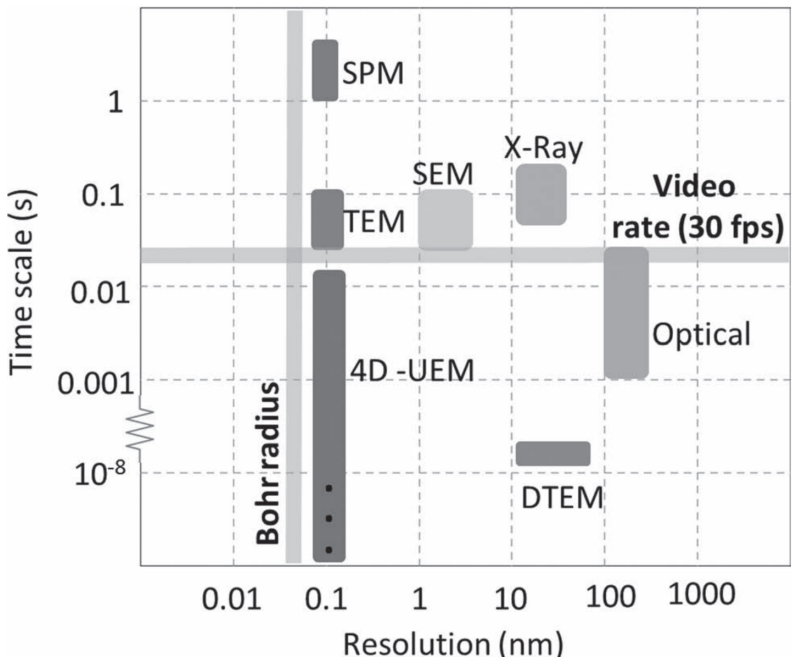

Figure 3.1 – Temporal and spatial resolution of several microscopy techniques [ESP 12],

gun which is used to emit electrons. The imaging unit consists of an objective lens, an objective aperture, intermediate lenses, a area-selection aperture, and projection lenses. The observation and recording unit consists of a fluorescent screen and/or a detector. It is worth mentioning that the development of detectors for TEM has also accelerated the widespread use of electron microscopy. This is true especially for *in situ* techniques, which need high recording speeds as well as high resolution image qualities.

3.1.1 Principles of TEM

The basic principle of transmission electron microscopy is as follows: the electron beam is emitted by an electron gun and accelerated at high voltage. Then, it passes through a multi-stage condensor lens in a vacuum, where it is concentrated into a small, sharp, uniform spot. When the sample is inserted into the microscope, the electron beam interacts with the sample while passing through it. At this time, the electron beam carrying information about the structure of the sample pass through the objective lens. The image is then magnified to the desired magnification using the lower intermediate and

Cette thèse est accessible à l'adresse : https://theses.insa-lyon.fr/publication/2022ISAL0090/these.pdf
© [R. Zhang], [2022], INSA Lyon, tous droits réservés

projection lenses. Finally, the electronic signal is collected and converted for observation using a fluorescent screen or on a camera.

Two modes can be used in a TEM: the diffraction mode and the imaging mode. The diffraction mode can be used (i) to investigate the structure of a material, (ii) to orientate the specimen in a special direction for imaging. It is obtained by adjusting the excitation current of the intermediate lenses so that their object plane is at the same height as the objective back focal plane. A representation of this mode is shown in Fig 3.2 [WIL 96] together with the imaging mode.

In the imaging mode, it is possible to select a region of interest of the specimen to perform selected area electron diffraction (SAED). The pattern of the diffraction spots in the selected area diffraction pattern can be used to determine the phase structure and crystallographic orientation of the specimen. After obtaining the diffraction spots, bright and dark field images can be obtained by using an aperture in the plane where the diffraction pattern is formed. In these images, specific regions become bright depending on the crystal orientation: non-diffracting regions appear bright in bright field, whereas regions giving rise to a specific diffraction spot appear bright in dark field.

Diffraction pattern (DP)

In a crystalline specimen, lattice planes are described by Miller indices h, k, l. The inter-lattice distance d_{hkl} (also called d-spacing) can be calculated by using a formula (which depends on the system) by considering the cell parameters and the Miller indices. A diffraction spot corresponding to a (hkl) plane appears on the diffraction pattern if the Bragg law is respected:

$$\lambda = 2d_{hkl} \sin\theta$$

where λ is the wavelength of the incident electron beam, d_{hkl} is the inter-lattice distance and θ is the angle between the incident electron beam and the lattice plane.

For cubic lattices, d_{hkl} can be calculated by considering the following relation:

$$d_{hkl} = \frac{a}{\sqrt{h^2+k^2+l^2}}$$

Fig 3.3 shows a schematic diagram of Bragg diffraction. From the diagram, we can get $|K| = 2|K_I| \sin\theta$, at the Bragg condition, $K = g_{hkl}$ where g_{hkl} is the diffraction vector.

Cette thèse est accessible à l'adresse : https://theses.insa-lyon.fr/publication/2022ISAL0090/these.pdf
© [R. Zhang], [2022], INSA Lyon, tous droits réservés

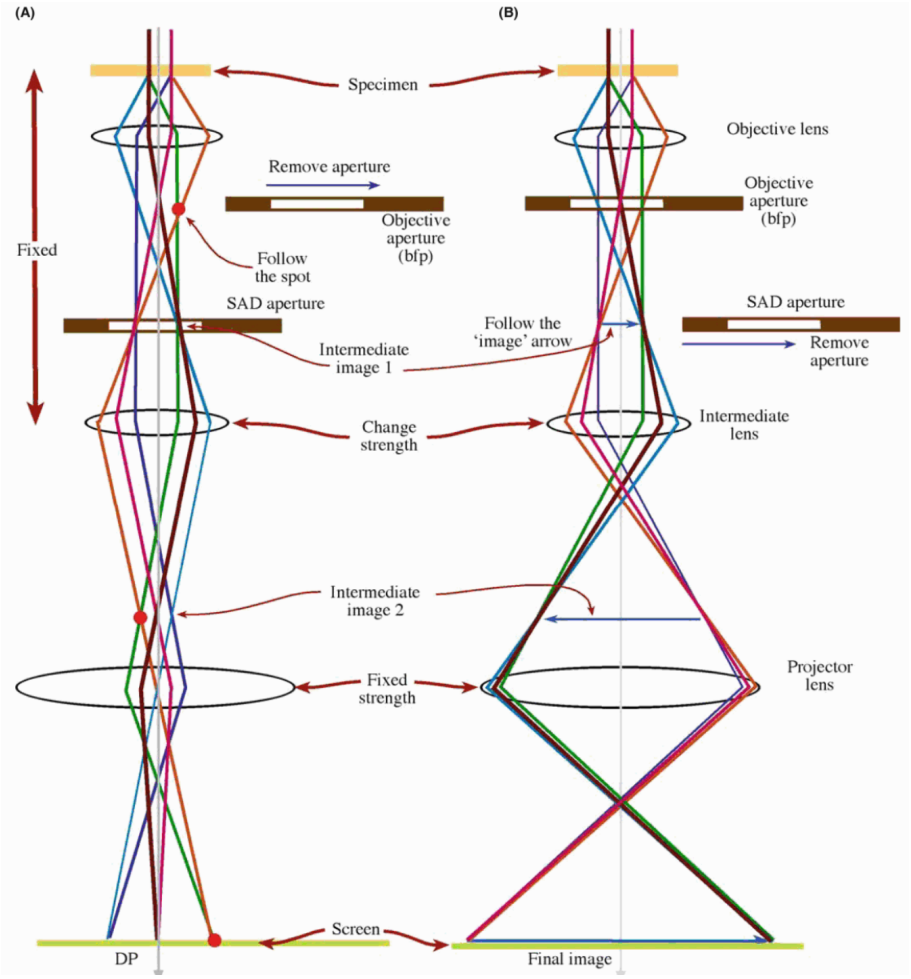

Figure 3.2 – Sketch of the two main TEM modes: diffraction mode (left) and imaging mode (right) [WIL 96].

Furthermore, we can find a relation between g_{hkl} and d_{hkl}:

$$|g_{hkl}| = \frac{1}{d_{hkl}}$$

From the formula above, it can be seen that the diffraction pattern can be indexed if the crystal plane distances and angles are known. Using the diffraction pattern, we can then determine the orientation of the sample in the TEM images. In addition, it is especially important in high-resolution imaging to mark out the crystallographic planes. It is necessary to note that a lattice plane can be described by a vector perpendicular to the plane (with its norm equal to the inverse of the d-spacing), and this vector belongs to the reciprocal lattice, which is the Fourier transform of the direct lattice. Fig3.4 gives

Cette thèse est accessible à l'adresse : https://theses.insa-lyon.fr/publication/2022ISAL0090/these.pdf
© [R. Zhang], [2022], INSA Lyon, tous droits réservés

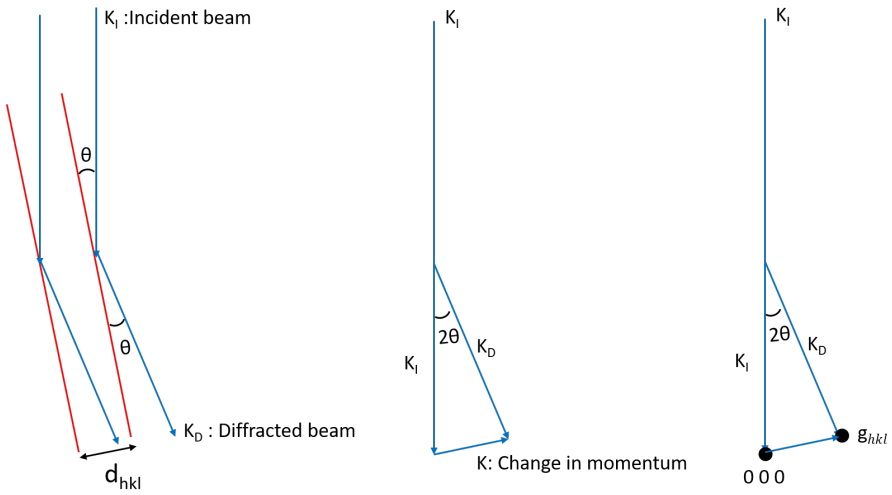

Figure 3.3 – schematic diagrams of Bragg's law

some examples of diffraction patterns. Fig3.4(a) displays the diffraction pattern from a pure titanium plate which has a δ-FCC structure. The dark field image was obtained using the g-vector [220]. Fig3.4(b) and (c) show diffraction patterns of CeO_2 and Ce_2O_3, which are the specimens studied in this work.

Dark field (DF) imaging

Fig3.5 show differences in the position of the objective aperture, between bright field and dark field imaging modes. Bright field imaging is formed by selecting only the direct wave. Dark field imaging is formed by choosing a single diffraction wave. This is achieved by inserting an small objective aperture in the image focal plane of the objective lens.

Dark-field images are helpful for observing defects such as dislocations, stacking faults, and twins, because the dark-field image comes from a selected diffracted wave, corresponding to a specific crystal plane. In the defective areas, the electrons are diffracted in a different direction than in the perfect areas, thus allowing the defective areas to be clearly visible in the dark field image. The bright-field image, on the other hand, is less sensitive to defects because it is formed using the direct wave. Moreover, because there is a fairly wide range of strain fields in the dislocation where the crystal plane is close to satisfying the Bragg condition, the dislocations visible in bright-field images look like diffraction bands wider than the real dislocations.

Cette thèse est accessible à l'adresse : https://theses.insa-lyon.fr/publication/2022ISAL0090/these.pdf
© [R. Zhang], [2022], INSA Lyon, tous droits réservés

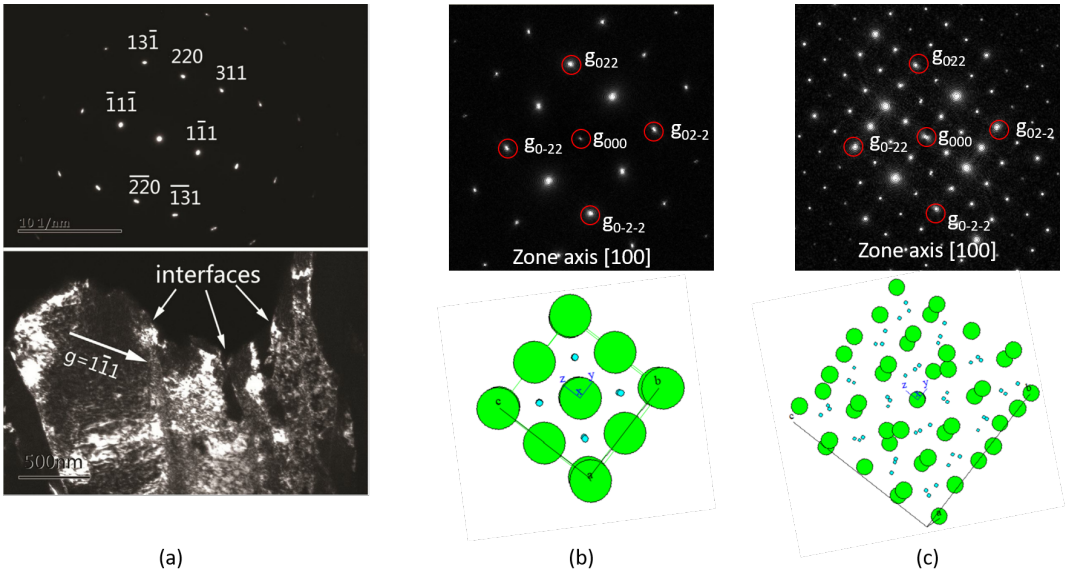

Figure 3.4 – Examples of cubic diffraction patterns. (a) Top: Area-selected diffraction pattern of the Ti δ-FCC phase. Bottom: dark field image using the g-vector [220][LI 18]. (b) Top: Diffraction pattern of the CeO_2 nanocubes used in this work. Bottom: Crystal structure with the same orientation (zone axis [100]). (c) Top: Diffraction pattern of the Ce_2O_3 nanocubes used in this work. Bottom: Crystal structure with the same orientation (zone axis [100]).

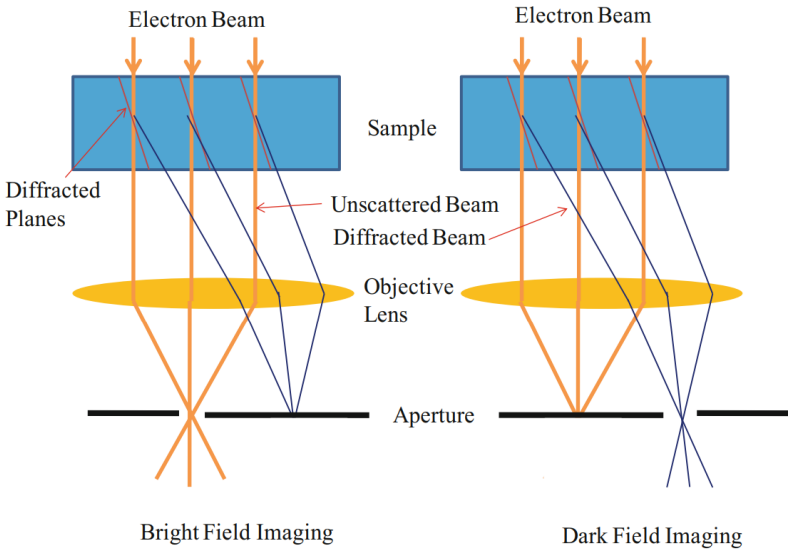

Figure 3.5 – Diagrams of bright-field imaging and dark-field imaging[JAV 18]

Cette thèse est accessible à l'adresse : https://theses.insa-lyon.fr/publication/2022ISAL0090/these.pdf
© [R. Zhang], [2022], INSA Lyon, tous droits réservés

The **g**·**b** rule describes the visibility of a dislocation depending on the imaging conditions. If the Burgers vector **b** of a dislocation is perpendicular to the diffraction vector **g** used for dark field imaging, g·b=0, there is no diffraction contrast from the dislocation. The dislocation is therefore invisible.

3.1.2 Environmental transmission electron microscope (ETEM)

In a transmission electron microscopy (TEM), an electron beam passes through the sample and forms an image afterwards. Due to the high vacuum requirement of the electron gun and the influence of interactions between electrons and gas molecules on imaging, transmission electron microscopes must be used under high vacuum conditions, so they can only be used to analyze the microstructure of sample in vacuum. In order to obtain the microstructure of the material under atmospheric conditions, it is necessary to confine the gas near the sample while other parts of electron lens barrels maintaining the high vacuum state. This kind of electron microscope is called environmental transmission electron microscope (ETEM). The common ETEM scheme is to transform the sample chamber area, using a differential pump (differential pumping system) and pressure-limiting apertures system, as shown in Fig3.6. By adding pressure-limiting apertures above and below the sample chamber, the gas around the sample can only pass through the small holes of the pressure-limiting apertures. The pressure-limiting apertures is vacuumed by a multi-stage differential pump to keep the other parts of the lens barrel under high vacuum.

In this work, we use a TITAN G2 80-300 kV environmental electron microscope from FEI company, operating at 300 kV (Fig3.7). The sample chamber can reach a pressure of up to 20 mPa but experiments under high vacuum can still be performed.
During the *in situ* experiments, the microscope is generally operated under vacuum. Videos are recorded with a Gatan Oneview camera, as stacks of 4k*4k images with 25 frames per second. The images are usually recoded in the bright field mode.

Cette thèse est accessible à l'adresse : https://theses.insa-lyon.fr/publication/2022ISAL0090/these.pdf
© [R. Zhang], [2022], INSA Lyon, tous droits réservés

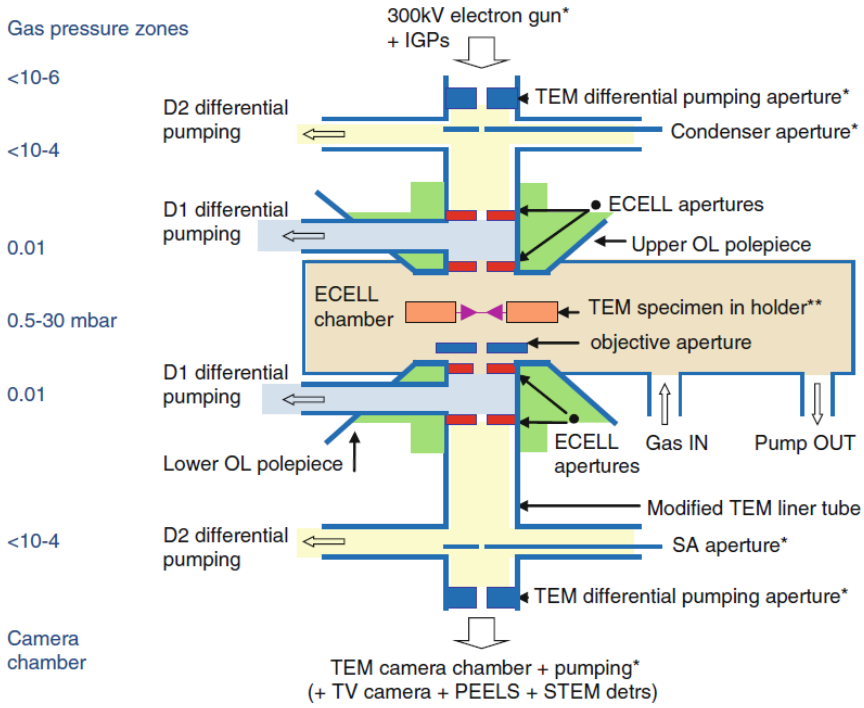

Figure 3.6 – Schematic Diagram of an Environmental Transmission Electron Microscope [HAN 16]

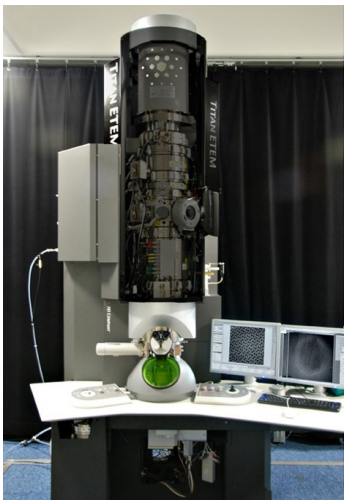

Figure 3.7 – Picture of the FEI Titan Environmental Transmission Electron Microscope of the CLYM

Cette thèse est accessible à l'adresse : https://theses.insa-lyon.fr/publication/2022ISAL0090/these.pdf
© [R. Zhang], [2022], INSA Lyon, tous droits réservés

3.2 *In situ* mechanical testing methods in TEM

In order to characterize the microstructure evolution of materials under sollicitation, *in situ* transmission electron microscopy (*in situ* TEM) technology is considered here. *In situ* TEM is a technology that applies an external excitation (such as force, heat, electricity, atmosphere, etc.) on the sample in a regular transmission electron microscope, so that the scientist observes and records the changes occuring in the sample in real time. *In situ* TEM can not only provide information on the structural dimension of the material, but also obtain some properties of the material and the one-to-one correspondence relationship between the properties and the structure in real time. Through *in situ*, quantitative, and dynamic experiments, we can better understand the microscopic process of material structure changes, which is crucial for discovering new phenomena, revealing new mechanisms, verifying new principles, and obtaining new evidence.

There are some mechanical testing devices that can be used inside TEM. One possible mechanical testing device is presently a series of sample holders from the company Bruker/Hysitron. A typical sample holder is composed of a sensor measuring the normal load and the displacement of the tip, thus providing force-displacements data. These data can be coupled with images recorded in real-time. The indenter is connected to a three-level controller (mechanical adjustment coarse control, piezoelectric ceramic to achieve fine adjustment, force-displacement sensor for fine adjustment and measurement) which can accurately adjust the position of the indenter, and can control the measurement of the force and displacement of the indenter. By modifying the shape of the indenter, mechanical tests could be performed on samples with different geometries in the literature, among which compression of films [MIN 06], compression of nanoparticles [HAN 15], compression of micro-nano-scale columnar samples [HUA 11], fatigue fracture tests on micro-nano scale cantilever samples [WAN 15b] and many other *in situ* quantitative mechanical tests.

On the basis of the mechanical test device, some researchers used MEMS technology to develop test chips with specific functions to realize quantitative mechanics tests on special samples. For example, Hysitron launched in 2012 a "push-to-pull" device that can quantitatively stretch nanowires *in situ* [GUO 11].This device can convert the compressive stress

Cette thèse est accessible à l'adresse : https://theses.insa-lyon.fr/publication/2022ISAL0090/these.pdf
© [R. Zhang], [2022], INSA Lyon, tous droits réservés

of the indenter into the tensile stress on the sample. It was used to carry out stretching of micro-nano-scale T-shaped samples [LIU 14], quantitative *in situ* stretching of nanowires [WAN 15a] and thin films [FRA 19a]. These research revealed the plastic deformation mechanisms of submicron-sized crystals. They help to develop crystal plasticity theory, design micro devices and predict their reliability.

3.2.1 Nanocompression TEM sample holder (Hysitron PicoIndenter 95)

In this work, we used a PI95 nanomechanics test system (PicoIndenter 95), which is a system developed by Bruker/Hysitron for *in situ* quantitative mechanical testing of micro/nano materials (see Fig 3.8). The sample holder used can be fitted in the Titan ETEM microscope of the Consortium Lyon Saint-Etienne de Microscopie (CLYM). Quantitative force-displacement curves obtained by the sensor of the picoindenter coupled with the corresponding real-time video recorded by the camera of the microscope give interesting pieces of information to better understand the behavior of materials at the nanoscale, and particularly their plastic behavior. The indenter is controlled by three-stage transmission systems. The first stage is the mechanical control, which can ensures coarse movements of the indenter using three knobs along the X, Y and Z directions. The second stage is the piezoelectric ceramic control unit, which can precisely adjust the indenter in three directions using piezoelements controlled through the software. The movement accuracy along X,Y could reach 2 nm and 0.1 nm along the Z direction. The third stage is the sensor unit - the transducer -, which has an electrostatic comb structure. It can only move along the Z direction in an accurate way and at the same time can measure the normal load. Table 3.1 gives the characteristics of this holder.

Holder	Max Force	Force Noise Floor	Max Displacement	Displacement Noise Floor	Fine Positioning Range X/Y/Z	Fine Positioning Sensitivity X/Y/Z
PI 95	1 mN	<0.2 μN	1μN	<1nm	50/50/3μm	2/2/0.1nm

Table 3.1 – Features of PI 95 holder provided by Bruker/Hysitron

As the core part of the holder, the transducer is designed with a three-plate capacitance for a high test sensitivity, a large dynamic range and linear force and displacement output

Cette thèse est accessible à l'adresse : https://theses.insa-lyon.fr/publication/2022ISAL0090/these.pdf
© [R. Zhang], [2022], INSA Lyon, tous droits réservés

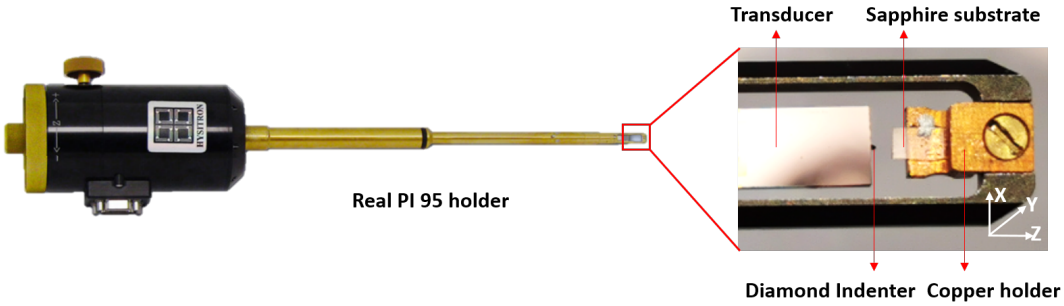

Figure 3.8 – Picture of the PI95 holder with an enlarged view of the front of the sample rod

signals. The maximum displacement can reach 3 μm in the compression axis and the maximum force can reach 1 mN. The basic working principle is shown in Fig3.9, including the upper, middle and lower capacitance plates. The upper and lower capacitor plates are fixed and the middle capacitor plate is movable and connected to the indenter. The displacement measurement is based on the principle of applying a 180° inverted AC signal to the upper and lower fixed capacitor plates. As the fixed plates are parallel to each other, the change in potential between the plates can be considered as a linear change in the signal applied to the fixed plates at any given time. They are equal in magnitude but opposite in polarity, so that the fixed plates have the maximum potential and the minimum potential between them is zero. The input impedance of the system is significantly greater than the output impedance, so when the position of the intermediate capacitor plate changes, its potential also changes, so the displacement of the intermediate plate can be calculated by measuring the change in the final potential.

A large DC voltage, up to 600 V, is applied to the lower fixed capacitor plate, causing an intermediate capacitor plate and a lower capacitor plate to electrostatic attraction between the capacitor plates, so that the middle capacitor plate is forced to move downwards. The magnitude of the force can be calculated from the value of the applied voltage. In addition, it is important to note that, in practice, many factors can affect the parameters of the sensor. For instance, changes in humidity in the laboratory can affect the dielectric constant of the medium and thus the performance of the sensor. It is therefore necessary to carry out a calibration prior to the experiment using the standard calibration procedure

Cette thèse est accessible à l'adresse : https://theses.insa-lyon.fr/publication/2022ISAL0090/these.pdf
© [R. Zhang], [2022], INSA Lyon, tous droits réservés

for the sensor.

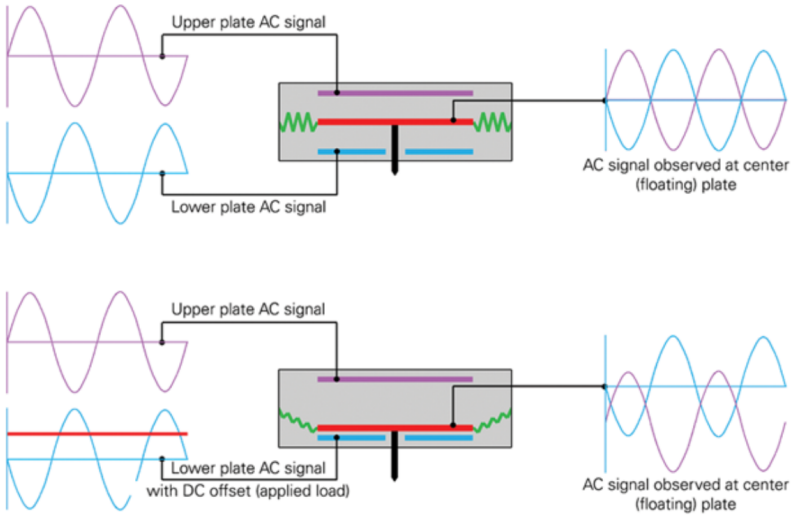

Figure 3.9 – Schematic diagram of the working principle of the PI-95 transducer

In this work, *in situ* compression experiments are performed using a Brucker/Hysitron PI95 mechanical holder, equipped with a diamond flat punch indenter of flat size around 400-700 nm. The loading mode is displacement control mode, and the loading rate is set to 0.1-0.5 nms^{-1}.

3.3 Sample preparation

The cerium oxides nanocubes studied in this PhD work are kindly provided by Frédéric Chaput from the Chemistry Laboratory at ENS Lyon. More details about synthesis methods is described in the literature [TRE 19].

Sample preparation is a key step to perform compression tests inside the TEM without some artifacts due to the small compression system. It is roughly divided into four steps, as shown in Fig3.10. First, a hard and end-flat substrate is prepared. Next, the substrate needs to be glued to a copper pallet. Afterwards, the particles are spread on the substrate cross-section. Finally, the copper pallet can be fixed to the sample holder with a small screw. After introducing the sample holder inside the TEM, the indenter (tip) is approached close to the sample and its height is adjusted to align it with the particle of

Cette thèse est accessible à l'adresse : https://theses.insa-lyon.fr/publication/2022ISAL0090/these.pdf
© [R. Zhang], [2022], INSA Lyon, tous droits réservés

interest.

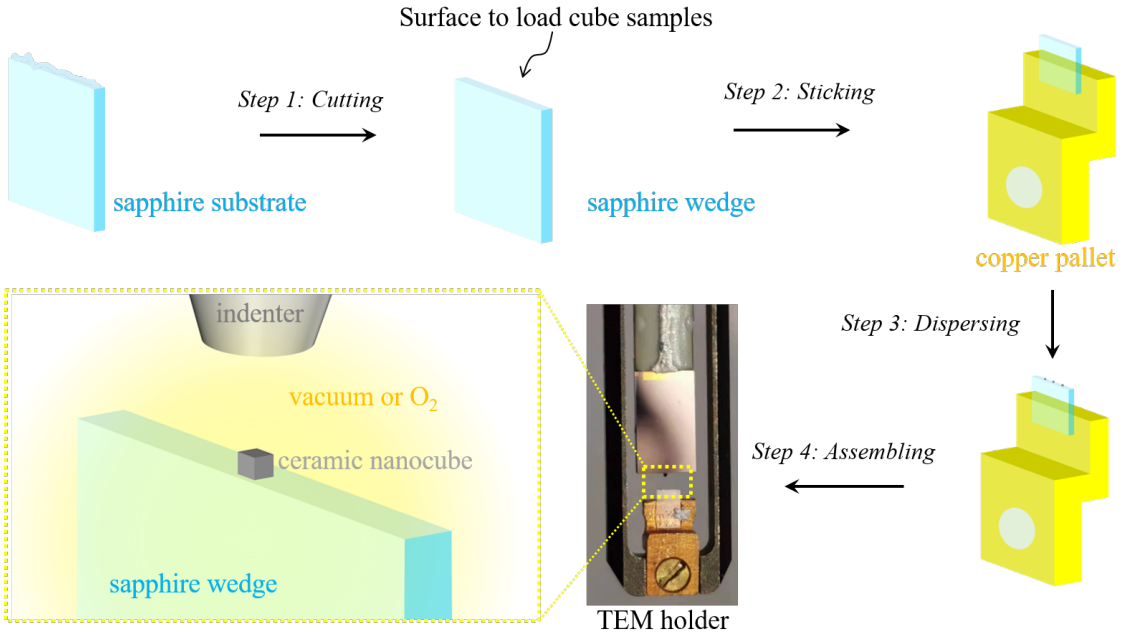

Figure 3.10 – Schematic Diagram of the sample preparation and sample mounting used to perform *in situ* mechanical tests in TEM

■ **StepI - Preparing the sapphire substrate**

In order to guarantee the same compression conditions on both sides of the nanocube and to minimize the effect of the substrate on the mechanical data [OUY 09], a sapphire substrate is chosen. Its surface is polished using an Ilion II wide-beam argon milling system (Gatan) that is commonly used for samples requiring large-area polishing. Comparing the pictures of the sapphire substrate before and after polishing (Fig3.11), a smooth surface is obtained.

■ **StepII - Sticking the sapphire substrate on a copper pallet**

The next step requires to glue the sapphire substrate on a copper pallet. For better adhesion, the copper pallet is first cleaned with acetone. A very small amount of hot melt crystal adhesive is used for bonding. This glue is very easy to solidify and very stable. However, its electrical conductivity is not good, so usually we apply

Cette thèse est accessible à l'adresse : https://theses.insa-lyon.fr/publication/2022ISAL0090/these.pdf
© [R. Zhang], [2022], INSA Lyon, tous droits réservés

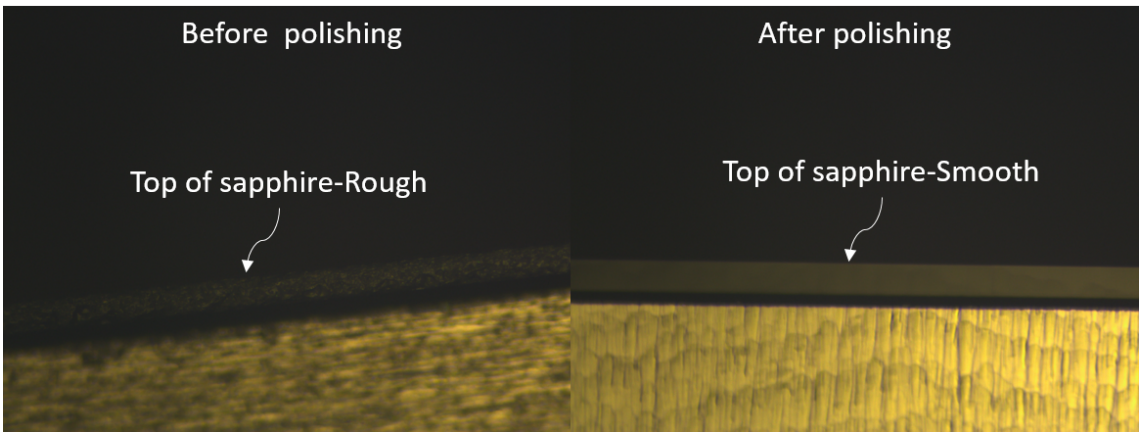

Figure 3.11 – Comparison of the sapphire substrate surfaces before and after argon beam polishing

a little amount of silver glue to strengthen the conductivity between the substrate and the copper pallet. Silver glue is usually applied to the end of the sapphire substrate, and the copper pallet connection part.

■ **StepIII - Depositing well-dispersed CeO_2 nanocubes on the sapphire substrate**

The dispersion of the nanocubes on the substrate is a very critical step. Cerium nanocubes are usually agglomerated. However, the compression test requires isolated particles and a certain distance between these isolated nanoparticles is necessary since the indenter tip is relatively large. Indeed during the compression, only one particle should be compressed to ensure that the mechanical data recorded are only those of the tested particle.

A thin thread is used for the dry deposition of nanoparticles onto the sapphire substrate. Different threads can be envisaged: human hair or small animal hair, such as cat beard. The chosen thread is first cleaned with alcohol then dipped in the sample powder. It should not be dipped too much, but just enough to see particles on it with the naked eye. Before dabbing particles onto the substrate, it is best to gently shake the thread to remove large particle clusters, to avoid the large parti-

Cette thèse est accessible à l'adresse : https://theses.insa-lyon.fr/publication/2022ISAL0090/these.pdf
© [R. Zhang], [2022], INSA Lyon, tous droits réservés

cle clusters from adhering to the substrate. Next, the thread is gently rubbed on the substrate cross-section just a few times. To further clean up the large particle clusters, it is necessary to sweep the surface of the substrate gently with a clean, fine thread, usually two or three times.

After completing the steps above, the sample dispersion is checked in TEM. If no isolated nanocubes are found, then the steps above are repeated until a suitable dispersion is found.

■ **StepIV - Compression experiment**

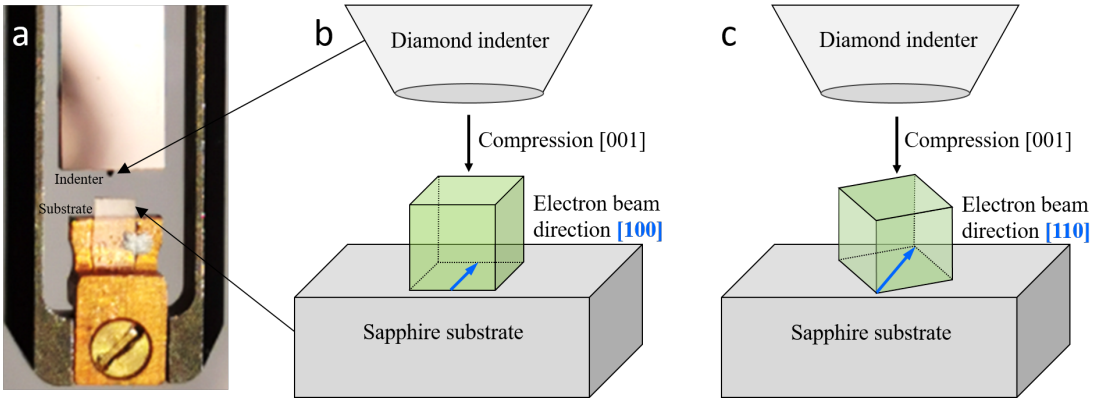

Figure 3.12 – Scheme of the experimental setup. (a) Picture of the front end of the TEM holder with a diamond indenter. (b) Scheme of the compression experiment with electron beam direction [100] and (c) Scheme of the compression experiment with electron beam direction [110].

In this work, nanocubes are observed along two zone axes: [100] or [110], as shown in Fig3.12. With the nanocube geometry,the compression direction remains the [001] direction. With this configuration, we can calculate the Schmid factor of the different slip systems in CeO_2. As shown in Fig3.13, when the compression direction is [001], the Schmid factor of the slip system <110>{100} is nil, indicating that the slip system <110>{100} is not activated with the force direction [001]. The <110>{100} is normally considered the primary slip system in the fluorite structure, but the priority of <110>{110} and <110>{111} is not well studied, so we focus

Cette thèse est accessible à l'adresse : https://theses.insa-lyon.fr/publication/2022ISAL0090/these.pdf
© [R. Zhang], [2022], INSA Lyon, tous droits réservés

on the <110>{110}, <110>{111} slip systems in this work.

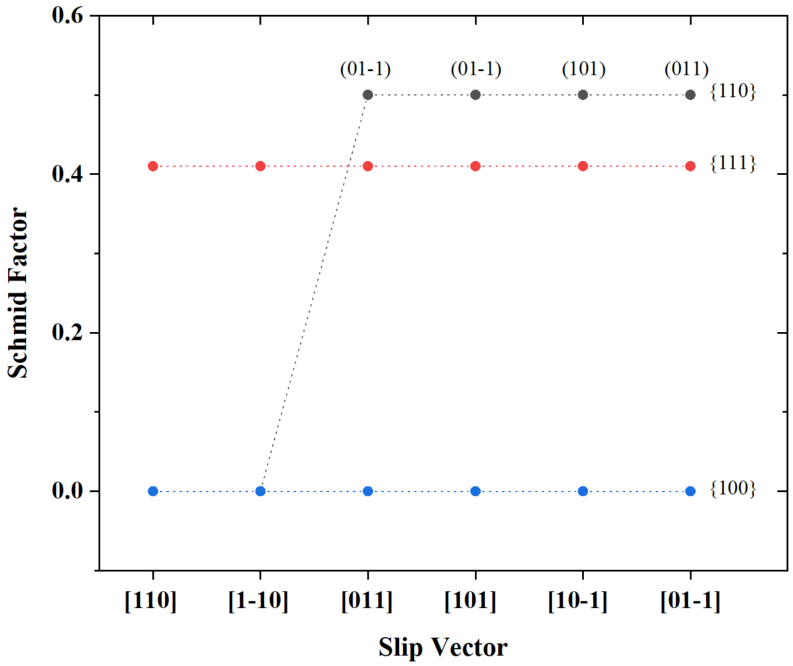

Figure 3.13 – Schmid factors for different slip systems.

Cette thèse est accessible à l'adresse : https://theses.insa-lyon.fr/publication/2022ISAL0090/these.pdf
© [R. Zhang], [2022], INSA Lyon, tous droits réservés

3.4 Data processing

During the compression test, the displacement of the indenter and the force applied are recorded. Meanwhile, the TEM images are acquired. The image acquisition is usually fixed to 25 frames per second. When analyzing the relationships between microstructural changes and the mechanical behavior, it is necessary to correlate the video with the mechanical curves. Before obtaining the correlation *in situ* video, the following steps need to be completed.

- **StepI - Compiling the images to create a compressed video**

  4k*4k images are saved in the DM4 format. This format allows high resolution imaging and is useful to monitor dislocations or stacking faults but it is a heavy format (66 Mo per image). To build a movie from the images, the images are first converted from DM4 to jpg. Afterwards, the compressed video is obtained in Matlab by using the same frame rate. As some cubes are tested with very low electron dose rates, the brightness and contrast are sometimes increased.

- **StepII - Processing mechanical data**

  Data recording typically begins when the indenter is very close but not in contact with the nanocube. At the end of the test, we need to reset the starting point at the point where the indenter touches the sample. We choose the point for which the force starts to increase significantly as the zero point.

  As mentioned in Chapter 1, the force-displacement curve is converted to a stress-strain curve. The engineering stress is obtained by dividing the force by the initial nanocube area in contact with the indenter. It is assumed that the nanocube is a perfect square and the lateral cube size is measured directly on the image. The engineering strain is defined as the displacement divided by the initial cube size.

- **StepIII - Measuring the real displacement**

  In order to be more accurate about the amount of nanocube deformation, digital image correlation (DIC) is applied on the compression video. The Matlab code

Cette thèse est accessible à l'adresse : https://theses.insa-lyon.fr/publication/2022ISAL0090/these.pdf
© [R. Zhang], [2022], INSA Lyon, tous droits réservés

used was developed in I. Issa's PhD thesis [ISS 16]. DIC processing results in new displacement data. In order to draw the calibrated mechanical curve, we use the displacement measured using DIC and the force acquired from the transducer of the sample holder. However, the number of data points from the sample holder is eight times more than the number of data points from DIC, so the number of points corresponding to the force points needs to be reduced. Hence, we take the average of eight consecutive points as new force data. This way we have the same number of displacement data points and force data points, and the noise is reduced. The last step is to match both sets of data in a time standard to get the calibrated stress-strain curve.

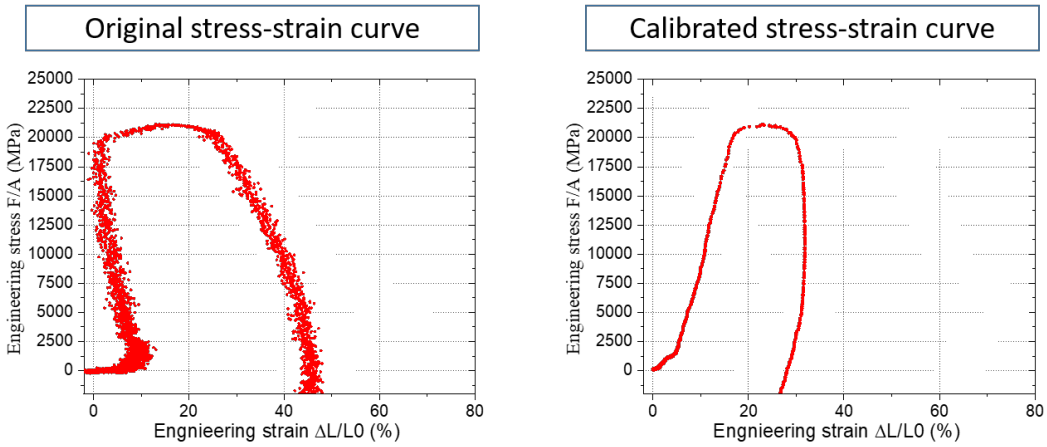

Figure 3.14 – Comparison of stress-strain curves before and after DIC. The left graph shows the original stress-strain curve, the right one is the curve after DIC processing.

An example is given in Fig3.14 to compare the mechanical curves before and after calibration. In the graph on the left, the stress-strain curve is drawn using the original data points, directly obtained from the sample holder sensor. The right part of the figure is the stress-strain curve after displacement calibration using DIC. Since the force is only averaged, the engineering stresses are not changed. On the contrary, the strain change a lot upon calibration. This is very important to get accurate measurements.

Cette thèse est accessible à l'adresse : https://theses.insa-lyon.fr/publication/2022ISAL0090/these.pdf
© [R. Zhang], [2022], INSA Lyon, tous droits réservés

To briefly summarise this chapter, *in situ* TEM compression experiments of cerium oxides are conducted with a dedicated sample holder (PI95 Hysitron) inside an environmental transmission microscope (TITAN FEI). The cerium oxides particles are provided by Frédéric Chaput from the Chemistry Laboratory at ENS Lyon. All particles tested keep the same direction of compression: [001]. The tests are performed in the displacement-controlled loading mode, with a loading rate set between 0.1 nm/s and 0.5 nm/s. The displacement data from the sample holder needs to be processed by DIC and then combined with compression video to obtain in-situ video.

Cette thèse est accessible à l'adresse : https://theses.insa-lyon.fr/publication/2022ISAL0090/these.pdf
© [R. Zhang], [2022], INSA Lyon, tous droits réservés

Chapter 4

In situ Nanocompression of CeO_2 nanocubes

In this chapter, we first characterize the ceria nanocubes in terms of crystallographic phase, size distribution and facet types. Moreover, we discuss the evolution of several microstructural parameters (phase, facets, oxygen content) as a function of the electron dose rate and the nanocube size. This allows the determination of experimental conditions under which the fluorite phase is preserved.

In the second part, we present the results obtained from *in situ* mechanical tests on fluorite nanocubes. The slip systems are discussed in light of the BF images acquired during the test and using DF images acquired after the test with different zone axes.

The last part of this chapter deals with the effect of the nanocube size on the yield stress.

4.1 Characterization of the nanocubes in TEM

4.1.1 Characterization of CeO_2 in TEM

Fig4.1 presents two zone axes used to observe the nanocubes deposited on the sapphire substrate: [100] and [110]. Due to geometrical constraints, the zone axes [100] and [110] could be reached on the same cube by rotating the sample holder by 45° around the axial direction [001], only if one zone axis is reached with a tilt of -20°. In such configuration,

Cette thèse est accessible à l'adresse : https://theses.insa-lyon.fr/publication/2022ISAL0090/these.pdf
© [R. Zhang], [2022], INSA Lyon, tous droits réservés

the (001) facet of the nanocube is in contact with the susbtrate and the compression direction remains [001]. Fig4.1a shows TEM images and the corresponding diffraction patterns, obtained with both zone axes. A locally magnified high-resolution image is at the extreme right. During the experiments, we noticed that the zone axis [100] is close to two beam condition, which is favorable for the observation of dislocations at "low" magnification. The zone axis [110] is more suitable to see dislocations and stacking faults in high resolution images.

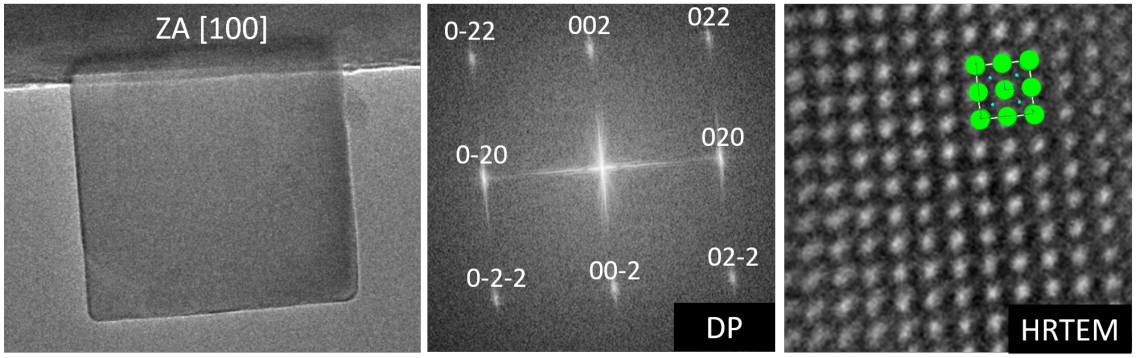

(a)

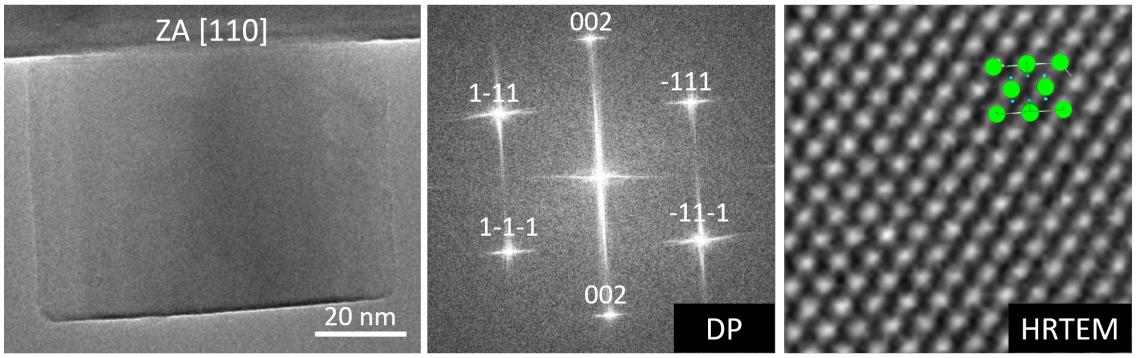

(b)

Figure 4.1 – The images from left to right are: TEM images, diffraction patterns (DP) and high-resolution TEM (HRTEM) images of CeO_2 nanocubes along different zone axes(Top is from ZA [100], bottom is from ZA[110]). Both zone axes can be used for the analysis of the same cube only if one zone axis is observed with a tilt of the sample holder of -20°

To reach atomic resolution, scanning transmission electron microscopy (STEM) was also used (Fig4.2). Compared with the TEM mode, the use of the STEM mode with an

Cette thèse est accessible à l'adresse : https://theses.insa-lyon.fr/publication/2022ISAL0090/these.pdf
© [R. Zhang], [2022], INSA Lyon, tous droits réservés

appropriate dwell time can help to reduce significantly damage in the sample due to the electron beam, and can greatly improve the contrast in the image.

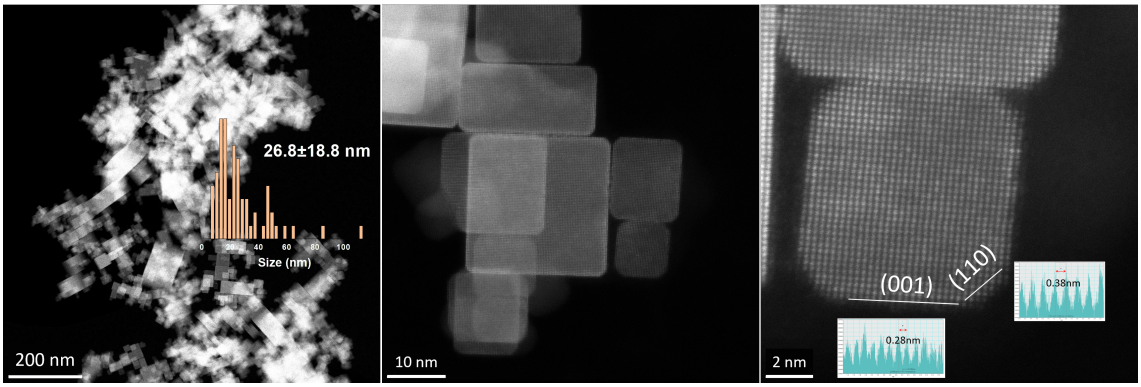

Figure 4.2 – STEM images at different magnifications. (a) low magnification image with particle size distribution. (b) nanocubes observed along the [100] zone axis. (c) High magnification image, reaching the atomic resolution, of the cube at the botton left part of image (b). The insets confirm the distance of the (100) and (110) planes

The inset in the low magnification image shows the measured distribution of the nanocube sizes. This distribution shows two major contributions: the main one around 26.8 nm and another one around 100 nm. The size distribution reveals that the sample contains a small quantity of big cubes. One important point to notice is that these big cubes are usually surrounded by many small cubes, which are not easy to measure because they overlap each other. Small nanocubes are generally in the edge of the larger particles, which make them easy to be measured. For this reason, the average size of the particles measured is rather small. During *in situ* experiments, we want to compress isolated nanocubes. Since the big ones are always surrounded by other small cubes or contaminants, the number of mechanical tests on big nanocubes is expected to be lower than that on small nanocubes.

In addition, we observe that the smaller the particles in the initial state of the sample, the more likely they are to present {110} planes. As seen in the Fig4.3, the small particle (right) has fewer cubic features than the large particle (left) since it presents more {110} facets. Almost all cubes present {110} planes but the fraction of these {110} planes is smaller in larger cubes. In the compression experiments, for the small size samples we

Cette thèse est accessible à l'adresse : https://theses.insa-lyon.fr/publication/2022ISAL0090/these.pdf
© [R. Zhang], [2022], INSA Lyon, tous droits réservés

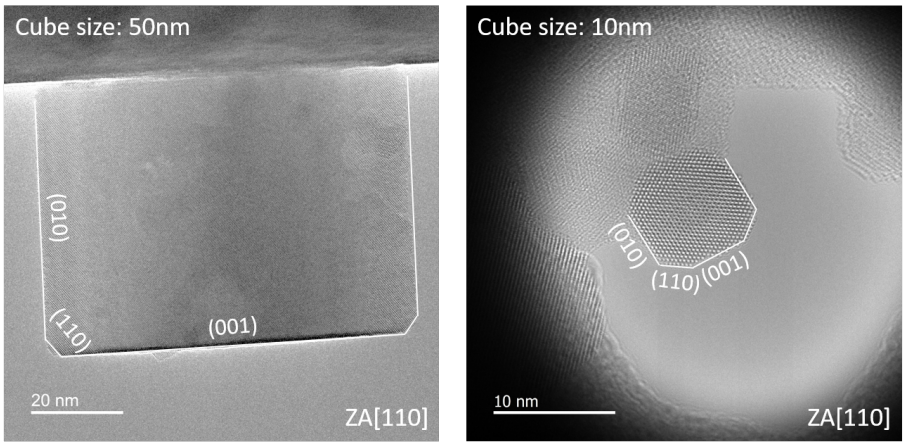

Figure 4.3 – The distributions of planes {001} and {110} differ between small and large cubes.

choose the more cubic particles as the compression objects.

4.1.2 Electron beam effect on the nanocube structure

The electron beam has a reducing effect on the CeO_2 particles, but at the same time we found that different planes and particle size have an effect on the reduction. They are further described in this section.

■ Effect of the electron dose on the nanocube phase

Some studies [HAO 18] [WU 04] have reported that the particle size has an effect on CeO_2 chemical composition. The small size is more favorable to Ce^{4+} reduction into Ce^{3+}, since reduction occurs especially on surface areas. In this work, several nanocubes are irradiated under the e-beam and their phase changes are monitored by following the diffraction pattern evolution.

Fig4.4 shows images of CeO_2 particles of different sizes before and after being exposed to irradiation (4.8×10^5-1.5×10^9 e/Å^2) for the same amount of time (20 s). The left part of the image shows a large particle (16 nm) and a small one (6 nm) without phase change under irradiation. From their DP, no superlattice diffraction points appear (characteristics of a phase change to the bixbyite structure), which means that the crystal is still in the original structure (Fluorite, Fm-3m space group). However, on the right part of the image, phase transition occurs in nanocubes of similar sizes (27 nm and 8 nm).

Cette thèse est accessible à l'adresse : https://theses.insa-lyon.fr/publication/2022ISAL0090/these.pdf
© [R. Zhang], [2022], INSA Lyon, tous droits réservés

From the example presented above, it is difficult to conclude on a relation between nanocube size and phase transition. Therefore, we analyzed the behaviour of 16 particles. The irradiation time was not always the same among the particles counted. However, it can be guaranteed that the particles which did not undergo phase change were all irradiated during more than 20 minutes. For the particles that underwent phase change, the times corresponding to phase change were always less than 20 minutes.

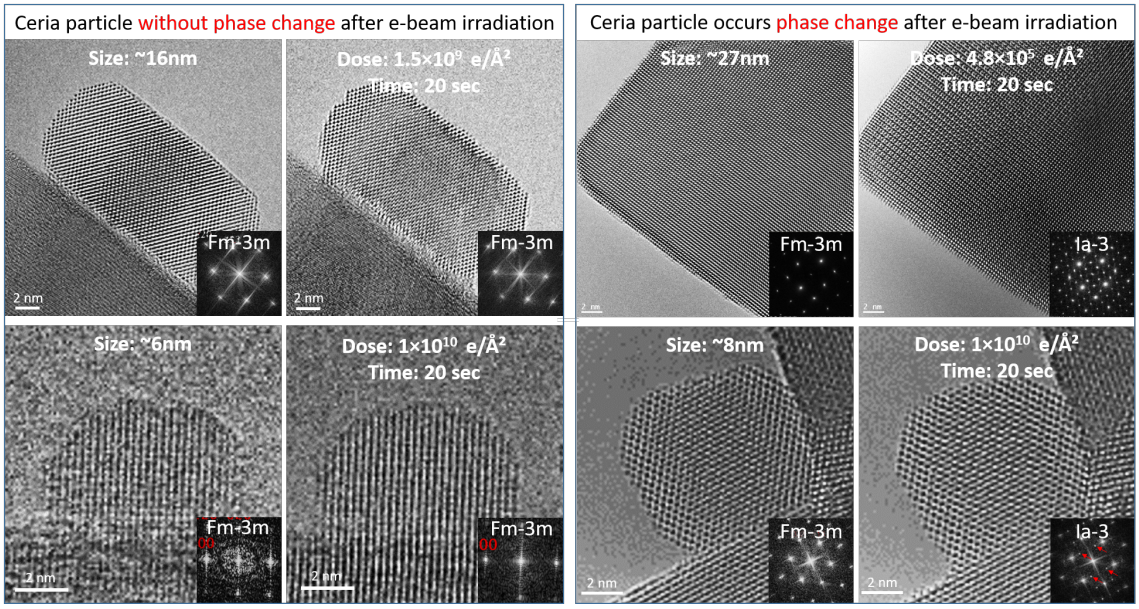

Figure 4.4 – effect of the same irradiation duration (20 s) on different CeO_2 nanoparticles. In the left square, the particles did not exhibit any phase change while on the right one, a structural change from CeO_2 to $CeO_x(1.5 \leq x < 2)$ is observed.

The analysis of many particles allows the study of the effect of the particle size and the electron dose on the phase change under electron beam irradiation. Fig4.6 sums up the electron beam effect on the phase transformation of particles of different sizes. It should be noted that small particles were tested at both high and low dose rates, but the large particles were only tested at low dose rate. Fig4.5 plotting the relationship between the e-beam rate and TEM magnification shows that they are exponentially related. The higher magnification, the greater e-beam intensity exposed on the sample. Indeed, with the same magnification in TEM, it is more difficult to obtain high electron dose rates for

Cette thèse est accessible à l'adresse : https://theses.insa-lyon.fr/publication/2022ISAL0090/these.pdf
© [R. Zhang], [2022], INSA Lyon, tous droits réservés

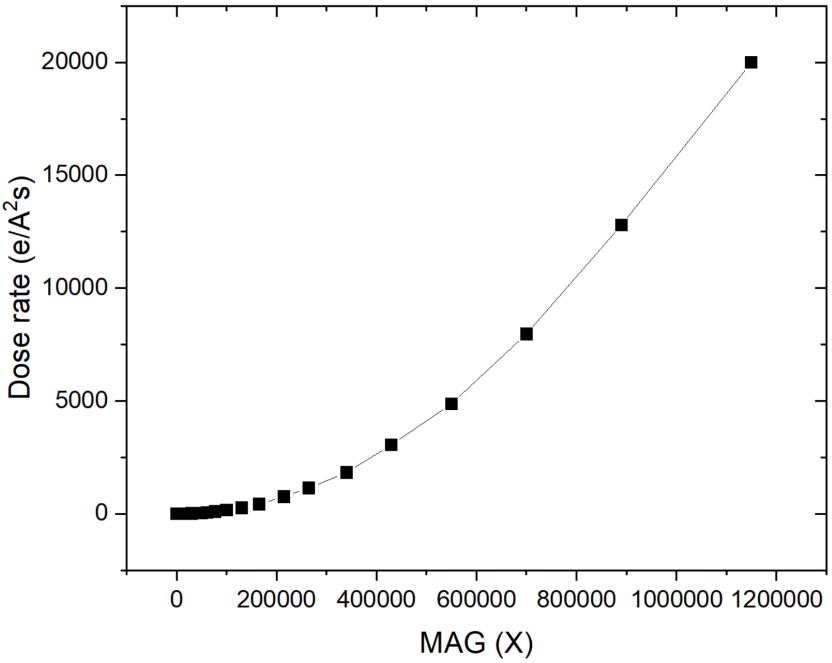

Figure 4.5 – Dependence of e-beam dose rate on the TEM magnification

large cubes since it is not possible to condensate so much the electron beam, unless the whole part of the cube is not be observed. So for larger cubes, the intensity of the electron beam can not reach a value as high as the one used in the case of small cubes.

From the results summarized in Fig4.6, it can been seen that larger particles are less likely to undergo phase transition than smaller particles. Indeed, phase transition occurs in a larger fraction of the volume of the smaller particles. Such a result agrees the trend reported in the literature [HAO 18][WU 04]. However, in our experiments we also found that some of the small particles do not undergo phase transition even under high electron doses, even when irradiated for a long time. Regarding this phenomenon, it is also necessary to take into account the effect of the different crystalline planes on phase change.

■ Effect of the electron dose on the nanocube facets

As shown in Fig4.7a, we chose a side of the particle with two crystal planes for observation. Five zones were selected as the areas to be observed. Zone 1 and zone 5 include (001) and (011) facets, whereas zones 2,3,4 only include (001) facets.

Fig4.7b shows the DP corresponding to each zone at different irradiation times. In Fig4.7b, the red arrow marks the diffraction spot indicating the appearance of the superlattice,

Cette thèse est accessible à l'adresse : https://theses.insa-lyon.fr/publication/2022ISAL0090/these.pdf
© [R. Zhang], [2022], INSA Lyon, tous droits réservés

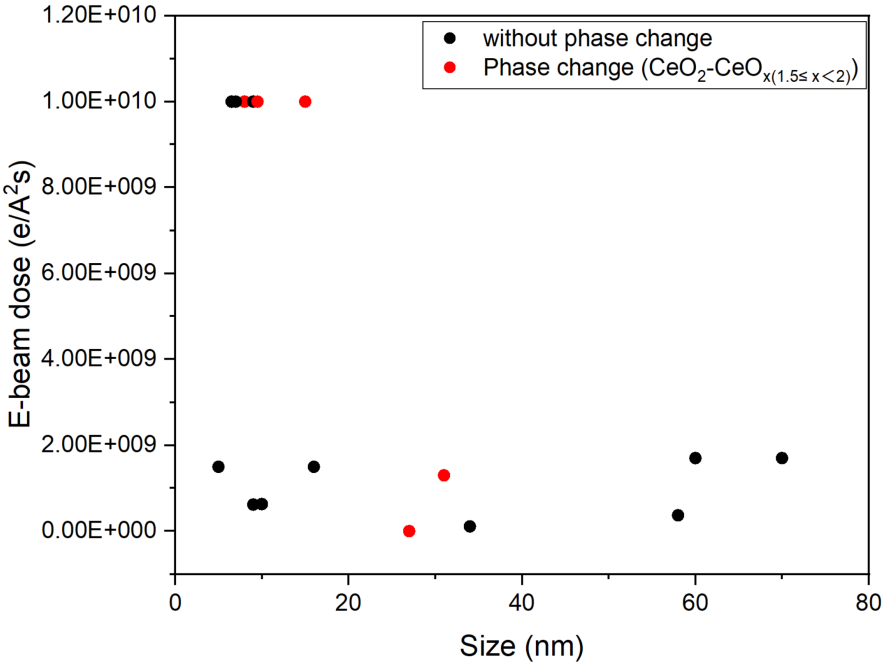

Figure 4.6 – CeO_2 particles of several sizes irradiated with different electron beam doses. The black dots represent CeO_2 that retains its structure (fluorite, Fm-3m space group) after irradiation. The red dots present a phase change from fluorite to bixbyite Ia-3.

which means that the fluorite structure transformed to the bixbyite structure. After the same dose and the same time of e-beam irradiation, the phase change successively appears in regions 2, 3, and 4. But regions 1 and 5 still maintain the original fluorite structure. These results show that the (001) plane is more easily reduced under the exposure of electron beam. The {100} planes tend to be reduced, which is the same as other experimental results [BUG 17] [GOR 14] [TUR 11].

This helps to explain why some small particles in our experiments are not easily reduced. Indeed in Fig4.3, we can see that, in small particles, the surface ratio of {100} planes is lower than in large particles. Due to the low ratio of {100} planes, it is thus not prone to reduction for small particles.

Cette thèse est accessible à l'adresse : https://theses.insa-lyon.fr/publication/2022ISAL0090/these.pdf
© [R. Zhang], [2022], INSA Lyon, tous droits réservés

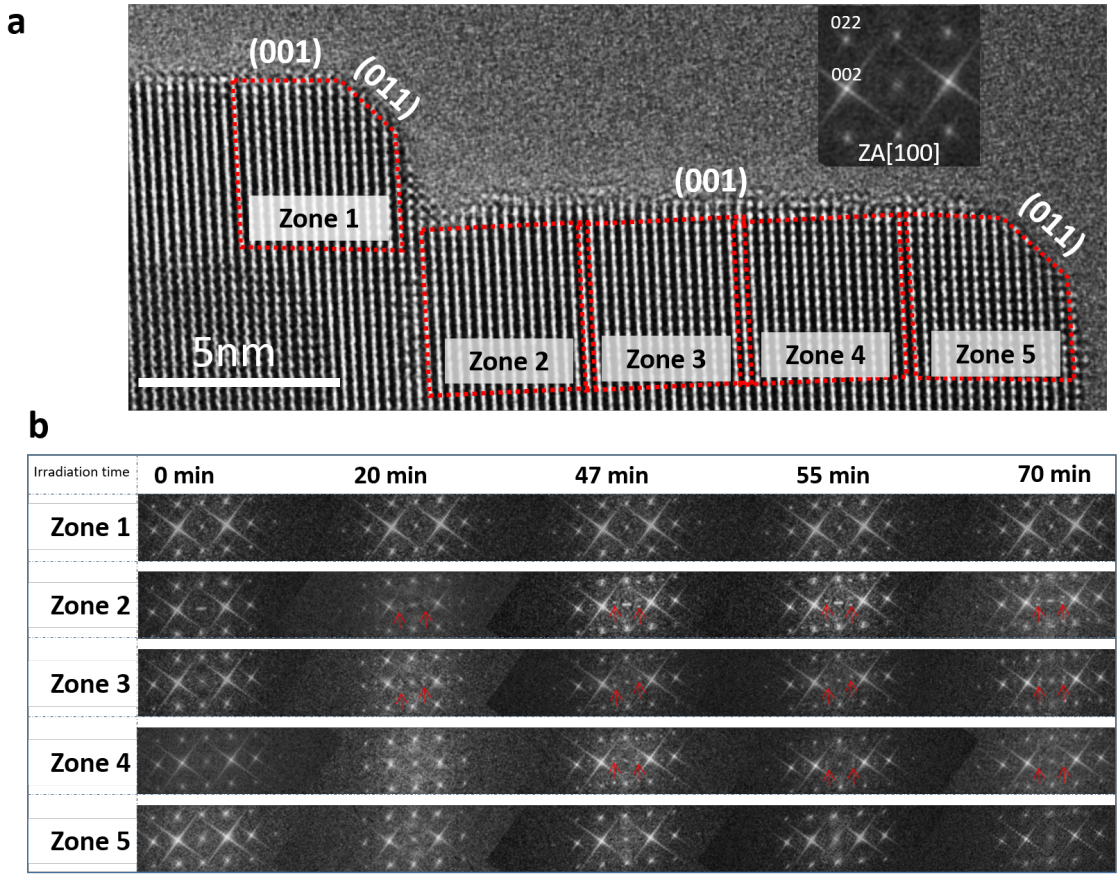

Figure 4.7 – a. Selection of five regions including (011) and (011) planes. Region 1 and region 5 include (001) and (011) facets, and the other regions contain only (001). b. Diffraction patterns corresponding to each region after the same time of e-beam irradiation. Region 1 and 5 maintain the original fluorite structure, while other regions undergo a phase change.

Cette thèse est accessible à l'adresse : https://theses.insa-lyon.fr/publication/2022ISAL0090/these.pdf
© [R. Zhang], [2022], INSA Lyon, tous droits réservés

■ Effect of the electron dose on the oxygen content

Electron Energy Loss Spectroscopy (EELS) can be used for chemical composition determination. Here we use EELS to determine the exact oxygen content x value during reduction of CeO_2.

Fig4.8 shows the evolution of x under different electron beam doses. From this graph we can estimate the value of x based on the electron beam dose. From the results, at low dose, the nanocubes are reduced from CeO_2 to $CeO_{1.74}$. At higher dose, they are reduced to Ce_2O_3, as x is found to be equal to 1.56.

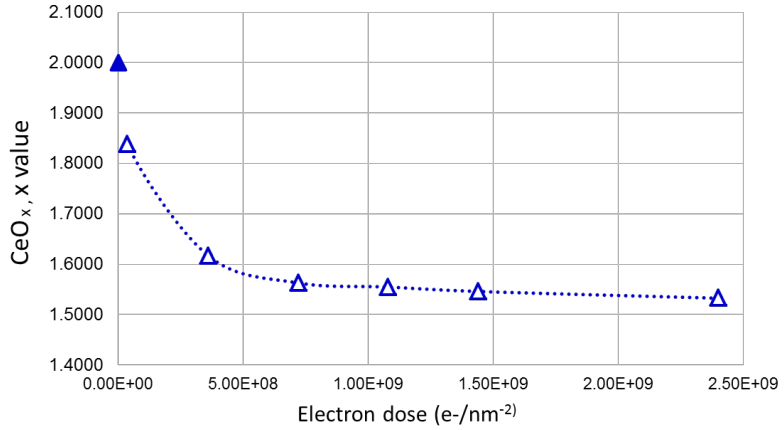

Figure 4.8 – Oxygen content x, measured by EELS, in a CeO_x nanocube, as a function of the electron dose. (EELS experiments conducted by Thierry Epicier)

To briefly summarise, the electron beam has reduction effects on the CeO_2. The electron beam will reduce particles from fluorite to Bixbyite structure. At the same time, we found that the {100} planes is more likely to be reduced by the electron beam than the {110} planes. The size of the particle also has an effect on the reduction. Experiments have found that smaller particles are more easily reduced. However, there are some small particles that maintain their original structure at low electron beams, and we speculate that this may be due to the high proportion of {110} planes in the small particles.

Cette thèse est accessible à l'adresse : https://theses.insa-lyon.fr/publication/2022ISAL0090/these.pdf
© [R. Zhang], [2022], INSA Lyon, tous droits réservés

4.2 Study of the CeO_2 slip systems

In this section, we focus on $CeOx$ nanocubes that remain in the fluorite structure. Even though the oxygen fraction x may be less than 2 due to the electron beam, such nanocubes are called "CeO_2" in the following, as a reference to the fluorite structure.

From Chapter 2.2.1, the more general consensus for fluorite is that <110>{100} is the primary slip system [LIU 64] [FRI 89] [CHE 89] [CHE 91] [DOM 91a] [DOM 91b] but because the compression direction is (001) in our experiments, this slip system cannot be activated. Only the other slip systems can be activated, but the ranks of the slip systems <110>{110} and <110>{111} are still not clear as there are not many experimental proofs [KEL 81] [POR 18]. We mainly use here two methods to determine the preferential slip system in CeO_2. In a first approach, the nanocube is tilted to obtain 3D information on dislocations remaining in the nanocube after unloading. In a second approach, we track dislocation configuration changes during compression.

3D information regarding dislocations

As described in Chapter 3.1.1, the sample holder may be tilted by ±20 degrees around an axis perpendicular to the substrate. The best condition we found is when a particle can be observed at -20 degrees or +20 degrees with a zone axis (ZA) very close to [110] or [100]. Indeed, this allows the cube to be tilted to the other ZA. When images are simultaneously obtained with both ZA [100] and [110], the actual direction and plane of the dislocation can be identified.

In order to avoid too many dislocation entanglements or a case where it is difficult to distinguish the dislocations from each other, we compressed a CeO_2 cube with a small strain. Fig 4.9 shows dark-field images of a CeO_2 cube (size: 60 nm) before and after compression, with the corresponding mechanical curve. In the dark-field images (g-vector indicated in the Figure), the deformation is close to 2.2. From the curve there is no obvious yield point, so the yield stress is defined by combination with the *in situ* video as the stress corresponding to the generation of dislocations. It is estimated around 6514 MPa. By comparing the images before and after compression, only one long, clear dislocation

Cette thèse est accessible à l'adresse : https://theses.insa-lyon.fr/publication/2022ISAL0090/these.pdf
© [R. Zhang], [2022], INSA Lyon, tous droits réservés

remains visible in the sample after unloading.

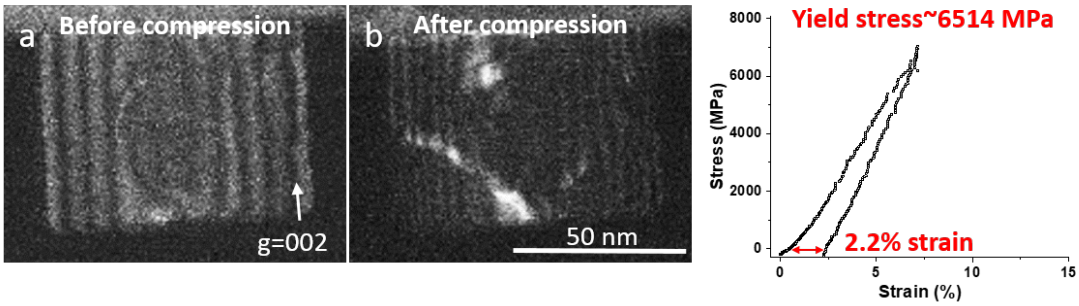

Figure 4.9 – Dark-field images of a CeO_2 cube before and after compression. ZA=[110] and g-vector [002]. The stress-strain curve is on the right with corresponding strain and yield stress.

Fig4.10 shows DF images (g=002) of the same nanocube, acquired with different orientations after unloading. The initial ZA is [110]. The tilt angle was gradually increased with tilt steps of 10° until 45° (10, 20, 30 and 45°). With a tilt angle of 35°, the DP shows an orientation along the ZA [100]. In terms of crystal structure, the fluorite crystal needs to be tilted by 45° to change from ZA [110] to ZA [100]. But in this experiment, the value of the tilt angle is read from the TEM, and there might be a slight error between the value read and the real value. The angles indicated in the Fig.4.10 are read from TEM but we mainly determined the crystal direction using the DP.

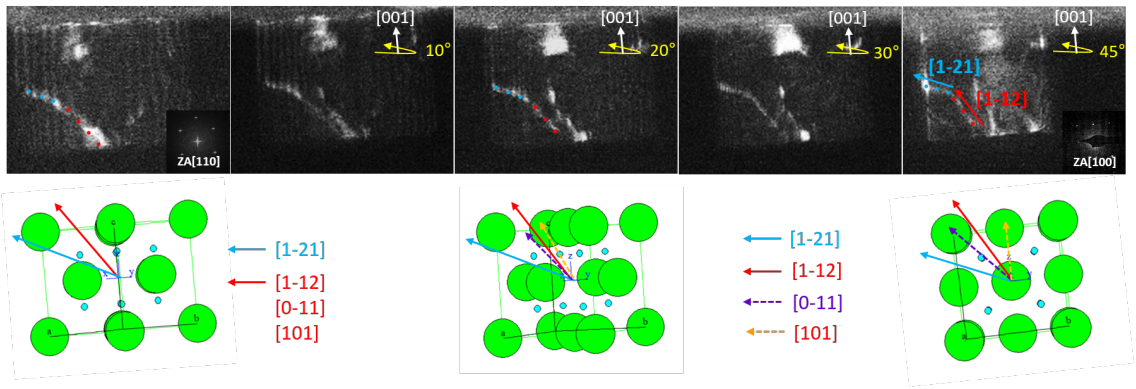

Figure 4.10 – Dark-field images acquired when tilting the cube around the direction [001], at 0°, 10°, 2°, 30° and 45° degree from the zone axis [110]. Below the images are the corresponding crystal structures. The direction of the dislocation lines are marked.

Cette thèse est accessible à l'adresse : https://theses.insa-lyon.fr/publication/2022ISAL0090/these.pdf
© [R. Zhang], [2022], INSA Lyon, tous droits réservés

With the ZA [110], two dislocations are observed. The schematic representations below the DF images give the possible dislocation vectors, among all the possible slip systems. In the direction of the blue arrow, there is only one possibility: [1-21] on the (-111) plane. However, the red arrow can correspond to three vectors: [1-12] or [0-11] or [101] on the (-111) plane. After the cube is tilted by 15 degrees, four vectors are mapped out with different colours. With this tilting angle, the directions of both dislocations can be identified as [1-21] and [1-12]. Yet, because with this tilting angle, the four possible directions remain close to each other, the nanocube was tilted to a larger angle, up to the ZA [100]. When the cube is tilted to the ZA [100], it becomes possible to confirm that both dislocations directions are [1-21] and [1-12].

Through this operation, a few dislocations are introduced and remain in the nanocube after unloading. Two points should be noted: (1) the DF images obtained with the g-vector g=002 makes the other dislocations invisible. (2) As show in Fig**??**, When the force direction is [001], the Schmid factor of the slip system <110>{100} is zero, indicating that it cannot be activated. <110>{100} is regarded the principal slip system in fluorite, however <110>{110} and <110>{111} are not widely investigated, thus we concentrate on priority of <110>{110} and <110>{111} in our study.

We identified two obvious dislocations and both of them are edge dislocations on (-111) plane. A series of DF images are used to construct configuration of dislocations to determine which slip system the dislocations are predominantly on at low strain and to compare the priority of both slip systems <110>{110} and <110>{111}. From the results above, the dislocations occurs mainly on the {111} plane. Also, to further identify the main slip systems, an other approach was taken, which is described in the next section.

dislocation configuration changes during compression

It is also possible to identify the dislocation vectors and slip planes by observing the configuration changes during deformation. Fig 4.11 shows the loading curve and bright field images before and after compression. The data were extracted from the compression test on a CeO_2 nanocube of size 62 nm. In Fig 4.11(a), the blue and red lines are the displacement-time and force-time curves, respectively. When both curves are combined, it is obvious that the loading rate is constant (0.1 nm/s from DIC), and the time at which the

Cette thèse est accessible à l'adresse : https://theses.insa-lyon.fr/publication/2022ISAL0090/these.pdf
© [R. Zhang], [2022], INSA Lyon, tous droits réservés

indenter begins to retract can also be precisely determined. The mechanical curve before the tip starts to retract reflects the mechanical behavior of the sample, so it is important to confirm the position where the indenter starts to retract to analyze the compression response of the sample.

In Fig 4.11(b), it seems there are few defects already existing inside the cube. On the contrary, from Figure (c), it is clear that the cube is defect-free after compression. This means that the pre-existing defects and the dislocations created during compression were not entangled and could slip to the nanocube surface upon unloading.

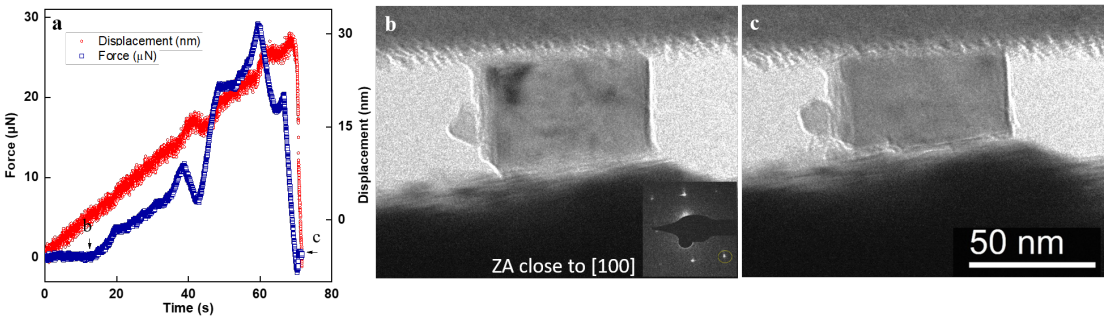

Figure 4.11 – Compression test of CeO_2 along [001]. Cube size: 62 nm (a) Force-time (blue line) and displacement-time (red line) curves. b and c indicate the beginning and the end of the compression test. (b) bright field image of the cube before compression (corresponding to position b on the curve) with the corresponding diffraction pattern showing a zone axis close to [100]. (c) bright field image of the cube after compression (position c on the curve).

Fig4.12 shows the stress-strain curves before and after DIC processing. The original displacement is bigger than the displacement of the actual indenter moving forward when combined with the compression video, resulting in a large strain. The strain should change correctly following DIC processing, but not perfectly. The curve (Fig4.12 right) shows that a small part of the strain value retracts during the continuous compression, but the data after DIC processing is more reliable than the original curve.

In order to analyze the changes in the cube during the compression process, we combine the *in situ* video with the stress-strain curve to present the dislocation changes at each

Cette thèse est accessible à l'adresse : https://theses.insa-lyon.fr/publication/2022ISAL0090/these.pdf
© [R. Zhang], [2022], INSA Lyon, tous droits réservés

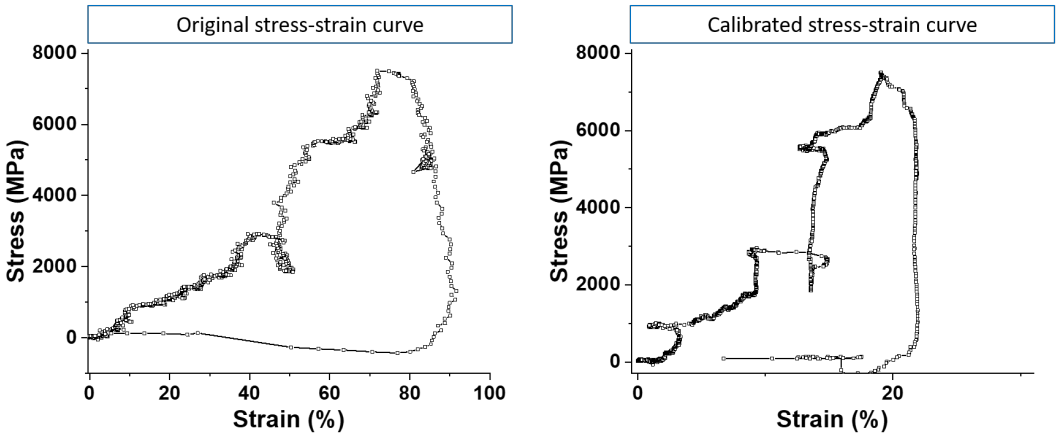

Figure 4.12 – Stress-strain curve of the cube before and after DIC processing.

stage. According to the mechanical curve (stress-strain curve in Fig4.13), there are four main stages and each stage indicate one stress drop.

Comparing the bright field images of these four stages demonstrates that the behaviour of the nanocube is similar for all the stress drops. The top layer images (I-IV) present the nanocube just before the stress drops. The contrast inside the cube reveals the presence of defects (mainly dislocations) and it is clear that the dislocation density is high before each stress drop. the bottom layer images (I'-IV') present the cube after each stage of stress drop. By comparing the cube just before and after a stress drop (I-I' for instance), the differences in the contrast reveal that the nanocube contains less dislocations and it is quite "clean". The stress decrease is caused by the escape of defects, which annihilate at the sample surface. Plastic deformation is the result of a high number of dislocations moving to the surface. Due to the small size of the sample, no further dislocations are created, and the dislocation distribution in the particles diminishes progressively as the dislocations approach the surface before interacting to form junctions. Finally, the dislocation density tends to zero. This phenomena is related to the "dislocation starvation" process for mechanical behavior of microscopic scale metal samples. The earliest experimental evidence for this theory was found in *in situ* TEM experiments, in which a Ni single crystal pillar with a high initial dislocation density escaped from the surface of the pillar during compression, leaving an almost perfect dislocation-free pillar. This phenomenon is also known as "mechanical annealing".

Cette thèse est accessible à l'adresse : https://theses.insa-lyon.fr/publication/2022ISAL0090/these.pdf
© [R. Zhang], [2022], INSA Lyon, tous droits réservés

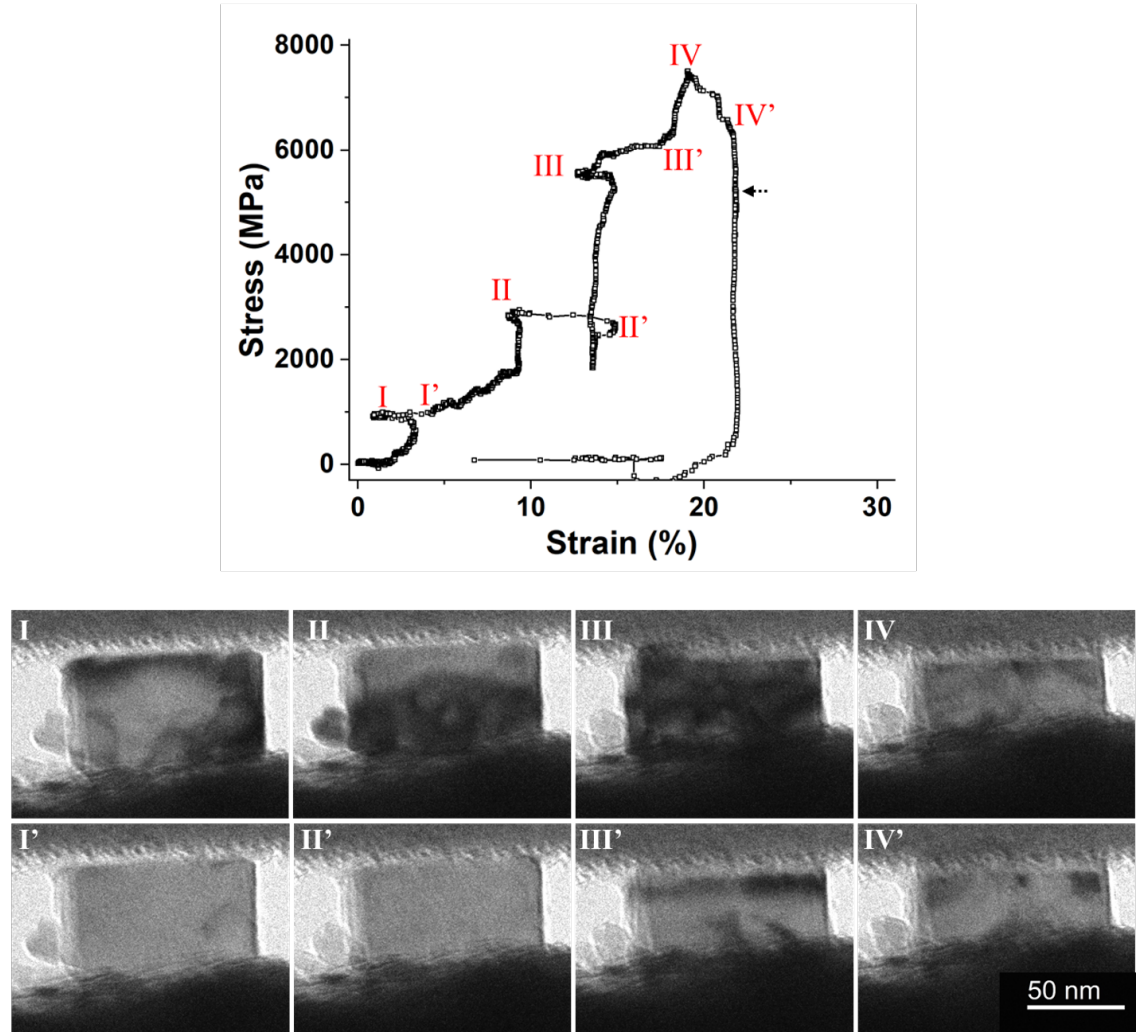

Figure 4.13 – Stress-strain curve derived from the test presented in Fig 4.11. There are four stress drop periods marked by a roman number and a roman number' (like for instance I and I'). The snapshots corresponding to the points marked by roman numbers are also given.

In the following, the dislocations generated at each stage are analyzed. To identify the dislocation generated, Fig 4.14 shows all the screw and edge dislocations for which the Schmid factor is not nil with the compression direction [001]. For each slip system, a scheme represents the slip plane and Burgers vector according to the projection direction of the nanocube compressed in Fig 4.14.

Fig 4.15, 4.16, 4.17, 4.18 show snapshots revealing dislocation line changes in the CeO_2

Cette thèse est accessible à l'adresse : https://theses.insa-lyon.fr/publication/2022ISAL0090/these.pdf
© [R. Zhang], [2022], INSA Lyon, tous droits réservés

Slip systems "S" is Schmid factor	**Schematic presents correspond slip system** (green area is slip plane, red line is screw dislocation, blue line is edge dislocation)	½ [101](-111) **S**=0.41	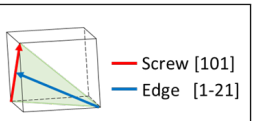
½ [0-11](111) **S**=0.41	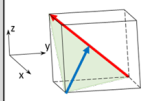	½ [011](1-11) **S**=0.41	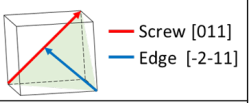
½ [-101](111) **S**=0.41	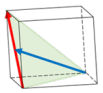	½ [-101](1-11) **S**=0.41	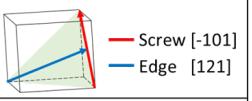
½ [101](11-1) **S**=0.41	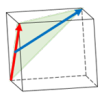	½ [0-11](011) **S**=0.5	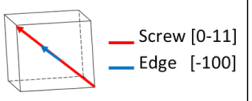
½ [011](11-1) **S**=0.41	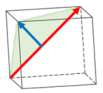	½ [101](10-1) **S**=0.5	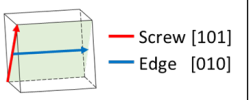
½ [0-11](-111) **S**=0.41	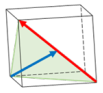	½ [011](01-1) **S**=0.5	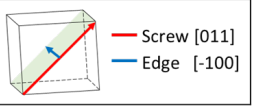

Figure 4.14 – List of the slip systems that can be activated in CeO_2, with the corresponding values of the Schmid factor. For each slip system, the direction of the dislocation lines for screw and edge dislocations are indicated.

nanocube tested in Figure 4.13. The TEM images correspond to the transitions from the original state to I, from I' to II, from II' to III and from III' to IV, respectively. Based on the Table (4.14), the Burgers vector and type of dislocation can be determined. In the TEM images, the dislocations are depicted with dotted lines and the corresponding schematic diagrams are given below the TEM images.

Cette thèse est accessible à l'adresse : https://theses.insa-lyon.fr/publication/2022ISAL0090/these.pdf
© [R. Zhang], [2022], INSA Lyon, tous droits réservés

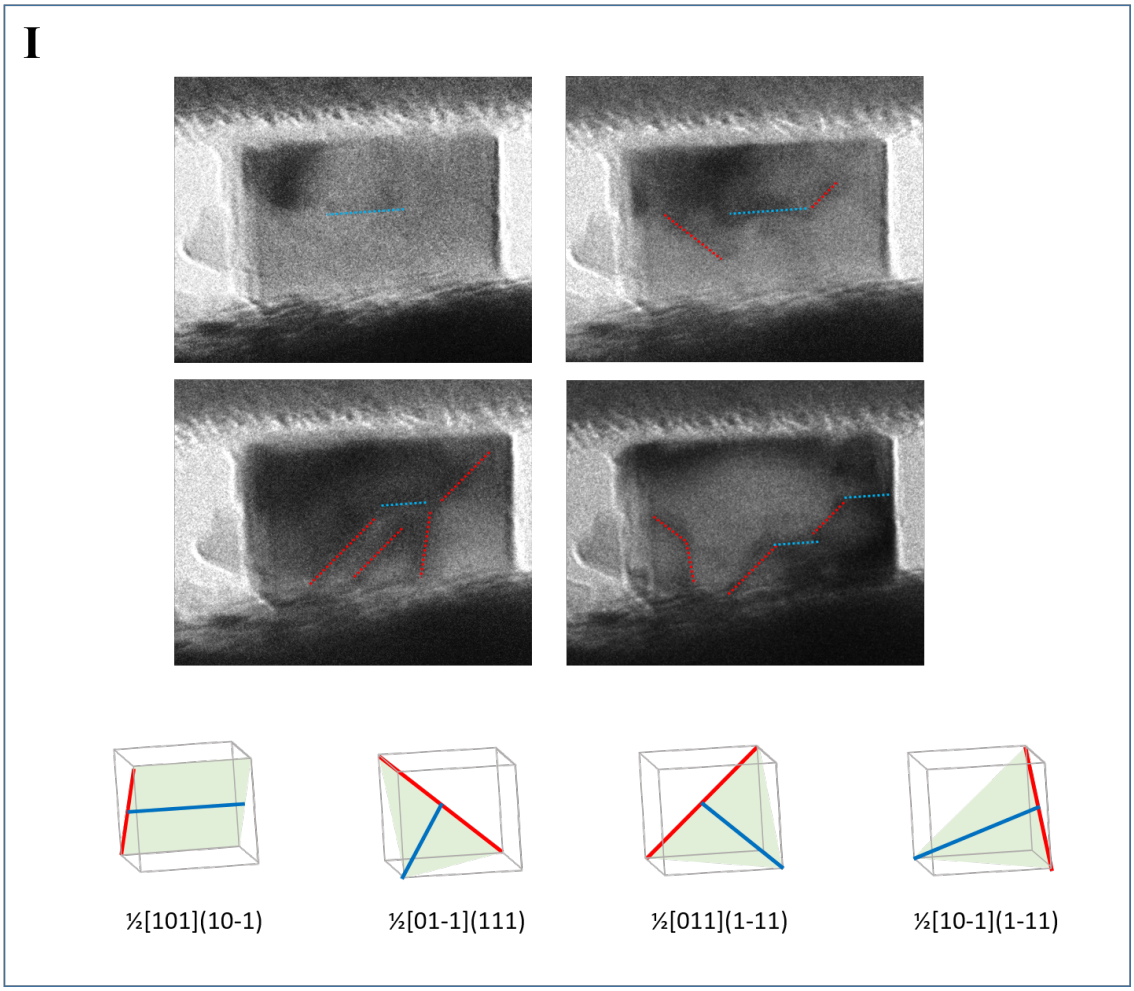

Figure 4.15 – Snapshots of the CeO_2 nanocube tested in Figure 4.13, from the original state to stage I. The dislocations are traced out with dotted lines and the corresponding schematic diagrams are depicted below the snapshots.

Cette thèse est accessible à l'adresse : https://theses.insa-lyon.fr/publication/2022ISAL0090/these.pdf
© [R. Zhang], [2022], INSA Lyon, tous droits réservés

In the initial state (Fig 4.15), the existence of some dislocations can be confirmed. There is a [101](10-1) edge dislocation at the onset of the compression test. With increasing compression, several screw dislocations are generated in the (111) and (1-11) planes.

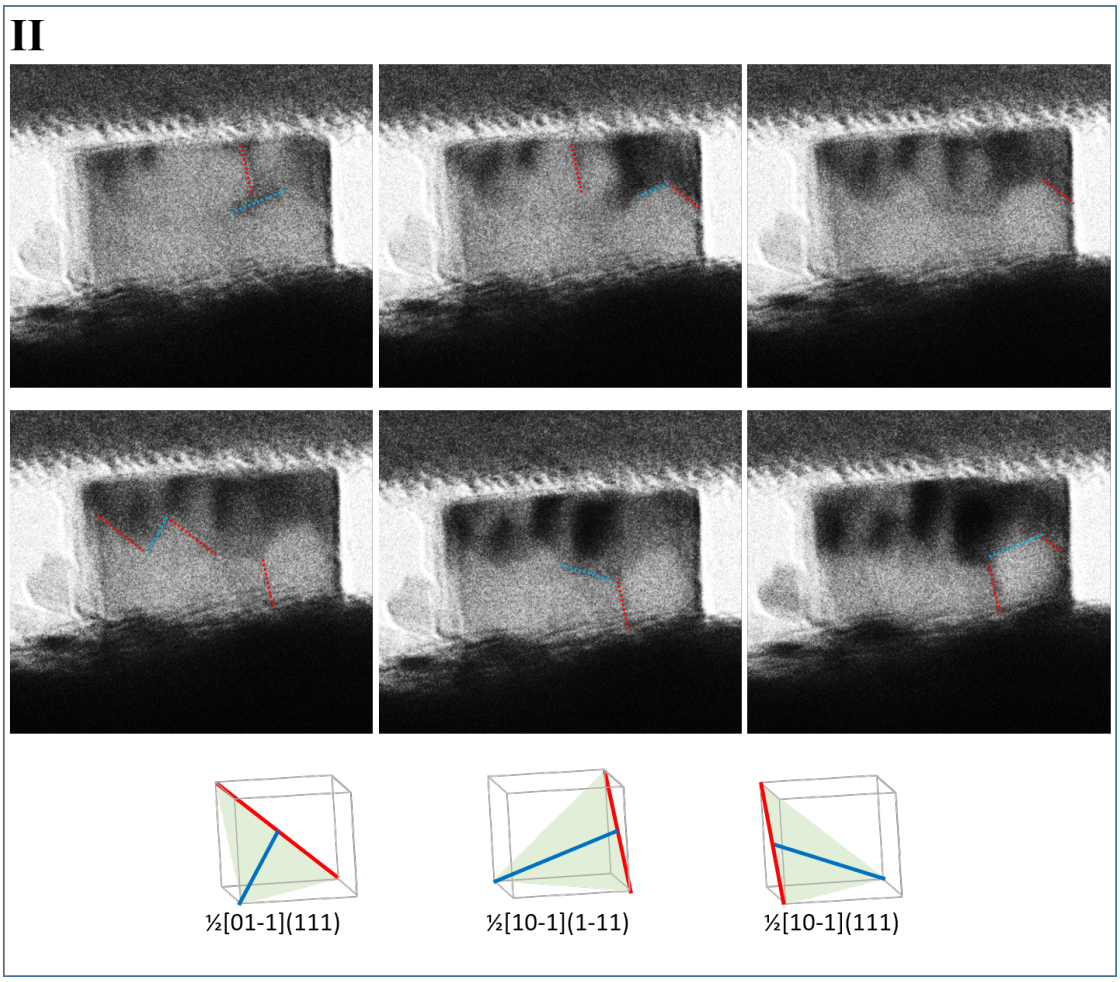

Figure 4.16 – Snapshots of the CeO_2 nanocube tested in Figure 4.13, from the I' to stage II. The dislocations are traced out with dotted lines and the corresponding schematic diagrams are depicted below the snapshots.

Cette thèse est accessible à l'adresse : https://theses.insa-lyon.fr/publication/2022ISAL0090/these.pdf
© [R. Zhang], [2022], INSA Lyon, tous droits réservés

In the second stage (Fig 4.16, new dislocations are generated after the "mechanical annealing." All dislocations are in the planes (111) and (1-11).

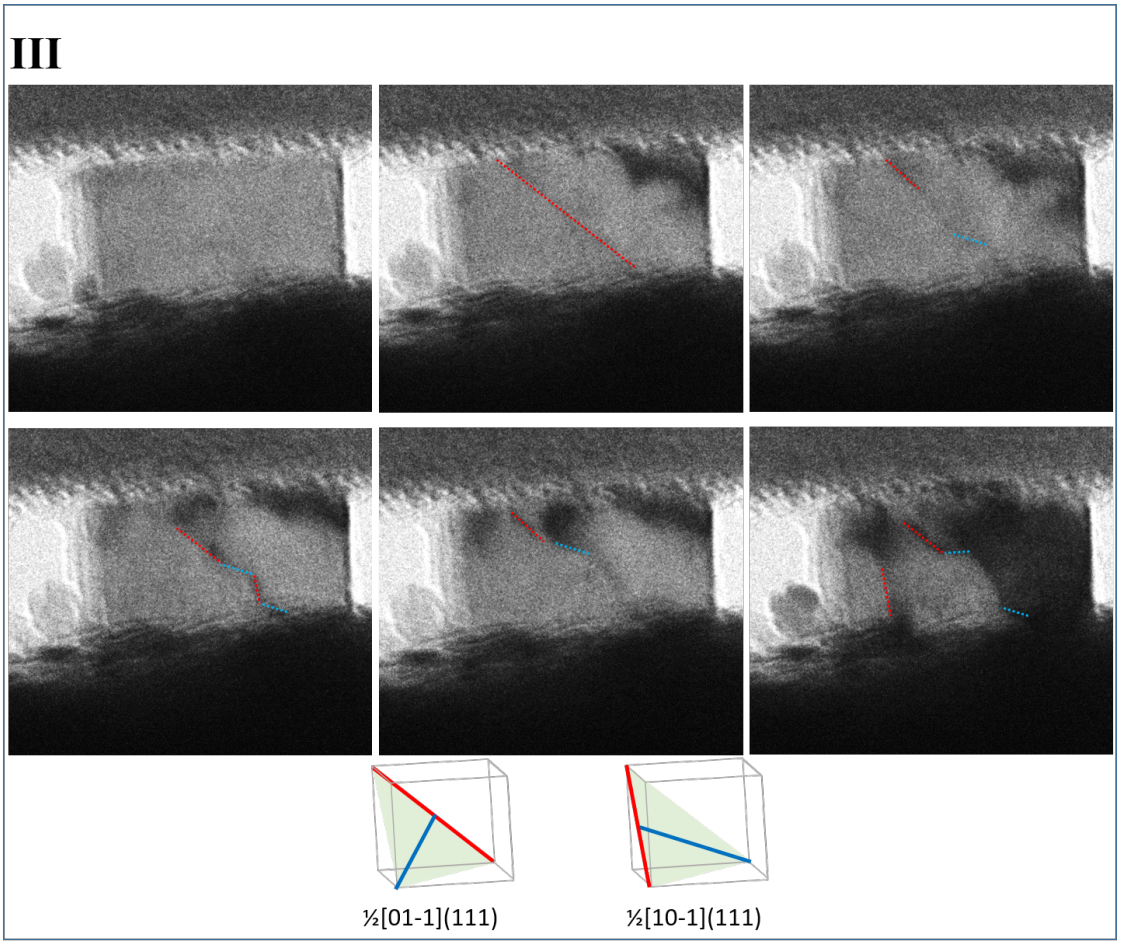

Figure 4.17 – Snapshots of the CeO_2 nanocube tested in Figure 4.13, from the II' to stage III. The dislocations are traced out with dotted lines and the corresponding schematic diagrams are depicted below the snapshots.

Cette thèse est accessible à l'adresse : https://theses.insa-lyon.fr/publication/2022ISAL0090/these.pdf
© [R. Zhang], [2022], INSA Lyon, tous droits réservés

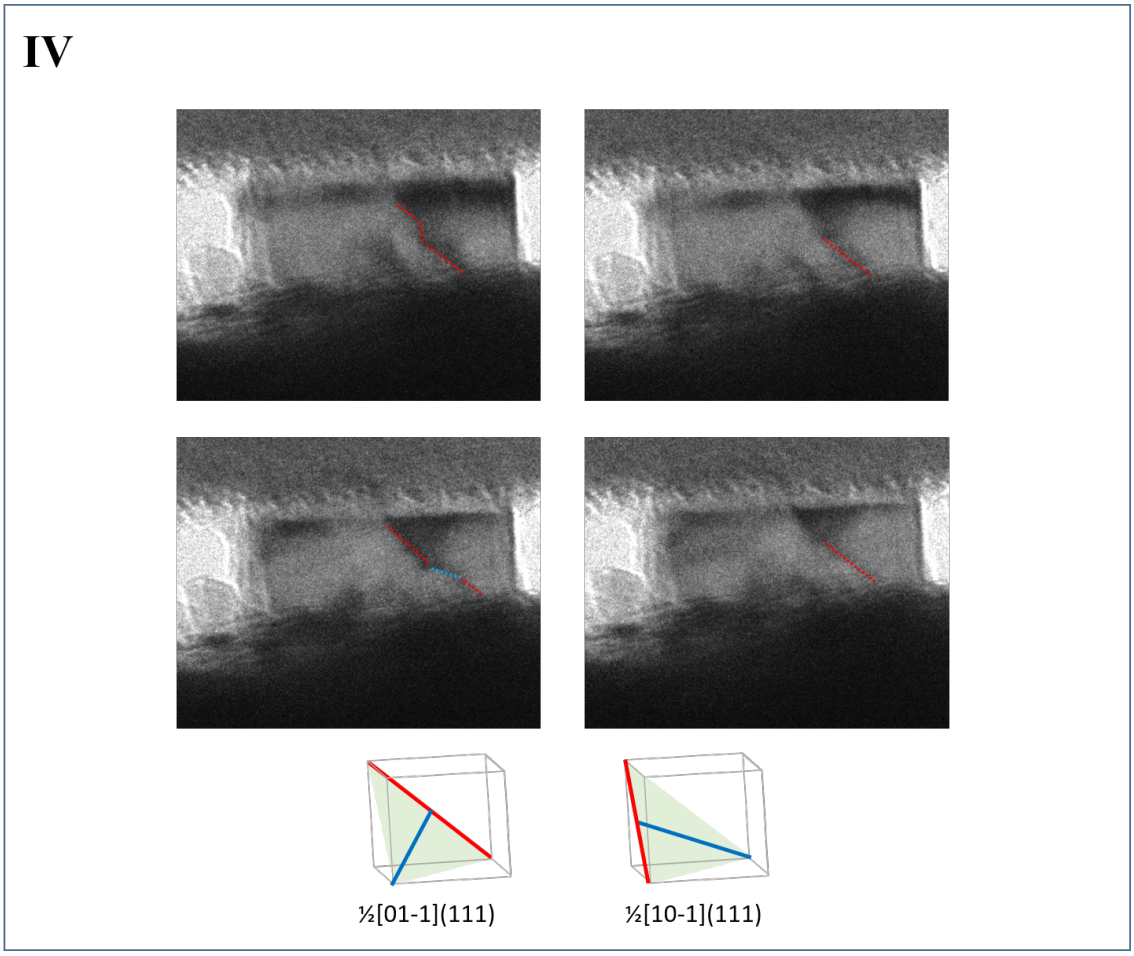

Figure 4.18 – Snapshots of the CeO_2 nanocube tested in Figure 4.13, from the III' to stage IV. The dislocations are traced out with dotted lines and the corresponding schematic diagrams are depicted below the snapshots.

Cette thèse est accessible à l'adresse : https://theses.insa-lyon.fr/publication/2022ISAL0090/these.pdf
© [R. Zhang], [2022], INSA Lyon, tous droits réservés

In the subsequent third and fourth stages (Fig 4.17 and 4.18, respectively), the dislocations are only in the (111) plane and are mainly screw dislocations.

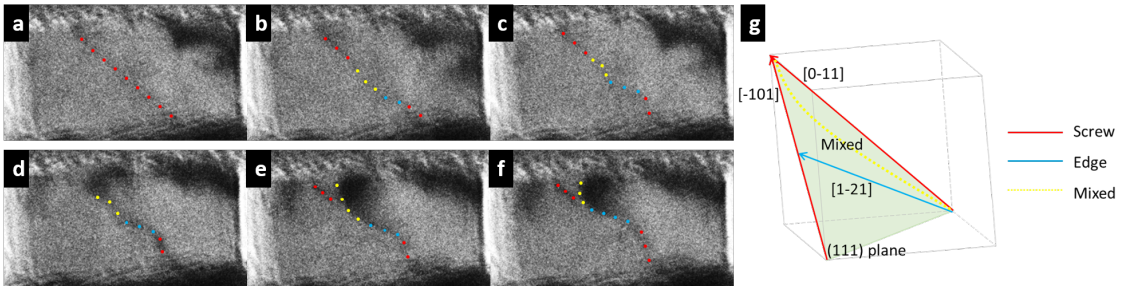

Figure 4.19 – (a-f) Video snapshots extracted of the CeO_2 nanocube tested in Fig 4.13, during the stress drop between stages III and III'. (g) Schematic representation of corresponding dislocation lines. The main dislocation slip plane is (111).

Fig 4.19 presents the change in dislocation configuration observed during the third stress drop, from stage III to stage III'. A screw dislocation is illustrated with a red dashed line (Fig 4.19a). This dislocation modifies its configuration with increasing deformation, with the appearance of mixed and edge parts. However, all parts of this dislocation are still in the (111) plane. Fig 4.19g is a schematic graph which indicates, with the same view direction, the screw, edge, and mixed dislocation on the (111) plane.

In brief, the newly generated dislocations from the cube defect-free state are mostly on the (111) plane. Although edge and mixed characters have been identified, the dislocations mostly have screw characteristics.

4.3 Size effect in CeO_2

After identifying the main slip systems by TEM observations, we found in CeO_2 cube (size:62 nm) that the stress drops correspond to dislocation escape to the free surfaces. This means that dislocation starvation can also happen in CeO_2 cubes. So in this section, we focus on the size influence on the yield stress. Moreover, with the TEM investigation, the deformation mechanism will be further explored.

As discussed above (chapter 4.1.2) CeO_2 is reduced under electron beam, so the size effect on the yield stress was studied by compressing 14 nanocubes under low electron dose

Cette thèse est accessible à l'adresse : https://theses.insa-lyon.fr/publication/2022ISAL0090/these.pdf
© [R. Zhang], [2022], INSA Lyon, tous droits réservés

rate. An explanation of the deformation mechanism is attempted through the analysis of the corresponding *in situ* videos.

Cette thèse est accessible à l'adresse : https://theses.insa-lyon.fr/publication/2022ISAL0090/these.pdf
© [R. Zhang], [2022], INSA Lyon, tous droits réservés

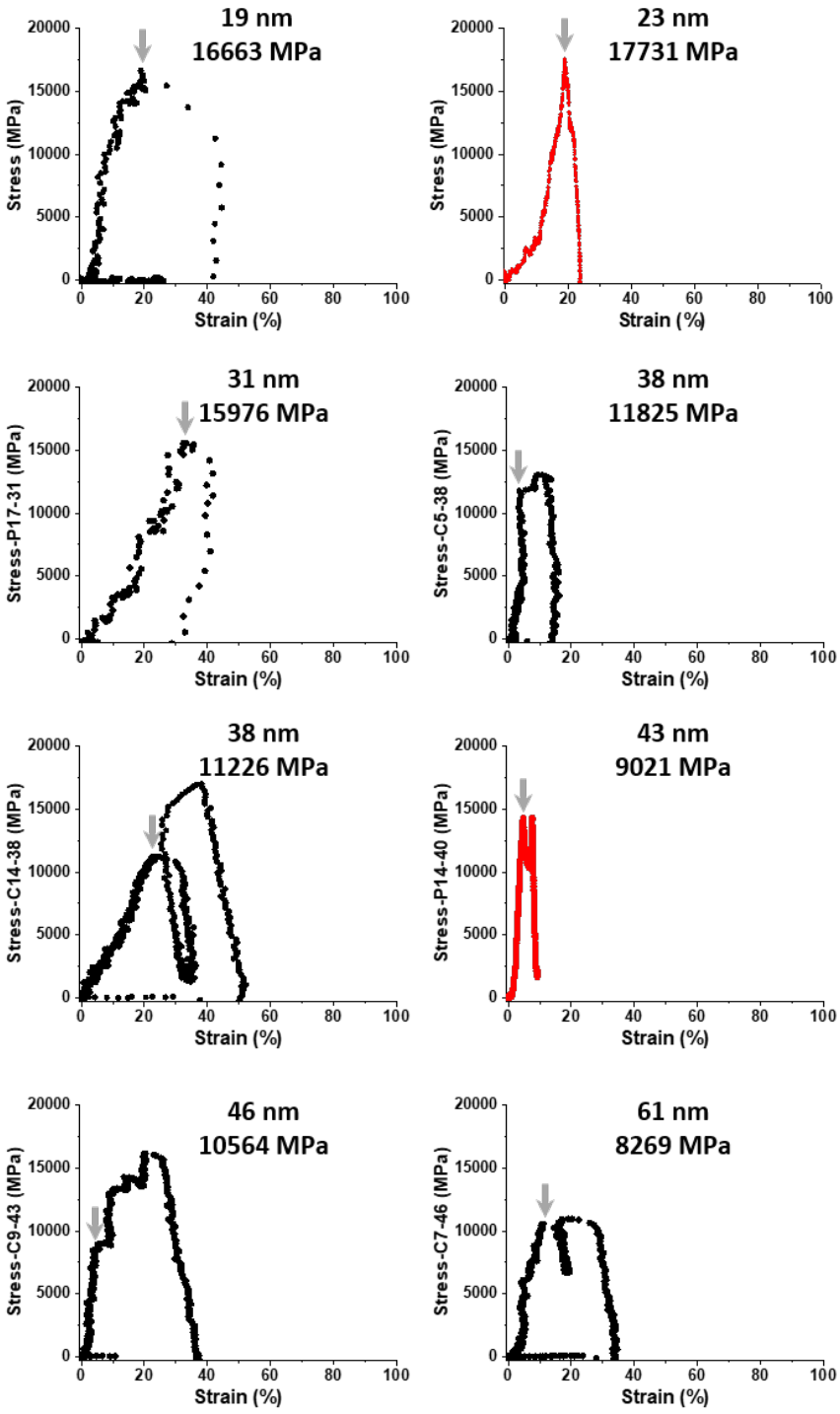

Figure 4.20 – Stress-strain curves of CeO_2 nanocubes of different sizes. All compression directions are [001]. The grey arrows indicate the yield points. The curves in red were obtained after measurement of the real displacement by DIC. DIC could not be successfully performed on the other ones, therefore they are left in black.

Cette thèse est accessible à l'adresse : https://theses.insa-lyon.fr/publication/2022ISAL0090/these.pdf
© [R. Zhang], [2022], INSA Lyon, tous droits réservés

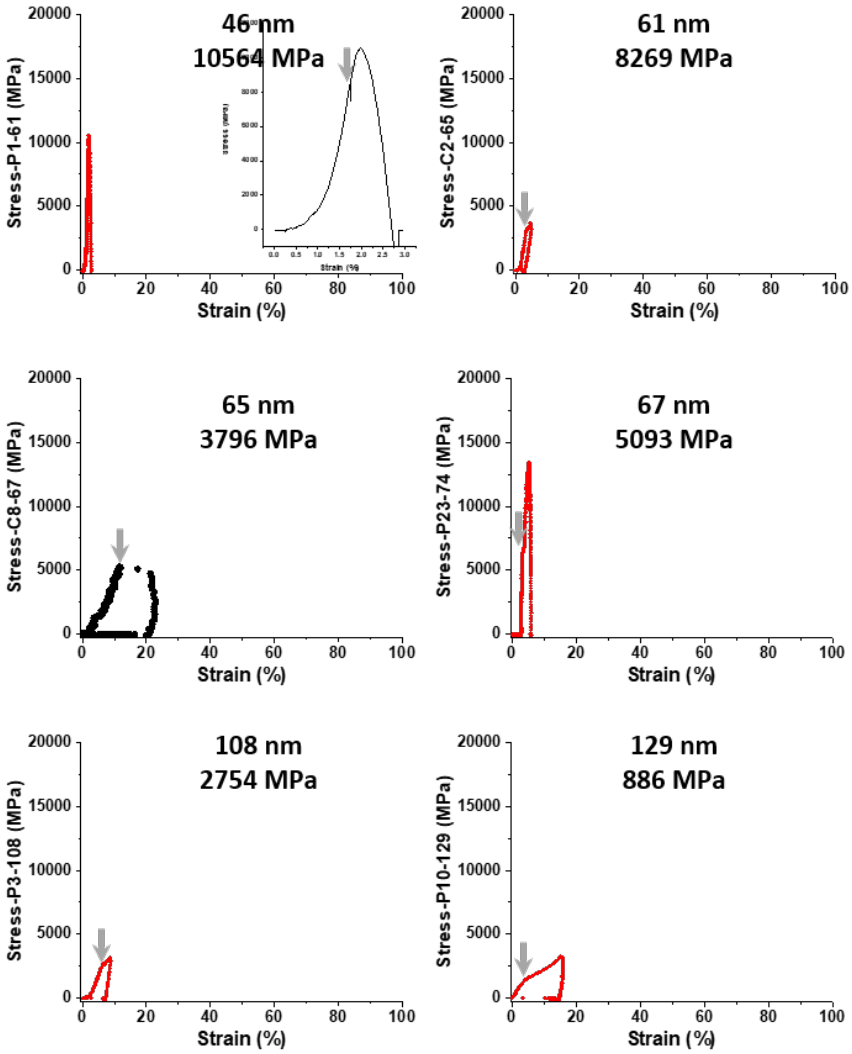

Figure 4.21 – Stress-strain curves of CeO_2 nanocubes of different sizes. All compression directions are [001]. The grey arrows indicate the yield points. The curves in red were obtained after measurement of the real displacement by DIC. DIC could not be successfully performed on the other ones, therefore they are left in black.

Cette thèse est accessible à l'adresse : https://theses.insa-lyon.fr/publication/2022ISAL0090/these.pdf
© [R. Zhang], [2022], INSA Lyon, tous droits réservés

Fig4.20 and Fig4.21 summarize the stress-strain curves for the 14 CeO_2 nanocubes. The grey arrows mark the yield points, for each cube size. It should be noted that some of the stress-strain curves were not processed by DIC for the following reasons: for small cubes that need to be observed at high magnifications. As the electron dose rate increases when increasing the magnification, the electron beam need to be de-condensed to ensure that the cubes will not be reduced during compression. This operation causes a decrease of the brightness and contrast, making the *in situ* video of poor quality and thus the DIC data unreliable. In Fig4.20 and Fig4.21, the curves without DIC processing are drawn in black, and those with DIC processing are drawn in red. When comparing the stress-strain curves before and after DIC (Chapter 3.3), it is clear that DIC mainly affects the measurement of the strain, but not that of the stress. Hence, our values of the stress can be taken with or without DIC processing.

To better show the relationship between size and yield stress, Fig4.22 shows the dependence of yield stress on the cube size. The label beside each dot gives the strain corresponding to the yield stress. The red values correspond to the strains obtained after DIC processing.

From the figure, the yield stress increases as the size decreases. In order to evaluate more previsely the size effect, normalized values are computed: ratio between the yield stress and the Young's modulus, and ratio between the nanocube size and the lattice parameter. A new graph is then obtained, see Fig4.23. The fitting work is carried out by Prof. David DUNSTAN, from the Queen Mary University in London.

In Fig4.23, the Y-axis is the elastic strain, which corresponds to the yield stress divided by the Young's modulus ($Y = 360$ GPa for bulk CeO_2, value obtained by simulation by G. Laurens and T. Albaret at ILM). The X-axis are the normalized size h, which corresponds to the nanocube size divided bu the lattice parameter ($a_0 = 0.54$ nm for CeO_2). The blue points come from the *in situ* experiments while the orange points come from simulations. Several curves are also drawn on this graph. The blue curve is an empirical curve computed for GaInAs (0.8nm/h). The orange curve is the theoretical curve for Frank-Read dislocation sources. In this model, the elastic strain varies as $5b/h$. In our case, as the Burgers vectors were found to be 1/2 <110>, $b = \frac{1}{2}\frac{0.54}{\sqrt{2}}$ nm. The green curve is the best

Cette thèse est accessible à l'adresse : https://theses.insa-lyon.fr/publication/2022ISAL0090/these.pdf
© [R. Zhang], [2022], INSA Lyon, tous droits réservés

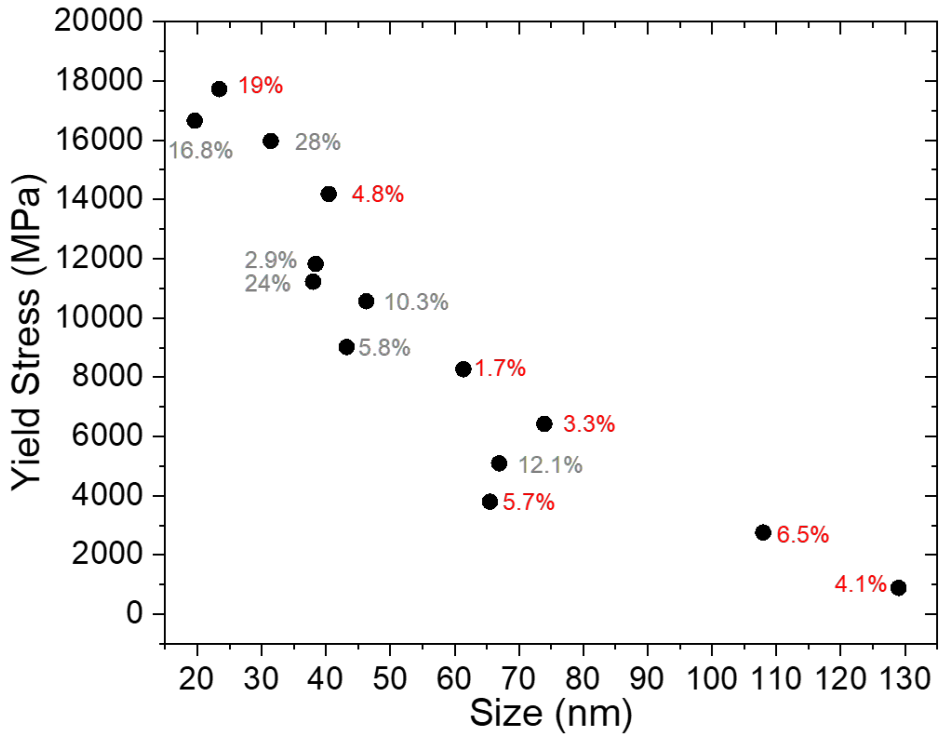

Figure 4.22 – Dependence of the yield stress on the nanocube size. Labeled beside each dot is the strain corresponding to the yield stress. Black is from the original data and red is from the DIC data.

Maximum Likelihood fit $a + h^{-c}$ to the data, obtained with $c = 0.97 \pm 0.15$, which is what is expected from the literature [DUN 17][DUN 91][DUN 12][ISS 21]. This means that the size effect can be explained by geometrical constraints in nanocubes where plasticity is due to dislocation multiplication.
It is interesting to notice that the elastic strain of the small cubes seem to be generally over the best fit curve. A similar behaviour was clearly evidenced in MgO nanocubes [ISS 21] and was attributed to a dislocation nucleation-starvation mechanism.

As we introduced in Chapter 1, two main model have been widely accepted to explain the size effect in submicron crystals. The first model corresponds to dislocation starvation[SHA 08]. The dislocation starvation mechanism mostly occurs in submicron

Cette thèse est accessible à l'adresse : https://theses.insa-lyon.fr/publication/2022ISAL0090/these.pdf
© [R. Zhang], [2022], INSA Lyon, tous droits réservés

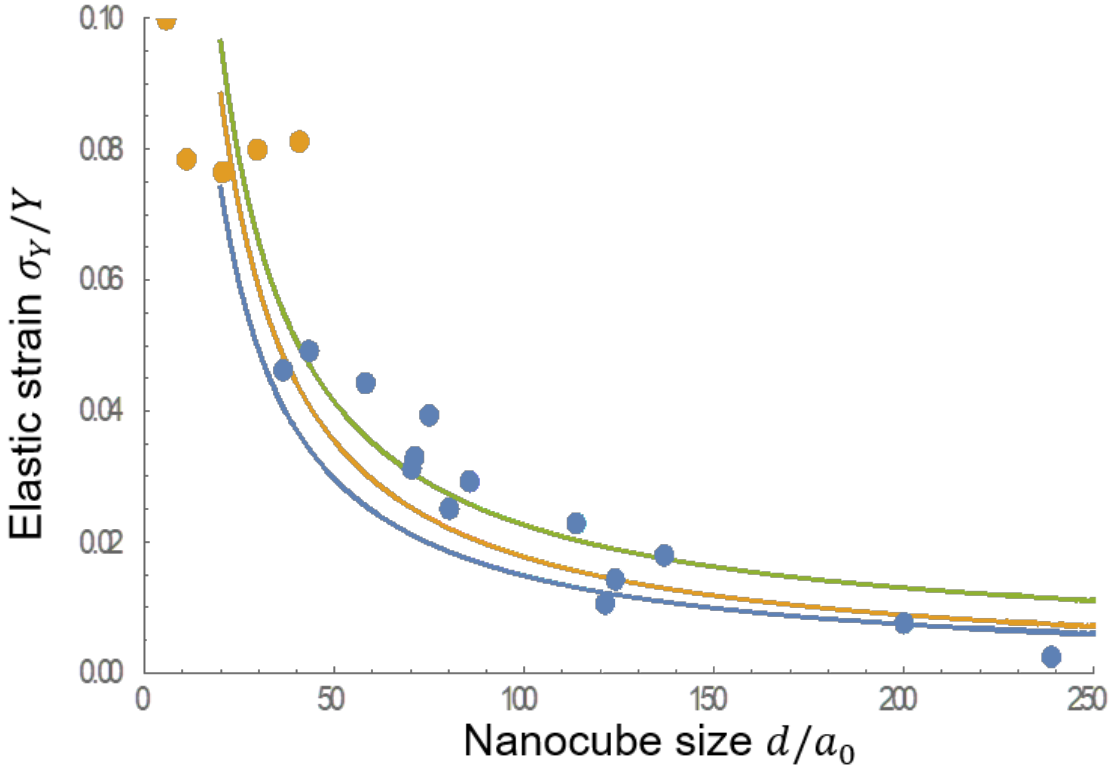

Figure 4.23 – Dependence of the elastic strain (yield stress divided by the Young's modulus at bulk, Y = 360 GPa) and the normalized size (nanocube size d divided by the lattice parameter $a_0 = 0.54$ nm). The blue dots come from the experiment, and the orange dots come from simulation results obtained by G. Laurens and T. Albaret at ILM. The blue curve is an empirical curve computed for GaInAs (0.8nm/h) and the green curve is the theoretical curve for Frank-Read dislocation sources (5b/h, with $b = \frac{1}{2}\frac{0.54}{\sqrt{2}}$ nm in our case). The orange curve is the result of the fit with the function a+bx^c, with $c = 0.97 \pm 0.15$. Work performed by Prof. David DUNSTAN from the Queen Mary University in London.

specimens with small sizes and low dislocation densities. At this point, as plastic deformation proceeds, dislocations gradually slip out of the specimen and surface nucleation plays the major role. The second model involves single-arm dislocation sources [OH 09]. In this case, due to the truncation effect of the surface, the Frank-Read dislocation sources with two pinned points, which is common in macroscopic bulk materials, become single-arm dislocation sources with only one pinned point. This mechanism occurs for larger sizes. Indeed, as the specimen size increases, it is more difficult to have nanocubes with-

Cette thèse est accessible à l'adresse : https://theses.insa-lyon.fr/publication/2022ISAL0090/these.pdf
© [R. Zhang], [2022], INSA Lyon, tous droits réservés

out any defect in the initial state. Therefore these defects can play the role of dislocation sources, and the single-arm source starts to become the dominant mechanism of plastic deformation. When the deformation is large enough, a large number of dislocations are generated and they interact with each other to form a complex and robust dislocation network that remains after unloading.

Both mechanisms were evidenced during compression tests in TEM on MgO nanocubes with different sizes[ISS 21].

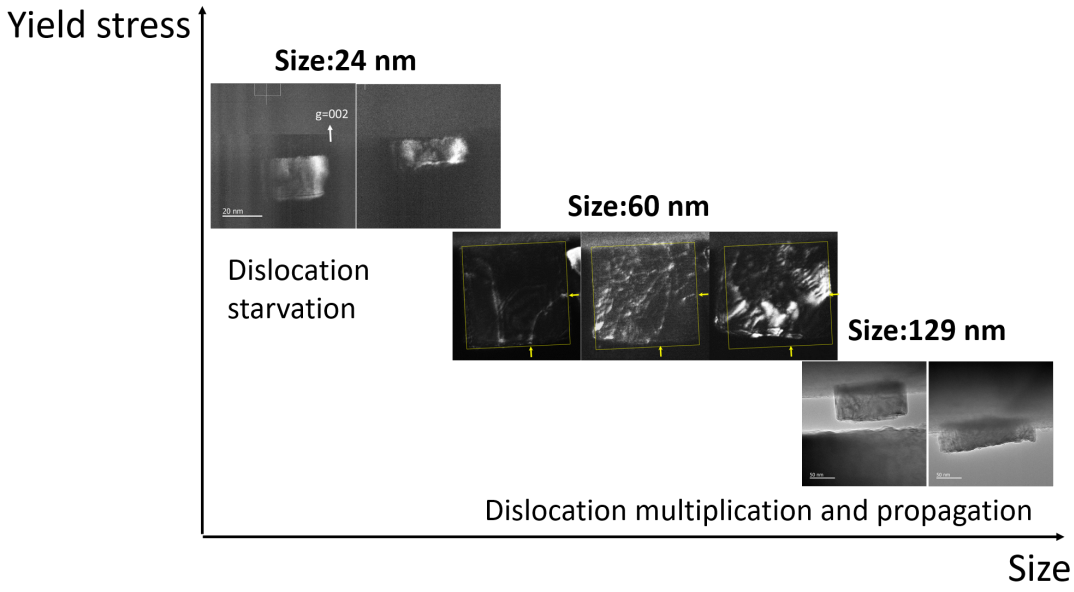

Figure 4.24 – Plastic deformation mechanisms in CeO_2

These different mechanisms were also captured in our compression tests, as shown in Fig4.24. After unloading the cube of size 24 nm, only few dislocations are observed in the cube. We can thus reasonably consider that the mechanisms includes dislocation nucleation-starvation. In the 60 nm cube, a dislocation is marked with yellow arrows before compression. In the second image, the cube is imaged after unloading from a first cycle. We can see that one end of the dislocation is pinned after the first compression and does not completely slip out. The third image shows the cube after a second cycle. The remained dislocation as a new dislocation source and emits more dislocations. A nanocube of similar size (62nm) was studied in section 4.2. We showed that a dislocation was also pre-existing before compression, so the mechanism corresponds to dislocation multiplication.

Cette thèse est accessible à l'adresse : https://theses.insa-lyon.fr/publication/2022ISAL0090/these.pdf
© [R. Zhang], [2022], INSA Lyon, tous droits réservés

However, mechanical annealing was observed during compression, and this is related to a dislocation starvation process. In the largest cubse, the initial dislocation density is high, see the image before compression of the cube of size 129 nm. After compression, it can also be seen that there is still a high density of dislocation inside the cube. The interaction between dislocations can produce strain hardening, which we can figure out from the corresponding stress-strain curve in Fig4.21.

4.4 General conclusion of Chapter 4

In this Chapter, we first presented characteristics of the cerium oxide nanocubes. The influence of the electron beam was studied on small and large nanocubes in function of the irradiation time. Small nanocubes could be irradiated either at low dose rate or at high dose rate. From a general point of view under the electron beam, cerium oxide nanocubes present two main crystal structures. CeO_2 has the fluorite structure (Fm-3m) and Ce_2O_3 has the bixbyite structure (Ia-3). This was found by analysing TEM diffraction patterns.

Moreover, the influence of the electron beam on the oxygen content x was studied using EELS. We found that the oxygen content decreased with the electron dose, from $x = 2$ (CeO_2) to $x = 1.5$ ($CeO_{1.5}$, that is to say Ce_2O_3). An intermediate state of composition $CeO_1.74$ could be identified by irradiating small nanocubes. The structure of this intermediate state has a bixbyite structure.

There was already a study reported that smaller CeO_2 particles are more easily reduced, so we also explored the effect of size on phase transition. We found that small sizes are indeed more easily transformed into bixbyite under the same irradiation conditions. The reduction ability was found within different planes. Under the same electron beam irradiation conditions, the {011} planes are less susceptible to reduction relative to the {001} planes. The {011} planes are more stable and maintain the original crystal structure. Although small particles are more easily reduced, we also found in the experiments that some small particles were not easily reduced. It is assumed that reduction from the {100} planes affects more easily the core of small nanocubes that that of large nanocubes,

Cette thèse est accessible à l'adresse : https://theses.insa-lyon.fr/publication/2022ISAL0090/these.pdf
© [R. Zhang], [2022], INSA Lyon, tous droits réservés

which makes them more sensitive to phase change. However, it is assumed that the small cubes that do not undergo reduction contain a higher proportion of {100} planes than the ones that change from fluorite to bixbyite.

In summary, the phase transition of the particles is influenced by the size and the ratio of the different facets. Therefore, the information of the phase needed to be clarified by analysing the diffraction pattern during the mechanical tests. As it was not possible to acquire meaningful EELS spectra during the compression tests, the oxygen content x was not monitored *in situ*. The nanocubes were nominally called "CeO_2" when found with the fluorite structure and will be called "Ce_2O_3" in the next chapter, when found in the bixbyite structure.

The preferred slip system in CeO_2 was then determined by analysing the sample under different zone axes and tracing the configuration changes of dislocations during compression. In our conditions where the primary slip system <110>{100} in CeO_2 cannot be activated, it was found that <110>{111} is more likely to be the active slip system than <110>{110}.

While exploring the slip system, we also found that dislocations can depleted in the cube. This is the same phenomenon in small sized metals during deformation. An effect of the nanocube size on the yield stress is also present in CeO_2. The best fit gave an exponent $c = 0.97 \pm 0.15$, which corresponds to the expected value from the literature. This fit is also in agreement with the theoretical curve computed for Frank-Read dislocation sources. Moreover, we noticed that the smaller cubes exhibited yield stress slightly above the curves, which suggested a dislocation nucleation-starvation mechanism. This was supported by the videos acquired during the compression tests. Indeed, we found that, for smaller cubes, dislocation nucleation-starvation is more likely to occur whereas for bigger cube, the deformation is dominated by dislocation multiplication and propagation.

Cette thèse est accessible à l'adresse : https://theses.insa-lyon.fr/publication/2022ISAL0090/these.pdf
© [R. Zhang], [2022], INSA Lyon, tous droits réservés

Chapter 5

In situ Nanocompression of Ce_2O_3 nanocubes

In this chapter, we show experimental results concerning the compression of Ce_2O_3 nanocubes. After the main slip systems in the complex bixbyite structure are clarified, experimental results on compressed Ce_2O_3 nanocubes are shown. By analysing a high-resolution video, we observe the dissociation of a perfect dislocation into two partial dislocations with a stacking fault. The dislocation dissociation and stacking fault formation mechanism in Ce_2O_3 is discussed by comparing our results with those found in the literature on FCC metals. We also use the models reported in the literature.

5.1 Determination of the primary slip system in Ce_2O_3

Speculating slip systems in complex materials is one of the applications of the "layered atom stacking concept" [SIK 05]. According to this concept, glide occurs mainly in the atomic layer composed of a triangular atom network (consisting of equilateral triangles formed by joining one type of atoms, whether anions or cations), also known as Kagome lattice [MEK 03]. Because the atomic density is high, the layer spacing between these triangular atom networks is large. Considering these planes with such characteristics, gliding will be easy, just like in the densest planes in metals.

Cette thèse est accessible à l'adresse : https://theses.insa-lyon.fr/publication/2022ISAL0090/these.pdf
© [R. Zhang], [2022], INSA Lyon, tous droits réservés

As an example, we defined the triangular atom network (drawn in yellow in Fig5.1(a).) to the cation stacking reported in the literature for $MgAl_2O_4$ [MIT 99]. According to the "layer atom stacking concept", the Burgers vectors of perfect 1/2 <110> dislocations correspond to the distances between opposite vertices of the kagome lattice (Fig5.1(b)) . Moreover, the possible dissociation schemes correspond to the directions given by the triangles in the kagome lattice.

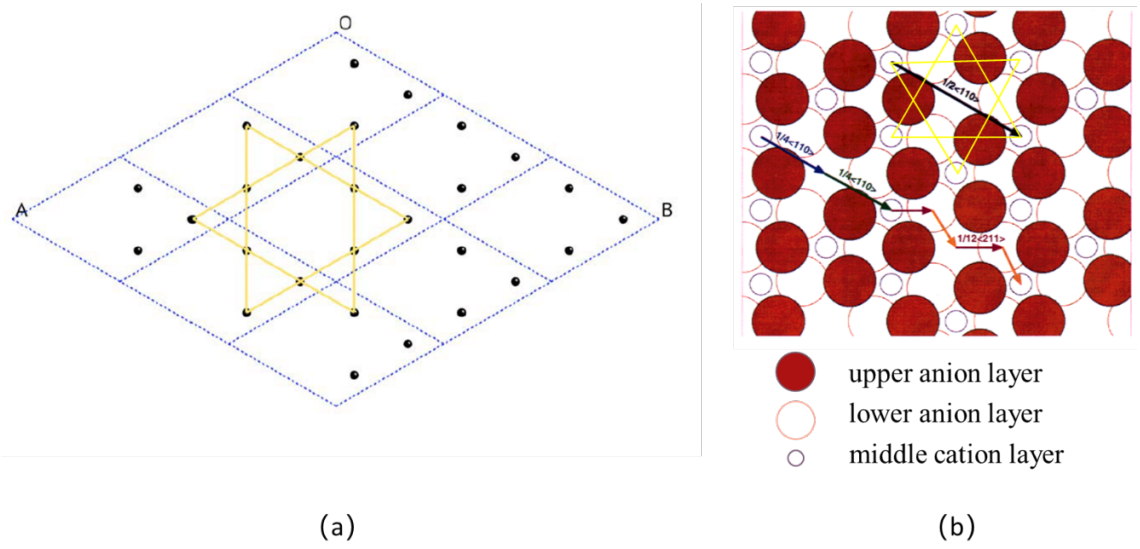

Figure 5.1 – (a) Kagome lattice of cations in the (111) plane of spinel $MgAl_2O_4$. The characteristic kagome star is shown in yellow.[SIC 06] (b) {111} Kagome lattice in the (111) plane of spinel $MgAl_2O_4$, with all cations and anions. A Perfect ½<110> Burgers vector is shown as well as its possible dissociation schemes [MIT 99] [ESP 12]

We applied the same method to bixbyite-Ce_2O_3 to determine its kagome lattice. The arrangement of the {111} cation and anion layers are illustrated in Fig5.2. Cations form a perfectly triangular network, as shown in Fig5.2(b). The anion layer is shown in Fig5.2(b). The anion triangular network is incomplete, due to oxygen vacancies. A Y-type pattern describes correctly the distribution of the oxygen anions and the vacancies (see Fig5.2(c) with the zone axis [1-11]). So, the kagome pattern in {111} planes of bixbyite is a Y-type, or wishbone, pattern.

With the layered atom stacking concept, the primary slip systems in Ce_2O_3 can be

Cette thèse est accessible à l'adresse : https://theses.insa-lyon.fr/publication/2022ISAL0090/these.pdf
© [R. Zhang], [2022], INSA Lyon, tous droits réservés

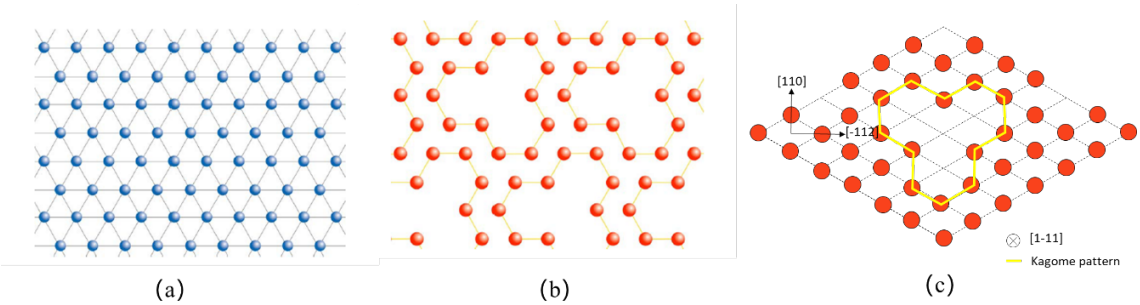

Figure 5.2 – (a) Cation arrangement in the $\{111_r brace$ planes in bixbyite, with a triangular lattice (b) Anions arrangement in the {111} planes in bixbyite. (c) Kagome pattern in yellow, revealing a Y-type or wishbone configuration of anions and vacancies. Zone axis [1-11] [SIC 06].

predicted. To do so, the kagome patterns were drawn for cations and anions, in different planes with low indices. Then, we defined the different shear vectors corresponding to the shortest periodicity in these different planes, as shown in Fig 5.3.

The shortest periodicity vectors for cerium cations are indicated by red arrows in the upper row in Fig 5.3. The shortest periodicity vectors of oxygen anions are indicated by red arrows in the bottom row in Fig 5.3. The coordinates of these vectors are given in Table 5.1.

	Cerium cation (8b)	Magnitude of the vector (Å)	Oxygen anion (16c)	Magnitude of the vector (Å)
(100)	1/2[010]	5.5	[010]	11.0
(110)	1/2[-111]	9.53	1/2[-111]	9.53
(111)	1/2[-110]	7.78	[0-11]	15.56

Table 5.1 – Shortest periodicity vectors and their magnitudes in Ce_2O_3.

From Table 5.1, it can be seen that the shortest periodicity vector, among those listed in Ce_2O_3 with bixbyite structure, is 1/2 [010] (5.5 Å) in the (100) plane. However, the Burgers vector corresponds to the shortest periodicity vector simultaneously for the cerium and oxygen atoms. Therefore, the Burgers vectors can be found as [010] in the (100) plane, 1/4[-111] in the (110) plane, and [0-11] in the (111) plane. A priority order is proposed by comparing the lengths of the Burgers vectors and is found as follows : <010>{100}

Cette thèse est accessible à l'adresse : https://theses.insa-lyon.fr/publication/2022ISAL0090/these.pdf
© [R. Zhang], [2022], INSA Lyon, tous droits réservés

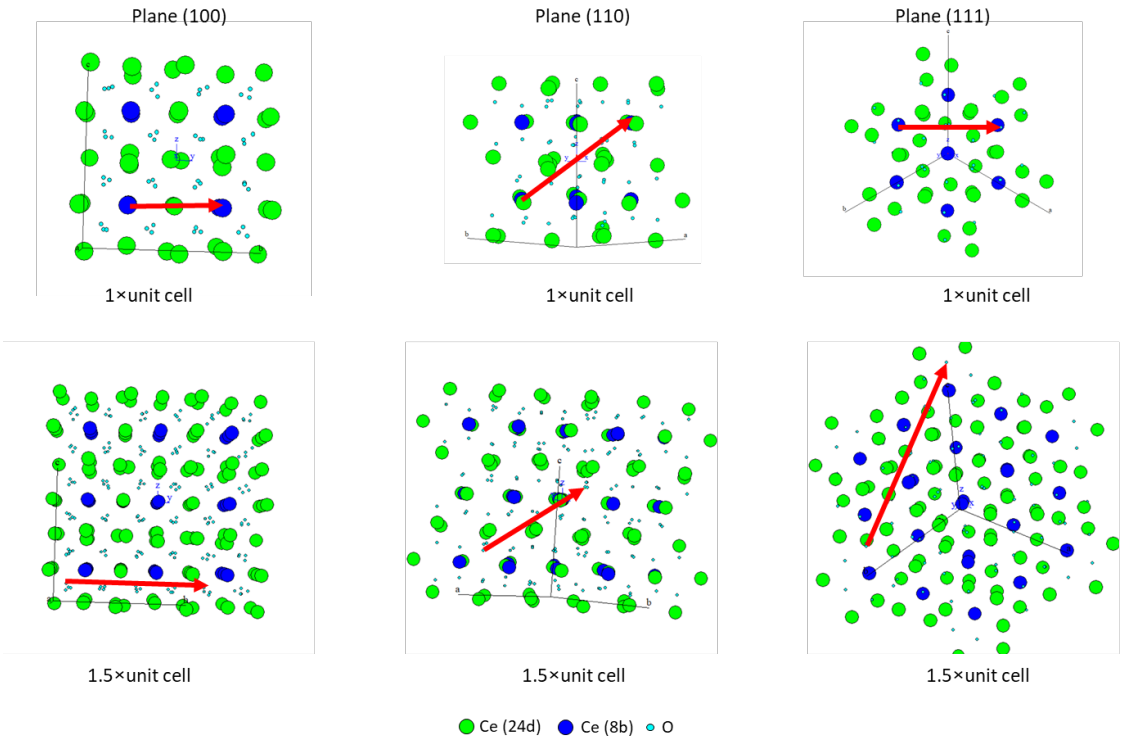

Figure 5.3 – (100), (110) and (111) planes of the bixbyite structure of Ce_2O_3. The upper row shows the shortest periodicity vectors for the cerium cations, indicated by red arrows. The bottom row shows the shortest periodicity vectors for the oxygen anions, indicated by red arrows.

(primary slip system), 1/4<-111>{110}, <0-11>{111}.

It is worth mentioning that the bixbyite structure has a large unit cell (a= 1.141 nm for Ce_2O_3), which leads to large unit slip distances and large Burgers vectors. However, dislocations that have large Burgers vectors do not glide easily. These dislocations, with large Burgers vectors, have significant energy in their core, and, thus, easily dissociate to form a stacking fault to reduce their energy. This is also clear in Table 2.4, and the literature agrees that dislocation dissociation happens in the bixbyite structure [SHA 00] [GAB 78] [GAB 09].

Cette thèse est accessible à l'adresse : https://theses.insa-lyon.fr/publication/2022ISAL0090/these.pdf
© [R. Zhang], [2022], INSA Lyon, tous droits réservés

5.2 *In situ* compression experiments on Ce_2O_3 nanocubes

One Ce_2O_3 cube of size 52 nm was compressed with a loading rate of 0.1 nm/s. Fig 5.4a presents the original state of the cube. In order to reach the atomic resolution and make sure that the cube was irradiated into bixbyite, the electron beam was highly condensed and the cube could not be observed entirely. Moreover, the cube was partially hidden by the substrate. Nevertheless, before compression, almost no defects (no dislocations, nor stacking faults) were observed in the high-resolution images, see Fig 5.4b. Fig 5.4c represents the DP of the cube. It is characteristic of the bixbyite structure, with the zone axis [110].

Moreover, because the position of this cube did not allow a full view of the cube, it is not possible to calculate the stress-strain from the mechanical data. Therefore, only the changes in the microstructure during compression are analyzed.

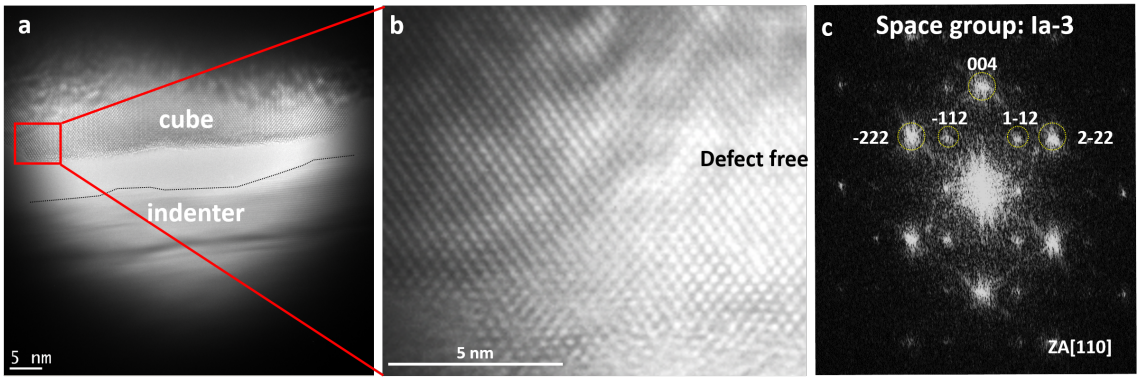

Figure 5.4 – Initial state of a 52 nm Ce_2O_3 cube before compression. (a) Image of the cube and indenter before compression. (b) High resolution image of the region of interest indicated with a red square in image (a). (c) is DP of the same region of interest. ZA=[110]

.

With the ZA [110], the crystalline planes, especially the {111} ones, can clearly be observed at the atomic scale. During compression, numerous stacking faults are generated. The stacking fault generation is illustrated in Fig 5.5. Prior to the appearance of a stacking fault, a dislocation is generated. The dislocation dissociation and the staking fault formation occurs within 0.9 seconds.

By analysing the high-resolution image in Fig 5.5b, the vector of this dislocation can be

Cette thèse est accessible à l'adresse : https://theses.insa-lyon.fr/publication/2022ISAL0090/these.pdf
© [R. Zhang], [2022], INSA Lyon, tous droits réservés

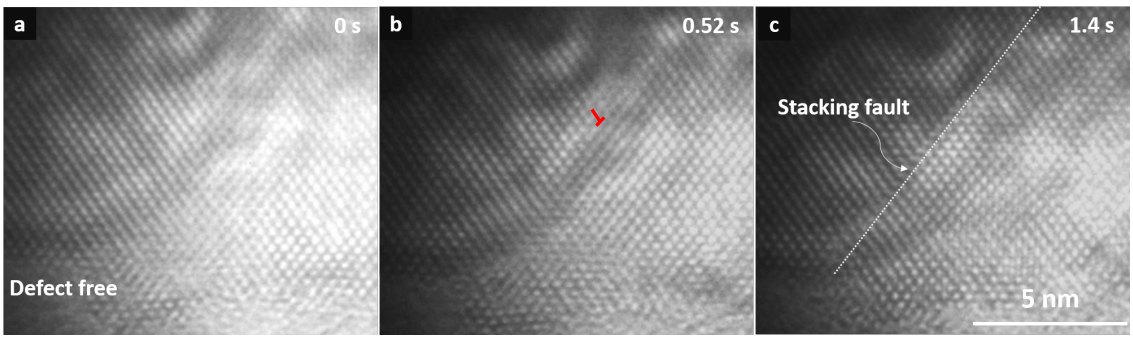

Figure 5.5 – *in situ* generation of a stacking fault in a 52 nm Ce_2O_3 nanocube. (a) Before loading, there is no defect in the cube. (b) Upon loading, a dislocation is created. (c) A stacking fault is created through dissociation of the dislocation

.

determined. Fig 5.6 shows a Burgers circuit around the dislocation core. The vector needed to complete the Burgers circuit is 1/4 [1-12]. This vector corresponds to the projection of the dislocation Burgers vector onto the image plane. Typically, in a metal with a known slip system, the Burgers vector of the dislocation may be determined directly by drawing loops in this way. However, in Ce_2O_3, the priority has not been identified between the slip systems in the {111} and {110} planes, and there are several vectors from different slip planes that are equivalent when projected onto the (110) plane. In the following analysis, we consider these possibilities and determine the actual Burgers vector of this dislocation.

In Fig 5.5(c), after compression, one side of the stacking fault ends at the surface. In order to measure the distance between two partial dislocations, the length of the stacking fault is measured in the first frame where it is visible, as shown in Fig5.7. This frame was taken during the compression at the time 1.2 s. The length is found to be 7.8 nm. By drawing Burgers circuits at each end of the stacking fault, we can obtain the projected vectors of both partial dislocations. As for the initial perfect dislocation, vectors parallel to 1/2[1-12] are needed to complete both circuits.

When further loading the sample, new stacking faults (SF2 and SF3) are generated near the first one (SF1). This is evidenced in Fig5.8, where the upper row corresponds to the TEM images and the lower one shows zoomed images of the region of interest highlighted with white rectangles and filtered using the g-vectors 2-22 and -222.

Cette thèse est accessible à l'adresse : https://theses.insa-lyon.fr/publication/2022ISAL0090/these.pdf
© [R. Zhang], [2022], INSA Lyon, tous droits réservés

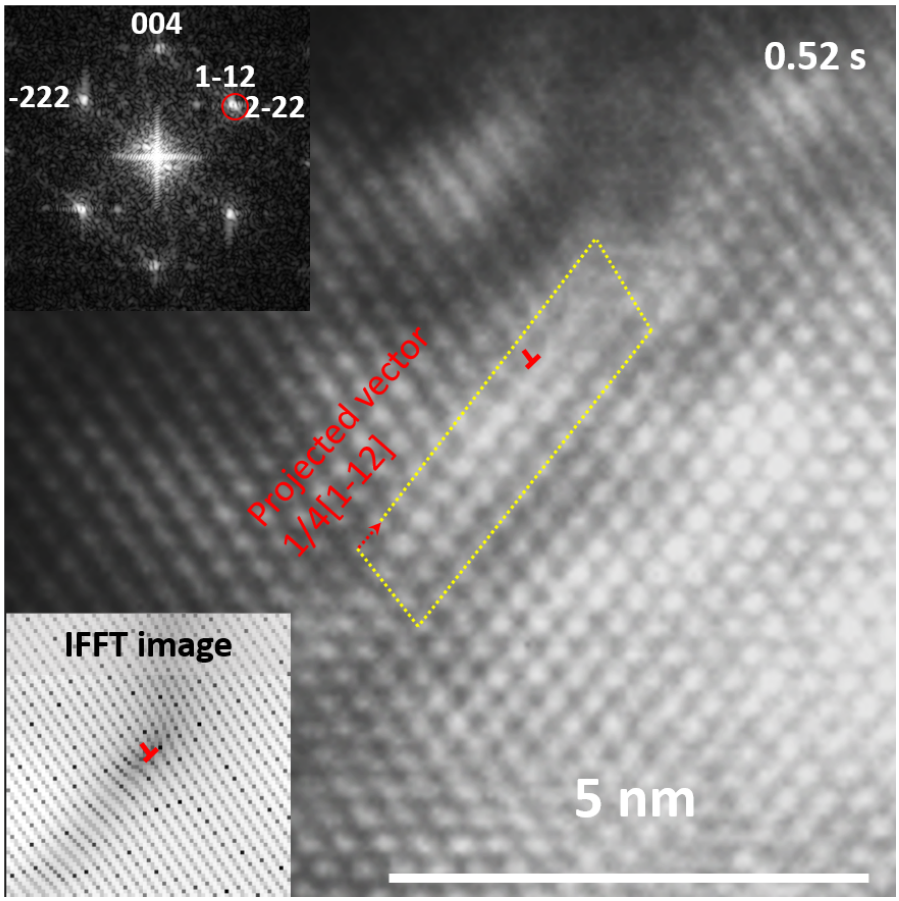

Figure 5.6 – Burgers circuit of the dislocation identified in Fig 5.5b. The circuit is drawn in yellow. The red arrow indicates the projected Burgers vector. The inset shows the corresponding DP and filtered image and filtered using the g-vector 2-22. The frame corresponds to the time 0.52 s.

SF2 is generated two atomic layers away from SF1, letting a nanotwin appear. It is generally agreed in metals that twin nucleation under deformation necessarily occurs by layer-by-layer emission of partial dislocations in a continuous atomic plane [CHR 95] [VAN 04] [ZHU 12]. But what occurs next has not been observed in metals: another stacking fault (SF3) is generated and goes through the nanotwin. The nanotwin structure is thus broken by a new stacking fault, and this process is exactly the opposite of what has been observed in the case of metals [WAN 17b].

Cette thèse est accessible à l'adresse : https://theses.insa-lyon.fr/publication/2022ISAL0090/these.pdf
© [R. Zhang], [2022], INSA Lyon, tous droits réservés

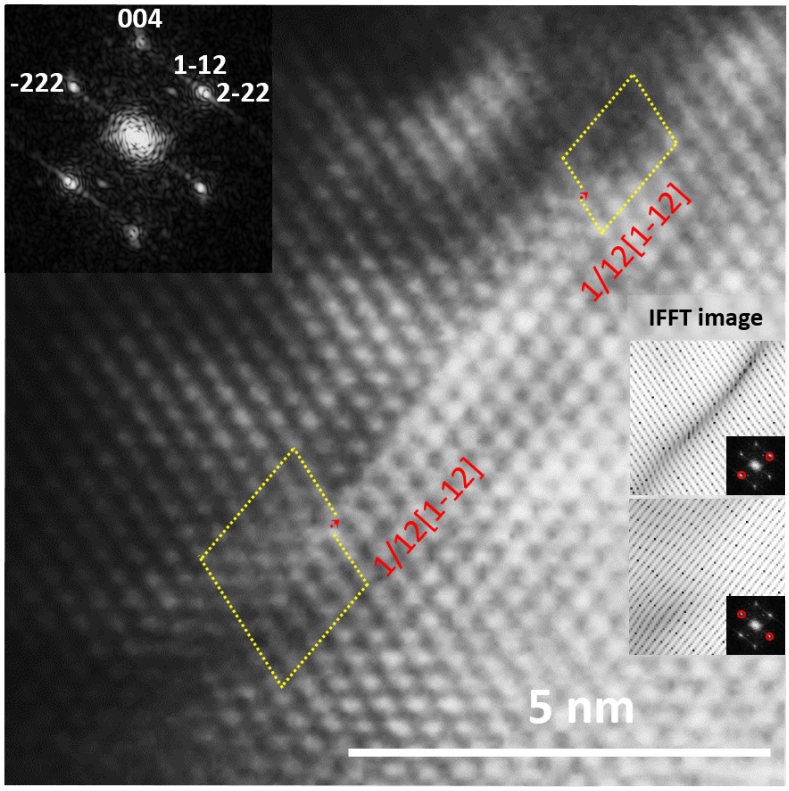

Figure 5.7 – Stacking fault generated in the Ce_2O_3 cube compressed *in situ* in Fig 5.5. The frame corresponds to the time 1,2s. Two Burgers circuits are drawn in yellow at both ends of the stacking fault. The projected Burgers vectors of the partials are shown in red. The insets give the DP and images filtered with the g-vectors 2-22 (top filtered image) and -222 (bottom filtered image).

5.3 Discussion of the deformation analysis in Ce_2O_3

From the experimental results presented above , the formation mechanism of stacking faults is similar to the one of f.c.c. metals. There is a consensus that in FCC materials, stacking faults are generated by dissociation of perfect dislocations with Burger vectors <110>{111}, and this has been verified in many experiments [VEN 61] [LAG 02] [HUA 96]. In Ce_2O_3, the sublattice of cerium atoms is a f.c.c. lattice, so we could reasonably assume that some elements of the deformation mechanism may be similar in Ce_2O_3 and metals.

However, we also have to take into account that the TEM images are two-dimensional.

Cette thèse est accessible à l'adresse : https://theses.insa-lyon.fr/publication/2022ISAL0090/these.pdf
© [R. Zhang], [2022], INSA Lyon, tous droits réservés

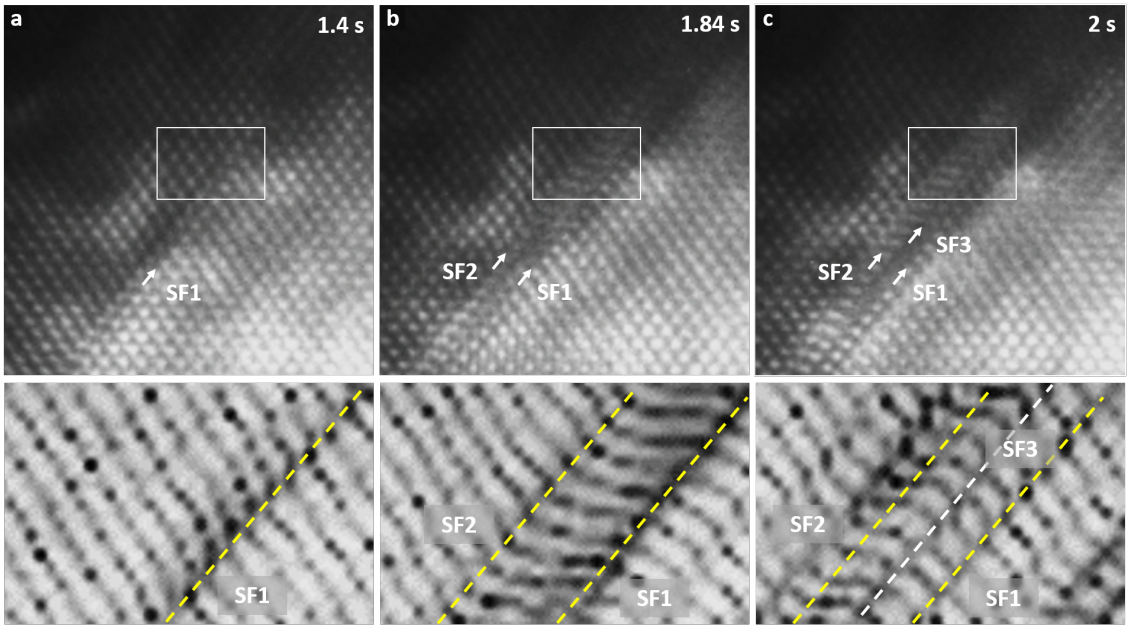

Figure 5.8 – HRTEM images of the Ce_2O_3 cube compressed *in situ* in Fig 5.5, with filtered images of the region of interest indicated by white rectangles. (a) stacking fault 1 (SF1) identified by the white arrow. (b) stacking fault 2 (SF2) created near the SF1. A nanotwin is observed between both stacking faults. (c) a new stacking fault 3 (SF3) is created between SF1 and SF2 and the nanotwin is broken.

Hence, if the expected Burgers vectors of the observed dislocations and their geometric projections on the plane perpendicular to the electron beam (in this case, the plane is (110) due to ZA=[110]) are known in advance, it is possible to determine their Burgers vectors [ROL 21]. The main issue in our case is that pieces of information lack in the literature regarding the slip systems in the bixbyite structure. In section 5.1, with the layered atom stacking concept, we identified the possible slip systems as <010>{100}, 1/2<-111>{110}, and <0-11>{111}. With these possible slip systems, it could be possible to determine the real Burgers vectors of the dislocations observed *in situ*.

In order to reduce the number of possible configurations, it is also important to consider mainly the slip systems that can be activated when the loading direction is [001]. In particular, the Schmid factors of <010>{100} and 1/2<-111>{110} are equal to zero. Excluding these slip systems, <0-11>{111} is the only slip system left to be considered.

Cette thèse est accessible à l'adresse : https://theses.insa-lyon.fr/publication/2022ISAL0090/these.pdf
© [R. Zhang], [2022], INSA Lyon, tous droits réservés

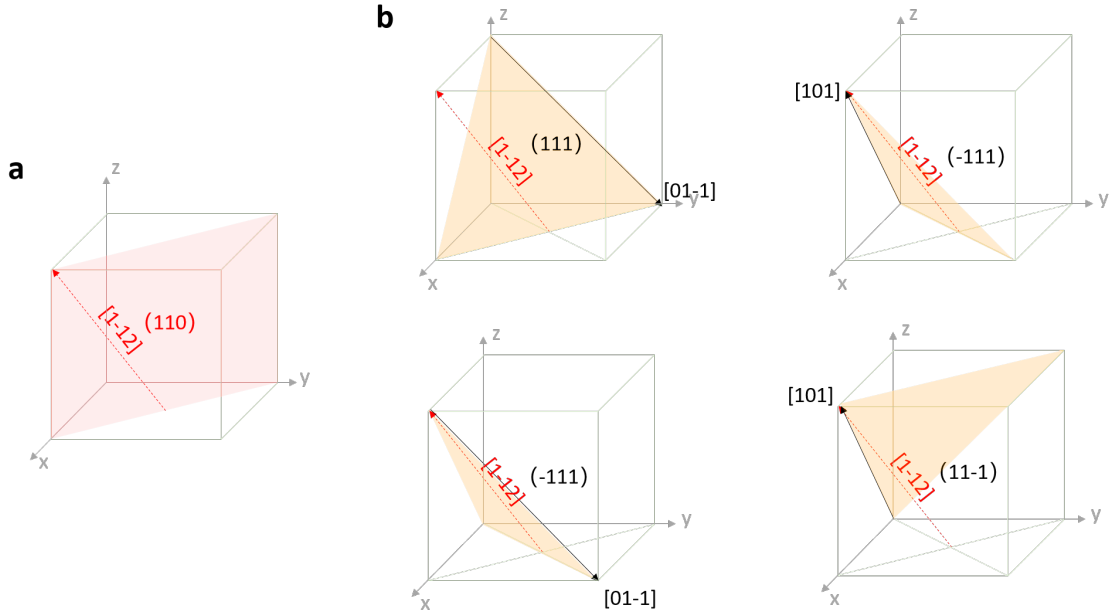

Figure 5.9 – (a) Scheme of the projected dislocation vector, determined from the TEM image in Fig 5.6. The red dashed line corresponds to the dislocation direction. The red plane corresponds to (110). (b) all possible slip systems, which have their projected vector on the plane (110) equal to [1-12]. The black solid line is the slip vector and the orange plane is the slip plane.

Fig 5.9 presents all possible vectors belonging to the <011>{111} slip system with the projection vectors on the plane (110) parallel to [1-12]. This figure presents four possibilities: [01-1](111), [101](-111), [01-1](-111) and [101](11-1). To index the dislocation, the next step involves the measurement of the vector magnitudes. The length of the projected Burgers vector is shown in Fig 5.10. By analysing the intensity profile between both ends of the Burgers circuit, the magnitude of the projected Burgers vector is measured as 0.347 nm (see left part of the figure). On the right part of the figure, the corresponding crystal structure of Ce_2O_3 is given with the ZA equal to [110]. The atoms marked in green are those in the [101] direction. In order to measure the projected distance, a scale bar is indicated with a black arrow. The scale bar is given for the direction [1-10], which is perpendicular to the ZA [110]. With this scale, it comes that the length of the vector 1/4[101] is 0.3928 nm and its projection on the (110) plane is 0.349 nm. This value is

Cette thèse est accessible à l'adresse : https://theses.insa-lyon.fr/publication/2022ISAL0090/these.pdf
© [R. Zhang], [2022], INSA Lyon, tous droits réservés

very close to what was measured in the TEM image. So, we can reasonably consider that the Burgers vector of this perfect dislocation is 1/4[101] (since 1/4[01-1] is also on the (-111) plane and belongs to the slip plane <110>{111}, we will take [101] as example in the following results). It is noteworthy that the angle between the Burgers vector and the dislocation line [110] is 60°, so this is a mixed dislocation.

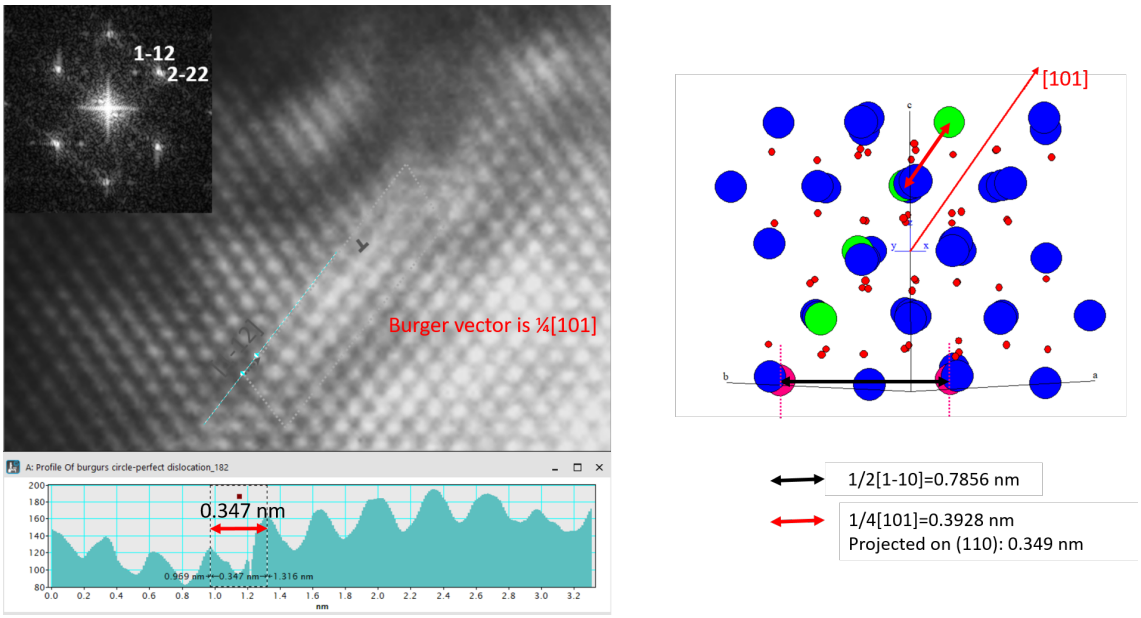

Figure 5.10 – Determination of the real Burgers vector for the perfect dislocation observed during the *in situ* compression of Ce_2O_3 in Fig 5.6.

In a similar way, the actual Burgers vector of both partials at the ends of the stacking fault SF1 can be determined. As shown in Fig5.11, the magnitude of the projected Burgers vector of the upper partial is 0.106 nm and whereas that of the lower one is 0.201 nm. The vector 1/2[1-10] is still used as scale bar. The atom marked in yellow and green indicate the [1-12] and the [211] directions, respectively. When 1/4[211] and 1/4[1-12] are projected on (110) plane, the distance are converted into 0.36 nm and 0.67 nm, respectively. Comparing distances measured in the TEM image with that in crystal structure, it is found that 0.106 nm is very close to one third of 1/4[211] projected on (110) and 0.201 nm is very close to one third of 1/4[1-12] projected on (110). So, the Burgers vector of both partials are determined as 1/12[211] (upper partial) and 1/12[1-12] (lower partial).

In summary, during *in situ* compression of the initially defect-free Ce_2O_3 cube, a perfect

Cette thèse est accessible à l'adresse : https://theses.insa-lyon.fr/publication/2022ISAL0090/these.pdf
© [R. Zhang], [2022], INSA Lyon, tous droits réservés

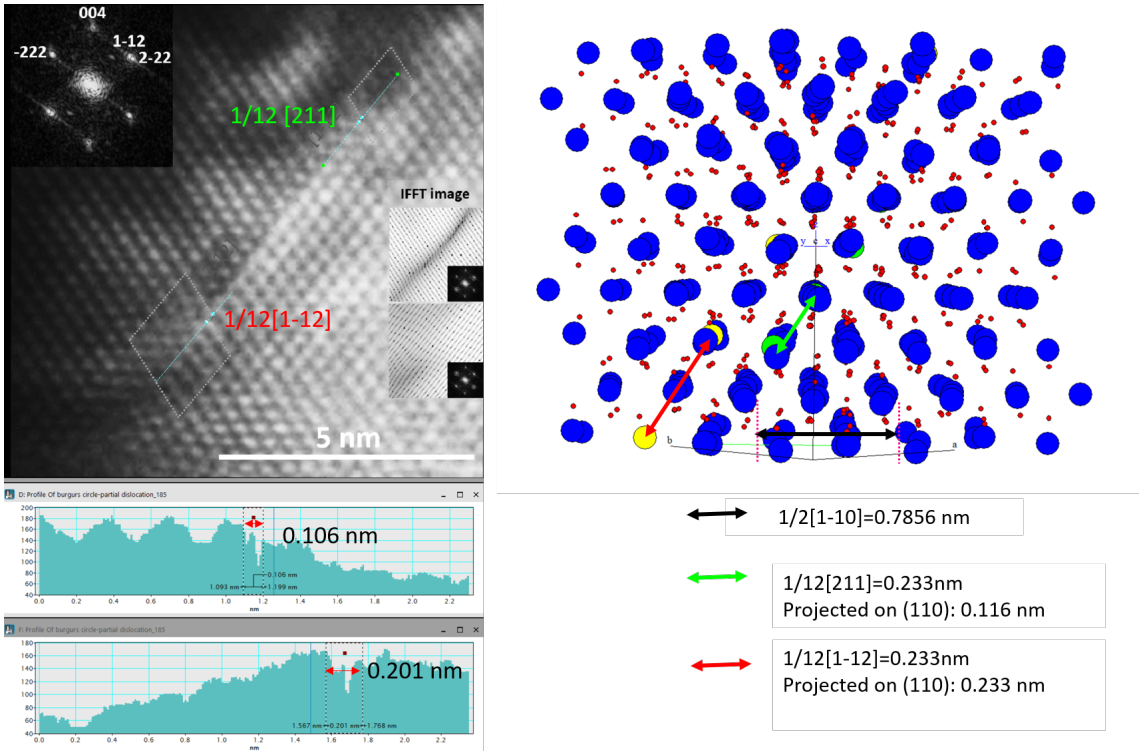

Figure 5.11 – Determination of the real Burgers vector for the partial dislocations observed during the *in situ* compression of Ce_2O_3 in Fig 5.7.

1/4[101] is created and imaged. Upon further loading, this perfect dislocation dissociates into two partial dislocations, which form a stacking fault. The Burgers vectors of both partials are 1/12[211] and 1/12[1-12]. This gives the following dissociation scheme:

$$\mathbf{1/4[101] \rightarrow 1/12[1\text{-}12] + 1/12[211]}$$

This equation is consistent from a vectorial point of view, see Fig 5.12. Moreover, this kind of dissociation has been observed in Eu_2O_3, that has the same bixbyite structure as Ce_2O_3 [NIN 90].

The formation of stacking faults in oxides is related to oxygen vacancies [SIK 05]. Fig5.13 shows the arrangement of the oxygen ions in the (1-11) plane of Ce_2O_3. As explained for the determination of the kagome lattice, there are many vacancies in this plane, and these vacancies form the letter "Y".

Upon loading, the generation of new dislocations or dislocation motions must withstand the demands of continuous deformation, resulting in very tight atomic rows. For f.c.c.

Cette thèse est accessible à l'adresse : https://theses.insa-lyon.fr/publication/2022ISAL0090/these.pdf
© [R. Zhang], [2022], INSA Lyon, tous droits réservés

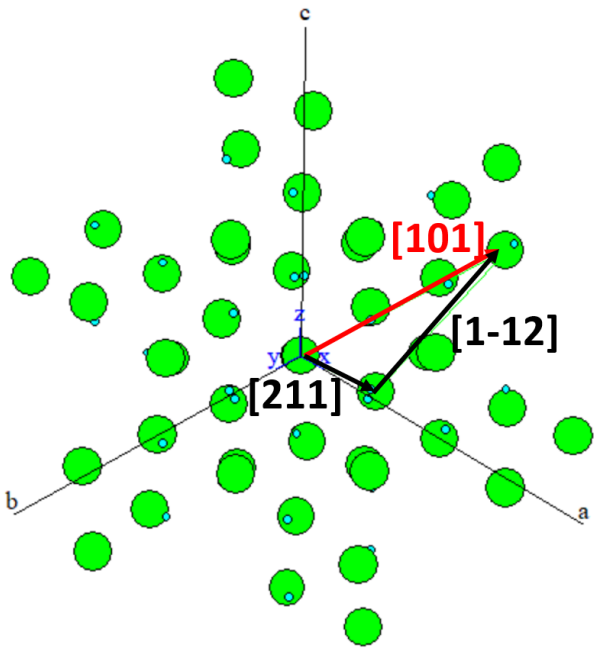

Figure 5.12 – Schematic diagram illustrating the dissociation in (-111) plane of the 1/4[101] perfect dislocation into the partials 1/12[211] and 1/12[1-12].

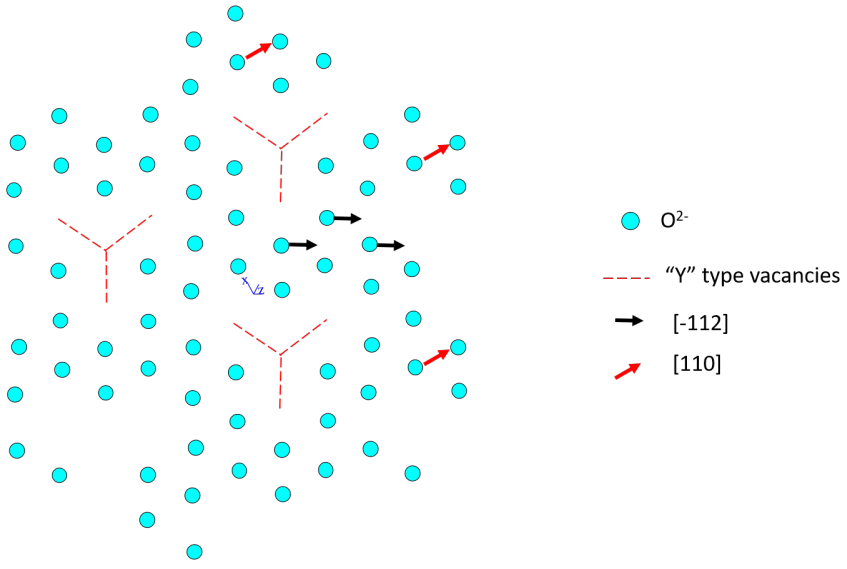

Figure 5.13 – Oxygen ions arrangement in the (1-11) plane of Ce_2O_3. (3X unit cell)

Cette thèse est accessible à l'adresse : https://theses.insa-lyon.fr/publication/2022ISAL0090/these.pdf
© [R. Zhang], [2022], INSA Lyon, tous droits réservés

crystals, with low stacking faults energies (SFE), it is more efficient to reduce the energy by dissociation than to form new dislocations or dislocation plugging to form junctions. In Ce_2O_3, one favorable feature for dislocation dissociation is the presence of oxygen vacancies. In some other atomic rows containing oxygen vacancies, the oxygen atoms of the dislocation can migrate to the vacancies and thus achieve dissociation. The black arrows in the figure indicate the direction of a partial dislocation. It is obvious that because of the presence of oxygen vacancies, partial dislocations and stacking faults can be formed more easily. Oxygen vacancies therefore directly contribute to the dissociation of mixed dislocations, as well as the formation of partial dislocations. This phenomenon was observed close to the sample surface. In Eu_2O_3, which has a bixbyite structure, the formation of partial dislocations were observed on the sample surface [NIN 90].

It is also interesting to compare the behaviour of Ce_2O_3 with that of metals. In bulk aluminum, plasticity is mainly dominated by dislocations. However, the generation of stacking faults and twins is more favorable in polycrystalline Al when the critical grain size D_c is around 10 nm [CHE 03]. This implies that the sample size also has an effect on dislocation dissociation [CHE 03]. We can try to determine which mechanism is more likely to dominate plastic deformation in f.c.c. materials by comparing the critical shear stress to generate a perfect 1/2<110> dislocation with the stress required to generate partial 1/12<112> dislocations.

The critical shear stress τ_N for the nucleation of a perfect dislocation is [LAG 02] [AND 17]:

$$\tau_N = \frac{2\alpha\mu b_N}{D}$$

And the critical shear stress τ_P for the nucleation of a shorkley partial dislocation is:

$$\tau_P = \frac{2\alpha\mu b_P}{D} + \frac{\gamma}{b_P}$$

Where:

— α is a parameter reflecting the character of the dislocation. For edge dislocations $\alpha = 0.5$ and for screw dislocations $\alpha = 1.5$ [AND 17]. In our experiment, the dislocation type is mixed one, so we consider α equal to 1.

— D is the grain size. Here, as the nanocubes are monocrystalline, we take the size of

Cette thèse est accessible à l'adresse : https://theses.insa-lyon.fr/publication/2022ISAL0090/these.pdf
© [R. Zhang], [2022], INSA Lyon, tous droits réservés

nanocube (52 nm)

— μ is the shear modulus. Here we take 66.5 GPa, from simulation results performed by Gaëtan Laurens and Tristan Albaret at ILM within the ANR project.

— b_N and b_P are the magnitudes of the perfect dislocations and the partial dislocations, respectively.

— γ is the stacking fault energy (SFE). γ can be estimated using the following equation [FOS 13]:

$$\gamma = \frac{\mu \mathbf{b_1} \cdot \mathbf{b_2}}{2d\pi K}$$

Where:

— b_1 and b_2 are the Burgers vectors of the partial dislocations;

— d is the distance between both partial dislocations. Here, we use the value measured on the TEM image (see Fig 5.7);

— μ is the shear modulus, taken as 66.5 GPa (see above);

— K is a factor that can be expressed as: $K = \frac{1-\nu}{(1-\nu)\cos^2\theta + \sin^2\theta}$

— ν is the Poisson's ratio: 0.291, from simulation results performed by Gaëtan Laurens and Tristan Albaret at ILM within the ANR project ;

— θ is the angle between the dislocation line and the Burger vector. Here θ is 60°.

μ	D	b_N	b_P	d	γ	τ_N	τ_P
GPa	nm	nm	nm	nm	mJ/m^2	GPa	GPa
66.5	52	0.403	0.233	7.8	96.39	1.03	1.01

Table 5.2 – Values of the parameters used for the computation of γ, τ_N and τ_P for bixbyite Ce_2O_3. μ is the shear modulus. D is the sample size. b_N and b_P are the magnitudes of the Burgers vectors of 1/4 [110] perfect dislocations, and 1/12[1-12] partial dislocations, respectively. d is the distance between two partial dislocations. γ is the stacking fault energy. τ_N is the critical shear stress required to generate a 1/4 [110] perfect dislocation and τ_P is critical shear stress required to generate a 1/12[1-12] partial dislocation.

The values of γ, τ_N and τ_P are shown in Table 5.2. The SFE, γ, is found to be equal to 96.39 mJ/m^2. For aluminum and copper, the SFE is around 160 mJ/m^2 [MUR 75] and 70 mJ/m^2 [ZHA 05], respectively. Compared with metallic materials, Ce_2O_3 seems to exhibit a low SFE. This is surprising as the SFEs of oxides are in general very large,

Cette thèse est accessible à l'adresse : https://theses.insa-lyon.fr/publication/2022ISAL0090/these.pdf
© [R. Zhang], [2022], INSA Lyon, tous droits réservés

as in aluminum oxides [YAM 02]. Moreover, as far as bixbyite is concerned, Boisson et al. calculated the SFE for different sliding systems in Y_2O_3, and they found that the SFE can be reach 7197 mJ/m^2 [BOI 77]. It is interesting to note that they found a low SFE for a shear vector 1/2[110] on the (001) plane, equal to 80 mJ/m^2. This value is close to the one calculated here, but our value refers to the shear vector 1/12[1-12] on (-111) plane. Unfortunately, no calculation of SFEs in Ce_2O_3 has been reported in the literature so far and simulations performed by ILM are still under work. Since we cannot rely on reference values, we will only do exploratory research here.

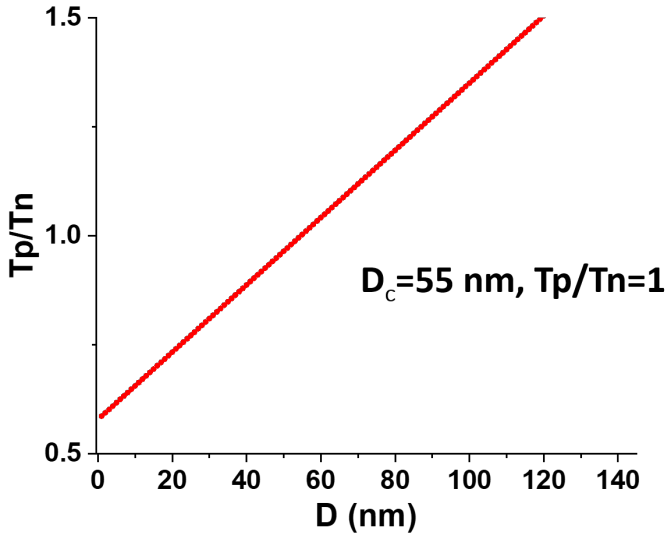

Figure 5.14 – Evolution of the ratio τ_N/τ_P (critical shear stress for the nucleation of a perfect 1/4 <110> dislocation divided by the critical shear stress for the nucleation of a partial 1/12 <112> dislocation) with the sample size D.

Fig 5.14 shows the evolution of the ratio τ_N/τ_P for bixbyite Ce_2O_3, as a function of the sample size D. It is obtained from the equations above and by considering the SFE value of 96.39 mJ/m² A critical size D_c can be defined, for which $\tau_N = \tau_P$. We obtain D_c = 55 nm. The size of cube we compressed being 52 nm, below D_c, we notice that $\tau_P < \tau_N$.

When $\tau_P < \tau_N$, the nucleation of a partial 1/12<112> dislocation requires a lower critical stress than the nucleation of a perfect 1/4 <110> dislocation. From Chen's work,

Cette thèse est accessible à l'adresse : https://theses.insa-lyon.fr/publication/2022ISAL0090/these.pdf
© [R. Zhang], [2022], INSA Lyon, tous droits réservés

in Al films, plastic deformation is dominated by stacking faults and deformation twinning because of the large difference between the τ_N and τ_P. In the 52 nm Ce_2O_3 cube, however, both values are very close to each other (from table 5.2, τ_N = 1.03 GPa, and τ_P = 1.01GPa).

At this point, it is important to remind that the distance between partial dislocations used in our calculation is the distance measured on high resolution images extracted from the video. The time difference between the image of the perfect dislocation and the image with the partial dislocations is 0.12 s (The video is 25 frames per second, and there are 3 frames between the images). Although the time is short, it cannot be maintained to be the moment when the SF is initially formed. This may be a reason why our value of SFE is very low. When calculating the dissociation distance in UO_2 (Fluorite), Fossati et al. argue that on {111} planes the dissociation distance is about twice the 1/2<110> Burgers vector [FOS 13]. By considering this assumption in the case of Ce_2O_3, the distance between two partials would rather be about 0.806 nm. Table 5.3 gathers updated values obtained by considering this dissociation distance. These values can be compared with the ones presented in table 5.2.

μ	D	b_N	b_P	d	γ	τ_N	τ_P
GPa	nm	nm	nm	nm	mJ/m^2	GPa	GPa
66.5	52	0.403	0.233	0.806	932.8	1.03	4.60

Table 5.3 – Updated values of γ, τ_N and τ_P for bixbyite Ce_2O_3, when the distance d between partials is changed to 0.806 nm (other parameters D, b_N, b_P unchanged).

The main result of table 5.3 is that the value of γ, the SFE, now reaches the usual level for oxides. However, with such a high SFE, the shear stress required to generate a partial dislocation is also increased a lot and the critical size D_c is now around 5 nm. This implies that the dislocation will more easily dissociate when the cube size lies below 5 nm. However, such result disagrees with our observations: a large number of stacking faults have been observed in the 52 nm Ce_2O_3 nanocube,which is not consistent with Chen's model.

Cette thèse est accessible à l'adresse : https://theses.insa-lyon.fr/publication/2022ISAL0090/these.pdf
© [R. Zhang], [2022], INSA Lyon, tous droits réservés

The explanation from the perspective of the oxygen atom network is more consistent with the experimentally observed results. Indeed, the results from Gaboriaud et al. [GAB 13] are very similar to ours. Under ion irradiation, stacking faults were generated in the {222} planes in bisbyite Y_2O_3. The authors suggest that the formation of stacking fault is mainly due to the characteristic arrangement of oxygen atoms in the {222} planes. As mentioned above, there are "Y-shaped" arrangement of oxygen vacancies, which probably facilitates the generation of stacking faults since dislocations are easily produced on the {111} planes.

5.4 General conclusion of Chapter5

In this chapter, we first studied the different slip systems in Ce_2O_3 from the point of view of crystallography. Due to the complexity of the bixbyite structure and missing information in the literature, we used the "layered atom stacking concept" to determine its shortest periodicity vectors. The analysis of the kagome lattice in the (111) plane led to the following slip system: **<010>**{100}**, 1/4<-111>**{110}**, <0-11<**{111}.

Then we presented an *in situ* compression experiment on a Ce_2O_3 cube of size 52 nm, without visible defects in the initial state. The analysis of the high-resolution video shows the nucleation of a perfect dislocation, followed by its dissociation into two partial dislocations within a very short time (0.12 s) and the generation of a stacking fault. We identified the slip system and determined the Burgers vectors for the perfect dislocation and the partial ones.

The dissociation scheme was found to be **1/4[101]→1/12[1-12]+1/12[211]**. It is very similar to that in f.c.c. metals. However, we noticed that the dissociation of a perfect dislocation in oxides is usually not easy. We thus discussed the possibility of dislocation dissociation in Ce_2O_3. Using models from the literature [CHE 03], we tried to compute the critical shear stresses τ_N and τ_P for the nucleation of a 1/4<110> perfect dislocation and a 1/2<112> partial, respectively. Since there is a stacking fault energy involved, but this parameter is not yet available, our computed values could not be validated. Even though we applied a correction on the distance between partials and could get a value of the stacking fault energy with a correct order of magnitude, we could not explain the

Cette thèse est accessible à l'adresse : https://theses.insa-lyon.fr/publication/2022ISAL0090/these.pdf
© [R. Zhang], [2022], INSA Lyon, tous droits réservés

formation of the stacking faults in the 52 nm Ce_2O_3 nanocube. Therefore, this part stays at the discussion stage and requires further analysis. A better explanation for the stacking fault formation was found with the arrangement of the oxygen vacancies in the {111} planes. In agreement with the literature on Y_2O_3, the arrangement of the oxygen vacancies is favorable for the generation of partial dislocations with vectors <112>.

Cette thèse est accessible à l'adresse : https://theses.insa-lyon.fr/publication/2022ISAL0090/these.pdf
© [R. Zhang], [2022], INSA Lyon, tous droits réservés

Cette thèse est accessible à l'adresse : https://theses.insa-lyon.fr/publication/2022ISAL0090/these.pdf
© [R. Zhang], [2022], INSA Lyon, tous droits réservés

Conclusion

The context of this PhD work was the study of plasticity at room temperature in ceramics. Such topic still needs to be explored as the mechanisms involved have to be determined, and they may be different from those occurring in metals due to the more complex structure of ceramics. Controlling plasticity in nano-sized ceramics could moreover benefit to the elaboration of bulk fine-grained materials.

In this context, this PhD work was dealing with *in situ* mechanical tests on cerium oxide nanocubes, with sizes ranging between 20 and 130 nm). The relationship between their mechanical properties and the evolution of defects (dislocations, stacking faults) was investigated using Environment Transmission Electron Microscopy and delicate mechanical test systems. Such techniques allows a direct observation of the microstructural changes within the sample together with the acquisition of quantitative data (force, displacement).

We first introduced basic concepts on the mechanical properties of ceramic materials, with an emphasis on the effect of the sample size. the state-of-the-art also includes several studies performed on f.c.c. and b.c.c. metals as references, because few works focused on room temperature plasticity in ceramic materials.

In a second chapter, we introduced the fluorite structure and its slip systems (in CeO_2 and other fluorite oxides). As it is known to undergo reduction under the electron beam, with phase transformation from fluorite to bixbyite, information regarding the bixbyite structure (Ce_2O_3 and other oxide materials).

The third chapter was devoted to the description of the materials and experimental techniques used. We described the key steps of the sample preparation, the *in situ* test itself and data processing.

Cette thèse est accessible à l'adresse : https://theses.insa-lyon.fr/publication/2022ISAL0090/these.pdf
© [R. Zhang], [2022], INSA Lyon, tous droits réservés

The results obtained on the cerium oxide nanocubes were presented in the fourth and fifth chapters. The main results are summarized hereafter.

Firstly, we characterized the CeO_2 nanocubes by TEM. As the electron beam is known to reduce CeO_2, the fluorite-to-bixbyite phase transition was explored in function of the electron dose rate and the nanocube size. It was found that small cubes were more easily reduced from fluorite to bixbyite, as reported in the literature. However, we also found that some small cubes were not reduced, so we also explored the effect of the type of facets on the reduction. Under similar irradiation conditions, it was found that the cubes with {110} facets were more likely to keep the original structure (fluorite). Compared with {110}, the {100} planes were more easily reduced, in agreement with the literature.

We then determined the activated slip system in CeO_2 when the force direction is [001]. Two methods were used: characterization of dislocations in the sample observed after unloading with different zone axes, and dislocation analysis during the test. Knowing that the primary slip system in CeO_2 cannot be activated with this force direction, both methods indicated that the <110>{110} is the activated slip system in our experiments on CeO_2. We also saw that dislocations tend to escape from the cube surface during compression, causing dislocation depletion.

Finally on CeO_2, we investigated the dependence of the yield stress on the nanocube size. It was found that in CeO_2, the yield stress is inversely proportional to the nanocube size, as expected from the literature and observed on other materials (InGaAs, MgO, f.c.c. metals).

The position of the experimental points with respect to the best fit curve gave insight on the deformation mechanism in nano-sized CeO_2 cubes. When the cube size is small, dislocations easily escape from the nanocube surface, which results in dislocation depletion. A higher stress is thus required to nucleate new dislocations, so the experimental points are above the best fit curve. On the contrary in large cubes, the mechanism includes dislocation multiplication and propagation and the experimental points are on the best fit curve.

Secondly, we explored the deformation mechanism in bixbyite $Ce2O_3$. The "layered atom stacking concept" was used to predict the possible slip systems in $Ce2O_3$. Three

Cette thèse est accessible à l'adresse : https://theses.insa-lyon.fr/publication/2022ISAL0090/these.pdf
© [R. Zhang], [2022], INSA Lyon, tous droits réservés

possibilities were found: <010>{100}, 1/4<-111>{110}, <0-11<{111}.

During compression, we observed that many stacking faults were generated. Through the high-resolution video, the process of stacking fault generation was captured. We could indeed evidence the formation of a perfect dislocation, followed rapidly by its dissociation and the appearance of a stacking fault. Based on the possible slip systems determined from the layered atom stacking concept, we further identified the dissociation by determining the Burgers vectors of the perfect and partial dislocations. We obtained the following dissociation scheme: **1/4[101]→1/12[1-12]+1/12[211]**. It is similar to what occurs in f.c.c. metals. Dislocation dissociation occurred in bixbyite but was not observed in fluorite. In order to explain why perfect dislocation easily dissociate in bixbyite, we tried to compute the ratio between the critical shear stresses for the generation of a perfect 1/4<110> dislocation and that for the generation of a 1/12<112> partial. Unfortunately, a reliable value of the stacking fault energy could not be obtained. Another explanation of dislocation dissociation in bixbyite involvesthe arrangement of oxygen vacancies in the {111} planes, in agreement with the literature on the behaviour of Y_2O_3 under ion irradiation.

This thesis, by combining mechanical data and compression video, mainly explored the deformation mechanisms in CeO_2 and Ce_2O_3. The results are promising and add experimental evidence to the deformation of nanometer-sized ceramic materials. In the future, several aspects would need to be considered:

• More measurements are needed to better understand the effect of electron beam on the phase change. It would be interesting to include a wider range of cube sizes, electron doses and electron dose rates.

• It is necessary to perform more compression tests on small CeO_2 cubes. It would then be possible to avoid some of problems that could be caused especially on small cubes (e.g., phase transformation induced by the small size, low contrast in the videos that makes DIC unreliable).

• It would also be exciting to compare the mechanisms of plastic deformation before and after phase change, inside one single cube. It would then be possible to gain deeper understanding of the effects of phase change on mechanical properties.

Cette thèse est accessible à l'adresse : https://theses.insa-lyon.fr/publication/2022ISAL0090/these.pdf
© [R. Zhang], [2022], INSA Lyon, tous droits réservés

Cette thèse est accessible à l'adresse : https://theses.insa-lyon.fr/publication/2022ISAL0090/these.pdf
© [R. Zhang], [2022], INSA Lyon, tous droits réservés

References

[AMO 21] Amodeo J., Pizzagalli L.

Modeling the mechanical properties of nanoparticles: a review. *Comptes Rendus. Physique*, vol. 22, n° S3, 2021, p. 35–66.

[AND 17] Anderson P. M., Hirth J. P., Lothe J.

Theory of dislocations. Cambridge University Press, 2017.

[BAU 94] Baufeld B., Messerschmidt U., Bartsch M., Baither D.

Plasticity of Cubic Zirconia between 700 C and 1150 C Observed by Macroscopic Compression and by in situ Tensile Straining Tests. *Key Engineering Materials*, , 1994, p. 431–431, Trans tech publications.

[BAU 95] Baufeld B., Bartsch M., Messerschmidt U., Baither D.

Plastic deformation of cubic zirconia at temperatures between 1150 and 700° C. *Acta metallurgica et materialia*, vol. 43, n° 5, 1995, p. 1925–1933, Elsevier.

[BAU 98] Baufeld B., Baither D., Bartsch M., Messerschmidt U.

Plastic deformation of cubic zirconia single crystals at 1400 C. *physica status solidi (a)*, vol. 166, n° 1, 1998, p. 127–153, Wiley Online Library.

[BEC 71] Becher P. F.

Mechanical behaviour of polycrystalline TaC. *Journal of Materials Science*, vol. 6, n° 1, 1971, p. 79–80.

[BEN 09] Benzerga A. A.

Micro-pillar plasticity: 2.5 D mesoscopic simulations. *Journal of the Mechanics and Physics of Solids*, vol. 57, n° 9, 2009, p. 1459–1469, Elsevier.

Cette thèse est accessible à l'adresse : https://theses.insa-lyon.fr/publication/2022ISAL0090/these.pdf
© [R. Zhang], [2022], INSA Lyon, tous droits réservés

[BOI 77] Boisson M., Gaboriaud R.

Calculs d'énergie de faute d'empilement dans le sesquioxyde d'yttrium (Y2O3). *Journal de Physique Lettres*, vol. 38, n° 8, 1977, p. 177-181, Edp sciences.

[BRE 58] Brenner S.

Growth and Properties of" Whiskers" Further research is needed to show why crystal filaments are many times as strong as large crystals. *Science*, vol. 128, n° 3324, 1958, p. 569–575, American Association for the Advancement of Science.

[BRI 08] Brinckmann S., Kim J.-Y., Greer J. R.

Fundamental differences in mechanical behavior between two types of crystals at the nanoscale. *Physical review letters*, vol. 100, n° 15, 2008, Page 155502, APS.

[BRU 01] Brunner D., Taeri-Baghbadrani S., Sigle W., Rühle M.

Surprising results of a study on the plasticity in strontium titanate. *Journal of the American Ceramic Society*, vol. 84, n° 5, 2001, p. 1161–1163, Wiley Online Library.

[BUG 17] Bugnet M., Overbury S. H., Wu Z. L., Epicier T.

Direct visualization and control of atomic mobility at {100} surfaces of ceria in the environmental transmission electron microscope. *Nano Letters*, vol. 17, n° 12, 2017, p. 7652–7658, ACS Publications.

[BUS 26] Busch H.

Berechnung der Bahn von Kathodenstrahlen im axialsymmetrischen elektromagnetischen Felde. *Annalen der Physik*, vol. 386, n° 25, 1926, p. 974–993, Wiley Online Library.

[BUS 04] Bushby A., Dunstan D.

Plasticity size effects in nanoindentation. *Journal of materials research*, vol. 19, n° 1, 2004, p. 137–142, Cambridge University Press.

[BUT 05] Butt H.-J., Cappella B., Kappl M.

Force measurements with the atomic force microscope: Technique, interpretation and applications. *Surface science reports*, vol. 59, n° 1-6, 2005, p. 1–152, Elsevier.

[CAD 16] Caddeo F., Corrias A., Sayle D. C.

Tuning the properties of nanoceria by applying force: stress-induced ostwald ripening.

Cette thèse est accessible à l'adresse : https://theses.insa-lyon.fr/publication/2022ISAL0090/these.pdf
© [R. Zhang], [2022], INSA Lyon, tous droits réservés

The Journal of Physical Chemistry C, vol. 120, n° 26, 2016, p. 14337–14344, ACS Publications.

[CAL 12] Calvié E., Joly-Pottuz L., Esnouf C., Clément P., Garnier V., Chevalier J., Jorand Y., Malchère A., Epicier T., Masenelli-Varlot K.
Real time TEM observation of alumina ceramic nano-particles during compression. *Journal of the European Ceramic Society*, vol. 32, n° 10, 2012, p. 2067–2071, Elsevier.

[CAL 14] Calvié E., Réthoré J., Joly-Pottuz L., Meille S., Chevalier J., Garnier V., Jorand Y., Esnouf C., Epicier T., Quirk J. et al.
Mechanical behavior law of ceramic nanoparticles from transmission electron microscopy in situ nano-compression tests. *Materials Letters*, vol. 119, 2014, p. 107–110, Elsevier.

[CHE 89] Cheong D.-S., Dominguez-Rodriguez A., Heuer A. H.
High-temperature plastic deformation of Y2O3-stabilized ZrO2 single crystals. II. Electron microscopy studies of dislocation substructures. *Philosophical Magazine A*, vol. 60, n° 1, 1989, p. 123–138, Taylor & Francis.

[CHE 91] Cheong D.-S., Dominguez Rodriguez A., Heuer A. H.
High-temperature plastic deformation of Y2O3-stabilized ZrO2 single crystals III. Variation in work hardening between 1200 and 1500° C. *Philosophical Magazine A*, vol. 63, n° 3, 1991, p. 377–388, Taylor & Francis.

[CHE 03] Chen M., Ma E., Hemker K. J., Sheng H., Wang Y., Cheng X.
Deformation twinning in nanocrystalline aluminum. *Science*, vol. 300, n° 5623, 2003, p. 1275–1277, American Association for the Advancement of Science.

[CHR 95] Christian J. W., Mahajan S.
Deformation twinning. *Progress in materials science*, vol. 39, n° 1-2, 1995, p. 1–157, Elsevier.

[COP 65] Copley S. M., Pask J. A.
Plastic deformation of MgO single crystals up to 1600 C. *Journal of the American Ceramic Society*, vol. 48, n° 3, 1965, p. 139–146, Wiley Online Library.

[COU 05] Courtney T. H.
Mechanical behavior of materials. Waveland Press, 2005.

Cette thèse est accessible à l'adresse : https://theses.insa-lyon.fr/publication/2022ISAL0090/these.pdf
© [R. Zhang], [2022], INSA Lyon, tous droits réservés

[CRA 80] Crampon J., Escaig B.

Mechanical properties of fine-grained magnesium oxide at large compressive strains. *Journal of the American Ceramic Society*, vol. 63, n° 11-12, 1980, p. 680–686, Wiley Online Library.

[CSI 07] Csikor F. F., Motz C., Weygand D., Zaiser M., Zapperi S.

Dislocation avalanches, strain bursts, and the problem of plastic forming at the micrometer scale. *Science*, vol. 318, n° 5848, 2007, p. 251–254, American Association for the Advancement of Science.

[DAS 07] Da Silva J. L.

Stability of the Ce 2 O 3 phases: A DFT+ U investigation. *Physical Review B*, vol. 76, n° 19, 2007, Page 193108, APS.

[DIM 05] Dimiduk D., Uchic M., Parthasarathy T.

Size-affected single-slip behavior of pure nickel microcrystals. *Acta materialia*, vol. 53, n° 15, 2005, p. 4065–4077, Elsevier.

[DIN 16] Ding Y., Chen Y., Pradel K. C., Liu M., Lin Wang Z.

In-situ transmission electron microscopy study of oxygen vacancy ordering and dislocation annihilation in undoped and Sm-doped CeO2 ceramics during redox processes. *Journal of Applied Physics*, vol. 120, n° 21, 2016, Page 214302, AIP Publishing LLC.

[DOM 91a] Dominguez-Rodriguez A., Cheong D.-S., Heuer A. H.

High-temperature plastic deformation in Y2O3-stabilized ZrO2 single crystals: IV. The secondary slip systems. *Philosophical Magazine A*, vol. 64, n° 4, 1991, p. 923–929, Taylor & Francis.

[DOM 91b] Dominguez-Rodriguez A., Heuer A. H., Castaing J.

Dislocations and the mechanical properties of stabilized ZrO2. *Radiation Effects and Defects in Solids*, vol. 119, n° 2, 1991, p. 759–769, Taylor & Francis.

[DUN 91] Dunstan D., Kidd P., Howard L., Dixon R.

Plastic relaxation of InGaAs grown on GaAs. *Applied physics letters*, vol. 59, n° 26, 1991, p. 3390–3392, American Institute of Physics.

Cette thèse est accessible à l'adresse : https://theses.insa-lyon.fr/publication/2022ISAL0090/these.pdf
© [R. Zhang], [2022], INSA Lyon, tous droits réservés

[DUN 12] Dunstan D.

Critical thickness theory applied to micromechanical testing. *Advanced Engineering Materials*, vol. 14, nº 11, 2012, p. 942–947, Wiley Online Library.

[DUN 17] Dunstan D. J.

The size effect in the mechanical strength of semiconductors and metals: strain relaxation by dislocation-mediated plastic deformation. *Journal of Materials Research*, vol. 32, nº 21, 2017, p. 4041–4053, Cambridge University Press.

[ESP 12] Espinosa H. D., Bernal R. A., Filleter T.

In situ TEM electromechanical testing of nanowires and nanotubes. *Small*, vol. 8, nº 21, 2012, p. 3233–3252, Wiley Online Library.

[FOS 13] Fossati P., Van Brutzel L., Devincre B.

Molecular dynamics simulation of dislocations in uranium dioxide. *Journal of nuclear materials*, vol. 443, nº 1-3, 2013, p. 359–365, Elsevier.

[FRA 19a] Frankberg E. J., Kalikka J., García Ferré F., Joly-Pottuz L., Salminen T., Hintikka J., Hokka M., Koneti S., Douillard T., Le Saint B. et al.

Highly ductile amorphous oxide at room temperature and high strain rate. *Science*, vol. 366, nº 6467, 2019, p. 864–869, American Association for the Advancement of Science.

[FRA 19b] Frazer D., Hosemann P.

Plasticity of UO2 studied and quantified via elevated temperature micro compression testing. *Journal of Nuclear Materials*, vol. 525, 2019, p. 140–144, Elsevier.

[FRA 21] Frazer D., Maiorov B., Carvajal-Nuñez U., Evans J., Kardoulaki E., Dunwoody J., Saleh T. A., White J. T.

High temperature mechanical properties of fluorite crystal structured materials (CeO2, ThO2, and UO2) and advanced accident tolerant fuels (U3Si2, UN, and UB2). *Journal of Nuclear Materials*, vol. 554, 2021, Page 153035, Elsevier.

[FRI 89] Fries E., Guiberteau F., Dominguez-Rodriguez A., Cheong D.-S., Heuer A.

High-temperature plastic deformation of Y2O3-stabilized ZrO2 single crystals. I. The

Cette thèse est accessible à l'adresse : https://theses.insa-lyon.fr/publication/2022ISAL0090/these.pdf
© [R. Zhang], [2022], INSA Lyon, tous droits réservés

origin of the yield drop and associated glide polygonization. *Philosophical Magazine A*, vol. 60, n° 1, 1989, p. 107–121, Taylor & Francis.

[FRI 07] Frick C., Orso S., Arzt E.

Loss of pseudoelasticity in nickel–titanium sub-micron compression pillars. *Acta Materialia*, vol. 55, n° 11, 2007, p. 3845–3855, Elsevier.

[GAB 78] Gaboriaud R., Denanot M., Boisson Grilhé M. E. J.

Etude des dislocations par microscopie électronique dans l'oxyde d'yttrium (Y2O3) monocristallin déformé plastiquement. *physica status solidi (a)*, vol. 46, n° 1, 1978, p. 387–396, Wiley Online Library.

[GAB 79] Gaboriaud R., Cadoz J.

Etude par microscopie électronique à haute tension de la configuration des dislocations, dans l'oxyde d'yttrium (Y2O3) monocristallin déformé plastiquement. *physica status solidi (a)*, vol. 52, n° 1, 1979, p. 95–101, Wiley Online Library.

[GAB 09] Gaboriaud R.

Dislocation core and pipe diffusion in Y2O3. *Journal of Physics D: Applied Physics*, vol. 42, n° 13, 2009, Page 135410, IOP Publishing.

[GAB 12] Gaboriaud R. J., Lacroix B., Paumier F.

Ion irradiation-induced phase transformations in bixbyite-fluorite related oxides: The role of dislocation loop nucleation. *Nuclear Instruments and Methods in Physics Research Section B: Beam Interactions with Materials and Atoms*, vol. 277, 2012, p. 18–20, Elsevier.

[GAB 13] Gaboriaud R., Paumier F., Jublot M., Lacroix B.

Ion irradiation-induced phase transformation mechanisms in Y2O3 thin films. *Nuclear Instruments and Methods in Physics Research Section B: Beam Interactions with Materials and Atoms*, vol. 311, 2013, p. 86–92, Elsevier.

[GAR 99] Garvie L., Buseck P.

Determination of Ce4+/Ce3+ in electron-beam-damaged CeO2 by electron energy-loss spectroscopy. *Journal of Physics and Chemistry of solids*, vol. 60, n° 12, 1999, p. 1943–1947, Elsevier.

Cette thèse est accessible à l'adresse : https://theses.insa-lyon.fr/publication/2022ISAL0090/these.pdf
© [R. Zhang], [2022], INSA Lyon, tous droits réservés

[GOM 14] Gomis O., Santamaría-Pérez D., Ruiz-Fuertes J., Sans J., Vilaplana R., Ortiz H., García-Domene B., Manjón F., Errandonea D., Rodríguez-Hernández P. et al.

High-pressure structural and elastic properties of Tl2O3. *Journal of Applied Physics*, vol. 116, n° 13, 2014, Page 133521, AIP Publishing LLC.

[GOR 14] Goris B., Turner S., Bals S., Van Tendeloo G.

Three-dimensional valency mapping in ceria nanocrystals. *Acs Nano*, vol. 8, n° 10, 2014, p. 10878–10884, ACS Publications.

[GRE 05] Greer J. R., Oliver W. C., Nix W. D.

Size dependence of mechanical properties of gold at the micron scale in the absence of strain gradients. *Acta Materialia*, vol. 53, n° 6, 2005, p. 1821–1830, Elsevier.

[GRE 08] Greer J. R., Weinberger C. R., Cai W.

Comparing the strength of fcc and bcc sub-micrometer pillars: Compression experiments and dislocation dynamics simulations. *Materials Science and Engineering: A*, vol. 493, n° 1-2, 2008, p. 21–25, Elsevier.

[GUI 19] Guillon O.

Advanced ceramics for energy conversion and storage. Elsevier, 2019.

[GUO 11] Guo H., Chen K., Oh Y., Wang K., Dejoie C., Syed Asif S., Warren O., Shan Z., Wu J., Minor A.

Mechanics and dynamics of the strain-induced M1–M2 structural phase transition in individual VO2 nanowires. *Nano letters*, vol. 11, n° 8, 2011, p. 3207–3213, ACS Publications.

[HAL 51] Hall E.

The deformation and ageing of mild steel: III discussion of results. *Proceedings of the Physical Society. Section B*, vol. 64, n° 9, 1951, Page 747, IOP Publishing.

[HAN 07] Han X., Zhang Y., Zheng K., Zhang X., Zhang Z., Hao Y., Guo X., Yuan J., Wang Z.

Low-temperature in situ large strain plasticity of ceramic SiC nanowires and its atomic-scale mechanism. *Nano letters*, vol. 7, n° 2, 2007, p. 452–457, ACS Publications.

Cette thèse est accessible à l'adresse : https://theses.insa-lyon.fr/publication/2022ISAL0090/these.pdf
© [R. Zhang], [2022], INSA Lyon, tous droits réservés

[HAN 15] Han W.-Z., Huang L., Ogata S., Kimizuka H., Yang Z.-C., Weinberger C., Li Q.-J., Liu B.-Y., Zhang X.-X., Li J. et al.

From "Smaller is Stronger" to "Size-Independent Strength Plateau": Towards Measuring the Ideal Strength of Iron. *Advanced Materials*, vol. 27, n° 22, 2015, p. 3385–3390, Wiley Online Library.

[HAN 16] Hansen T. W., Wagner J. B.

Controlled atmosphere transmission electron microscopy. *Switzerland: Springer International Publishing*, , 2016, p. 213–235, Springer.

[HAO 18] Hao X., Yoko A., Chen C., Inoue K., Saito M., Seong G., Takami S., Adschiri T., Ikuhara Y.

Atomic-Scale Valence State Distribution inside Ultrafine CeO2 Nanocubes and Its Size Dependence. *Small*, vol. 14, n° 42, 2018, Page 1802915, Wiley Online Library.

[HSI 19] Hsiao H.-W., Li S., Dahmen K. A., Zuo J.-M.

Shear banding mechanism in compressed nanocrystalline ceramic nanopillars. *Physical Review Materials*, vol. 3, n° 8, 2019, Page 083601, APS.

[HU 14] Hu J., Liu Z., Cui Y., Wang Z., Shan Z., Zhuang Z.

Sensitive material behavior: theoretical model and experiment for compression collapse of gold particles at submicron scale. *Journal of Applied Mechanics*, vol. 81, n° 9, 2014, American Society of Mechanical Engineers Digital Collection.

[HUA 96] Huang J., Wu Y., Ye H.

Deformation structures in ball milled copper. *Acta materialia*, vol. 44, n° 3, 1996, p. 1211–1221, Elsevier.

[HUA 11] Huang L., Li Q.-J., Shan Z.-W., Li J., Sun J., Ma E.

A new regime for mechanical annealing and strong sample-size strengthening in body centred cubic molybdenum. *Nature communications*, vol. 2, n° 1, 2011, p. 1–6, Nature Publishing Group.

[ISL 19] Islam M., Rajak P., Bhattacharyya S.

Ab initio calculation insights into the structural, elastic and mechanical properties of high-k dielectric gadolinium oxide (Gd2O3). *Applied Physics A*, vol. 125, n° 11, 2019, p. 1–6, Springer.

Cette thèse est accessible à l'adresse : https://theses.insa-lyon.fr/publication/2022ISAL0090/these.pdf
© [R. Zhang], [2022], INSA Lyon, tous droits réservés

[ISS 15] Issa I., Amodeo J., Réthoré J., Joly-Pottuz L., Esnouf C., Morthomas J., Perez M., Chevalier J., Masenelli-Varlot K.

In situ investigation of MgO nanocube deformation at room temperature. *Acta Materialia*, vol. 86, 2015, p. 295–304, Elsevier.

[ISS 16] Issa I., Amodeo J., Joly-Pottuz L., Réthoré J., Esnouf C., Garnier V., Morthomas J., Masenelli-Varlot K.

In situ TEM nanocompression of MgO nanocubes and mechanical analysis. *European Microscopy Congress 2016: Proceedings* Wiley Online Library, 2016, p. 255–256.

[ISS 18] Issa I., Joly-Pottuz L., Réthoré J., Esnouf C., Douillard T., Garnier V., Chevalier J., Le Floch S., Machon D., Masenelli-Varlot K.

Room temperature plasticity and phase transformation of nanometer-sized transition alumina nanoparticles under pressure. *Acta Materialia*, vol. 150, 2018, p. 308–316, Elsevier.

[ISS 21] Issa I., Joly-Pottuz L., Amodeo J., Dunstan D. J., Esnouf C., Réthoré J., Garnier V., Chevalier J., Masenelli-Varlot K.

From dislocation nucleation to dislocation multiplication in ceramic nanoparticle. *Materials Research Letters*, vol. 9, n° 6, 2021, p. 278–283, Taylor & Francis.

[JAV 18] Javed Y., Ali K., Akhtar K., Hussain M. I., Ahmad G., Arif T. et al.

TEM for atomic-scale study: Fundamental, instrumentation, and applications in nanotechnology. *Handbook of materials characterization*, p. 147–216 Springer, 2018.

[JIA 16] Jiang N.

Beam damage by the induced electric field in transmission electron microscopy. *Micron*, vol. 83, 2016, p. 79–92, Elsevier.

[JUB 07] Jublot M., Paumier F., Pailloux F., Lacroix B., Leau E., Guerin P., Marteau M., Jaouen M., Gaboriaud R., Imhoff D.

Yttrium oxide thin films: Influence of the oxygen vacancy network organization on the microstructure. *thin solid Films*, vol. 515, n° 16, 2007, p. 6385–6390, Elsevier.

[KAR 87] Karch J., Birringer R., Gleiter H.

Ceramics ductile at low temperature. *Nature*, vol. 330, n° 6148, 1987, p. 556–558, Nature Publishing Group.

Cette thèse est accessible à l'adresse : https://theses.insa-lyon.fr/publication/2022ISAL0090/these.pdf
© [R. Zhang], [2022], INSA Lyon, tous droits réservés

[KEL 71] Kelly A., Nicholson R.

Strengthening methods in crystals. Elsevier publishing company, 1971.

[KEL 81] Keller R., Mitchell T., Heuer A.

Slip systems in UO2+ x. *Le Journal de Physique Colloques*, vol. 42, n° C3, 1981, p. C3–73, EDP Sciences.

[KEL 88] Keller R., Mitchell T., Heuer A. H.

Plastic deformation in nonstoichiometric UO2+ x single crystals—I. Deformation at low temperatures. *Acta metallurgica*, vol. 36, n° 4, 1988, p. 1061–1071, Elsevier.

[KIE 06] Kiener D., Motz C., Schöberl T., Jenko M., Dehm G.

Determination of mechanical properties of copper at the micron scale. *Advanced Engineering Materials*, vol. 8, n° 11, 2006, p. 1119–1125, Wiley Online Library.

[KIE 10] Kiener D., Motz C., Grosinger W., Weygand D., Pippan R.

Cyclic response of copper single crystal micro-beams. *Scripta Materialia*, vol. 63, n° 5, 2010, p. 500–503, Elsevier.

[KIE 11] Kiener D., Minor A. M.

Source truncation and exhaustion: insights from quantitative in situ TEM tensile testing. *Nano letters*, vol. 11, n° 9, 2011, p. 3816–3820, ACS Publications.

[KIM 18] Kim H. J.

Abrasive for chemical mechanical polishing. *Abrasive Technology-Characteristics and Applications*, p. 183–201 IntechOpen, 2018.

[KNO 32] Knoll M., Ruska E.

Das elektronenmikroskop. *Zeitschrift für physik*, vol. 78, n° 5, 1932, p. 318–339, Springer.

[KRA 10] Kraft O., Gruber P. A., Mönig R., Weygand D.

Plasticity in confined dimensions. *Annual review of materials research*, vol. 40, 2010, p. 293–317, Annual Reviews.

[KÜM 99] Kümmerle E., Heger G.

The structures of C–Ce2O3+ δ, Ce7O12, and Ce11O20. *Journal of Solid State Chemistry*, vol. 147, n° 2, 1999, p. 485–500, Elsevier.

Cette thèse est accessible à l'adresse : https://theses.insa-lyon.fr/publication/2022ISAL0090/these.pdf
© [R. Zhang], [2022], INSA Lyon, tous droits réservés

[LAG 02] Lagerlöf K., Castaing J., Pirouz P., Heuer A.

Nucleation and growth of deformation twins: a perspective based on the double-cross-slip mechanism of deformation twinning. *Philosophical Magazine A*, vol. 82, n° 15, 2002, p. 2841–2854, Taylor & Francis.

[LAW 64] Lawley A., Gaigher H.

Deformation structures in zone-melted molybdenum. *Philosophical Magazine*, vol. 10, n° 103, 1964, p. 15–33, Taylor & Francis.

[LEE 12] Lee S.-W., Nix W. D.

Size dependence of the yield strength of fcc and bcc metallic micropillars with diameters of a few micrometers. *Philosophical Magazine*, vol. 92, n° 10, 2012, p. 1238–1260, Taylor & Francis.

[LEE 16] Lee S., Jeong J., Kim Y., Han S. M., Kiener D., Oh S. H.

FIB-induced dislocations in Al submicron pillars: Annihilation by thermal annealing and effects on deformation behavior. *Acta Materialia*, vol. 110, 2016, p. 283–294, Elsevier.

[LI 18] Li Z., Cheng X., Li J., Wang H.

Formation of face-centered cubic titanium in laser surface re-melted commercially pure titanium plate. *Journal of Materials Science & Technology*, vol. 34, n° 5, 2018, p. 767–773, Elsevier.

[LI 19] Li J., Cho J., Ding J., Charalambous H., Xue S., Wang H., Phuah X. L., Jian J., Wang X., Ophus C. et al.

Nanoscale stacking fault–assisted room temperature plasticity in flash-sintered TiO2. *Science advances*, vol. 5, n° 9, 2019, Page eaaw5519, American Association for the Advancement of Science.

[LIN 19] Lin Y., Li D., Zhang M., Zhan S., Yang Y., Yang H., Yuan Q.

Excellent energy-storage properties achieved in BaTiO3-based lead-free relaxor ferroelectric ceramics via domain engineering on the nanoscale. *ACS applied materials & interfaces*, vol. 11, n° 40, 2019, p. 36824–36830, ACS Publications.

[LIU 64] Liu T., Li C.

Plasticity of Barium Fluoride Single Crystals. *Journal of Applied Physics*, vol. 35, n°

Cette thèse est accessible à l'adresse : https://theses.insa-lyon.fr/publication/2022ISAL0090/these.pdf
© [R. Zhang], [2022], INSA Lyon, tous droits réservés

11, 1964, p. 3325–3330, American Institute of Physics.

[LIU 09] Liu Z., Liu X., Zhuang Z., You X.

Atypical three-stage-hardening mechanical behavior of Cu single-crystal micropillars. *Scripta Materialia*, vol. 60, n° 7, 2009, p. 594–597, Elsevier.

[LIU 12] Liu L., Song H. X., Wang Z., Geng H. Y., Jing Q., Zhang Y., Liu S., Xiang S., Bi Y., Xu J. et al.

Strength and equation of state of fluorite phase CeO2 under high pressure. *Journal of Applied Physics*, vol. 112, n° 1, 2012, Page 013532, American Institute of Physics.

[LIU 14] Liu B.-Y., Wang J., Li B., Lu L., Zhang X.-Y., Shan Z.-W., Li J., Jia C.-L., Sun J., Ma E.

Twinning-like lattice reorientation without a crystallographic twinning plane. *Nature communications*, vol. 5, n° 1, 2014, p. 1–6, Nature Publishing Group.

[LUF 70a] Luft A.

The correlation between dislocation structure and work-hardening behaviour of molybdenum single crystals deformed at 293° K. *physica status solidi (b)*, vol. 42, n° 1, 1970, p. 429–440, Wiley Online Library.

[LUF 70b] Luft A., Kaun L.

Electron microscopic investigation of the dislocation structure in molybdenum single crystals deformed in tension at 293 and 493 K. *physica status solidi (b)*, vol. 37, n° 2, 1970, p. 781–793, Wiley Online Library.

[MAA 07] Maass R., Van Petegem S., Van Swygenhoven H., Derlet P. M., Volkert C. A., Grolimund D.

Time-resolved Laue diffraction of deforming micropillars. *Physical review letters*, vol. 99, n° 14, 2007, Page 145505, APS.

[MAN 74] Mann A.

Structural relationships and mechanisms for the stoichiometry change from MX3 (YF3-type) through MX2 (fluorite-type) to M2X3 (C-type sesquioxide). *Journal of Solid State Chemistry*, vol. 11, n° 2, 1974, p. 94–105, Elsevier.

[MAN 15] Mansur A., Nganbe M.

Assessment of Three Finite Element Approaches for Modeling the Ballistic Impact Fail-

Cette thèse est accessible à l'adresse : https://theses.insa-lyon.fr/publication/2022ISAL0090/these.pdf
© [R. Zhang], [2022], INSA Lyon, tous droits réservés

ure of Metal Plates. *Journal of Materials Engineering and Performance*, vol. 24, n° 3, 2015, p. 1322–1331, Springer.

[MAT] Matsumura S., Yasuda K., Bhuian A. S. I., Takaki S.

High Voltage Electron Microscope Study of Lattice Defect Formation in Fluorite-type Oxide Crystals.

[MEK 03] Mekata M.

Kagome: The story of the basketweave lattice. *Physics Today*, vol. 56, n° 2, 2003, Page 12.

[MEN 62] Mendelson S.

Dislocations and Plastic Flow in NaCl Single Crystals. I. *Journal of Applied Physics*, vol. 33, n° 7, 1962, p. 2175–2181, American Institute of Physics.

[MEY 08] Meyers M. A., Chawla K. K.

Mechanical behavior of materials. Cambridge university press, 2008.

[MIN 06] Minor A. M., Syed Asif S., Shan Z., Stach E. A., Cyrankowski E., Wyrobek T. J., Warren O. L.

A new view of the onset of plasticity during the nanoindentation of aluminium. *Nature materials*, vol. 5, n° 9, 2006, p. 697–702, Nature Publishing Group.

[MIT 99] Mitchell T. E.

Dislocations and mechanical properties of MgO-Al2O3 spinel single crystals. *Journal of the American Ceramic Society*, vol. 82, n° 12, 1999, p. 3305–3316, Wiley Online Library.

[MOG 00] Mogensen M., Sammes N. M., Tompsett G. A.

Physical, chemical and electrochemical properties of pure and doped ceria. *Solid State Ionics*, vol. 129, n° 1-4, 2000, p. 63–94, Elsevier.

[MOM 08] Momma K., Izumi F.

VESTA: a three-dimensional visualization system for electronic and structural analysis. *Journal of Applied crystallography*, vol. 41, n° 3, 2008, p. 653–658, International Union of Crystallography.

Cette thèse est accessible à l'adresse : https://theses.insa-lyon.fr/publication/2022ISAL0090/these.pdf
© [R. Zhang], [2022], INSA Lyon, tous droits réservés

[MOO 09] Mook W., Niederberger C., Bechelany M., Philippe L., Michler J.
Compression of freestanding gold nanostructures: from stochastic yield to predictable flow. *Nanotechnology*, vol. 21, n° 5, 2009, Page 055701, IOP Publishing.

[MUH 01] Muhlstein C. L., Brown S. B., Ritchie R. O.
High-cycle fatigue of single-crystal silicon thin films. *Journal of microelectromechanical systems*, vol. 10, n° 4, 2001, p. 593–600, IEEE.

[MUN 94] Munoz A., Domínguez-Rodríguez A., Castaing J.
Slip systems and plastic anisotropy in CaF2. *Journal of materials science*, vol. 29, n° 23, 1994, p. 6207–6211, Springer.

[MUR 75] Murr L. E.
Interfacial phenomena in metals and alloys. , 1975, Addison-Wesley Publishing Company, Reading, MA.

[NAM 08] Namazu T., Isono Y.
Fatigue life prediction criterion for micro–nanoscale single-crystal silicon structures. *Journal of Microelectromechanical Systems*, vol. 18, n° 1, 2008, p. 129–137, IEEE.

[NIN 90] Ning X., Ye H.
In situ observations of dislocation motion and relevant surface phenomena in Eu2O3. *Philosophical Magazine A*, vol. 62, n° 4, 1990, p. 431–446, Taylor & Francis.

[NIX 89] Nix W. D.
Mechanical properties of thin films. *Metallurgical transactions A*, vol. 20, n° 11, 1989, p. 2217–2245, Springer.

[NIX 98] Nix W. D., Gao H.
Indentation size effects in crystalline materials: a law for strain gradient plasticity. *Journal of the Mechanics and Physics of Solids*, vol. 46, n° 3, 1998, p. 411–425, Elsevier.

[NIX 11] Nix W. D., Lee S.-W.
Micro-pillar plasticity controlled by dislocation nucleation at surfaces. *Philosophical Magazine*, vol. 91, n° 7-9, 2011, p. 1084–1096, Taylor & Francis.

[OH 07] Oh S. H., Legros M., Kiener D., Gruber P., Dehm G.
In situ TEM straining of single crystal Au films on polyimide: Change of deformation

Cette thèse est accessible à l'adresse : https://theses.insa-lyon.fr/publication/2022ISAL0090/these.pdf
© [R. Zhang], [2022], INSA Lyon, tous droits réservés

mechanisms at the nanoscale. *Acta materialia*, vol. 55, n° 16, 2007, p. 5558–5571, Elsevier.

[OH 09] Oh S. H., Legros M., Kiener D., Dehm G.

In situ observation of dislocation nucleation and escape in a submicrometre aluminium single crystal. *Nature materials*, vol. 8, n° 2, 2009, p. 95–100, Nature Publishing Group.

[OUY 09] Ouyang C., Li Z., Huang M., Hu L., Hou C.

Combined influences of micro-pillar geometry and substrate constraint on microplastic behavior of compressed single-crystal micro-pillar: Two-dimensional discrete dislocation dynamics modeling. *Materials Science and Engineering: A*, vol. 526, n° 1-2, 2009, p. 235–243, Elsevier.

[PAR 07] Parthasarathy T. A., Rao S. I., Dimiduk D. M., Uchic M. D., Trinkle D. R.

Contribution to size effect of yield strength from the stochastics of dislocation source lengths in finite samples. *Scripta Materialia*, vol. 56, n° 4, 2007, p. 313–316, Elsevier.

[PET 53] Petch N.

The cleavage strength of polycrystals. *Journal of the iron and steel institute*, vol. 174, 1953, p. 25–28.

[PLE 18] Pletnev P., Pogrebenkov V., Vereshchagin V., Tyul'kin D.

Corundum refractory material in alumina-binder resistant to high-temperature deformation. *Refractories and Industrial Ceramics*, vol. 59, n° 1, 2018, p. 85–90, Springer.

[POR 18] Portelette L., Amodeo J., Madec R., Soulacroix J., Helfer T., Michel B.

Crystal viscoplastic modeling of UO2 single crystal. *Journal of Nuclear Materials*, vol. 510, 2018, p. 635–643, Elsevier.

[POR 20] Portelette L., Amodeo J., Michel B., Madec R.

Athermal dislocation strengthening in UO2. *Journal of Nuclear Materials*, vol. 538, 2020, Page 152157, Elsevier.

Cette thèse est accessible à l'adresse : https://theses.insa-lyon.fr/publication/2022ISAL0090/these.pdf
© [R. Zhang], [2022], INSA Lyon, tous droits réservés

[QI 13] Qi Y.-Y., Niu Z.-W., Cheng C., Cheng Y.

Structural and elastic properties of Ce2O3 under pressure from LDA+ U method. *Frontiers of Physics*, vol. 8, nº 4, 2013, p. 405–411, Springer.

[RAO 07] Rao S. I., Dimiduk D., Tang M., Uchic M., Parthasarathy T., Woodward C.

Estimating the strength of single-ended dislocation sources in micron-sized single crystals. *Philosophical Magazine*, vol. 87, nº 30, 2007, p. 4777–4794, Taylor & Francis.

[REE 88] Reed J. S.

Introduction to the Principles of Ceramic Processing. 1988.

[REI 20] Reimnitz L. C., Lwin T., Lopez M., Milliron D. J.

Oxygen storage in transition metal-doped bixbyite vanadium sesquioxide nanocrystals. *ACS Applied Nano Materials*, vol. 3, nº 10, 2020, p. 9645–9651, ACS Publications.

[RIV 22] Rivas D. E., Serkez S., Baumann T. M., Boll R., Czwalinna M. K., Dold S., de Fanis A., Gerasimova N., Grychtol P., Lautenschlager B. et al. High-temporal-resolution X-ray spectroscopy with free-electron and optical lasers. *Optica*, vol. 9, nº 4, 2022, p. 429–430, Optica Publishing Group.

[ROA 09] Roa J., Gilioli E., Bissoli F., Pattini F., Rampino S., Capdevila X., Segarra M.

Study of the mechanical properties of CeO2 layers with the nanoindentation technique. *Thin Solid Films*, vol. 518, nº 1, 2009, p. 227–232, Elsevier.

[ROL 21] Roldán M., Sánchez F. J., Fernández P., Ortiz C. J., Gómez-Herrero A., Jiménez Rey D.

Dislocation Loop Generation Differences between Thin Films and Bulk in EFDA Pure Iron under Self-Ion Irradiation at 20 MeV. *Metals*, vol. 11, nº 12, 2021, Page 2000, Multidisciplinary Digital Publishing Institute.

[SAN 16] Sangsefidi F. S., Sabet M., Salavati-Niasari M.

Synthesis and characterization of ceria nanostructures with different morphologies via a simple thermal decompose method with different cerium complexes and investigation the photocatalytic activity. *Journal of Materials Science: Materials in Electronics*, vol. 27, nº 8, 2016, p. 8793–8801, Springer.

Cette thèse est accessible à l'adresse : https://theses.insa-lyon.fr/publication/2022ISAL0090/these.pdf
© [R. Zhang], [2022], INSA Lyon, tous droits réservés

[SAW 71] Sawbridge P., Sykes E.

Dislocation glide in UO2 single crystals at 1600 K. *Philosophical Magazine*, vol. 24, n° 187, 1971, p. 33–53, Taylor & Francis.

[SCH 09a] Schneider A., Clark B., Frick C., Gruber P., Arzt E.

Effect of orientation and loading rate on compression behavior of small-scale Mo pillars. *Materials Science and Engineering: A*, vol. 508, n° 1-2, 2009, p. 241–246, Elsevier.

[SCH 09b] Schneider A., Kaufmann D., Clark B., Frick C., Gruber P., Mönig R., Kraft O., Arzt E.

Correlation between critical temperature and strength of small-scale bcc pillars. *Physical review letters*, vol. 103, n° 10, 2009, Page 105501, APS.

[SEE 02] Seeger A.

Peierls barriers, kinks, and flow stress: recent progress. *International Journal of Materials Research*, vol. 93, n° 8, 2002, p. 760–777, De Gruyter.

[SHA 00] Sharif A. A., Misra A., Petrovic J. J., Mitchell T. E.

Dislocation motion in erbia single crystals. *Materials Science and Engineering: A*, vol. 290, n° 1-2, 2000, p. 164–170, Elsevier.

[SHA 08] Shan Z., Mishra R. K., Syed Asif S., Warren O. L., Minor A. M.

Mechanical annealing and source-limited deformation in submicrometre-diameter Ni crystals. *Nature materials*, vol. 7, n° 2, 2008, p. 115–119, Nature Publishing Group.

[SHE 79] Sherry W., Vander Sande J.

TEM investigation of the plastic deformation behaviour of calcium fluoride. *Philosophical Magazine A*, vol. 40, n° 1, 1979, p. 77–95, Taylor & Francis.

[SIC 06] Sickafus K., Grimes R., Corish S., Cleave A., Tang M., Stanek C., Uberuaga B., Valdez J.

Los Alamos Series Report# LA-14205: Layered Atom Arrangements in Complex Materials. *Los Alamos National Laboratory, Los Alamos, NM*, , 2006.

[SIK 05] Sikafus K., Grimes R., Corish S., Cleave A., Tang M., Stanek C., Uberuaga B., Valdez J.

Layered atom arrangements in complex materials. rapport, 2005, Los Alamos National Lab.(LANL), Los Alamos, NM (United States).

Cette thèse est accessible à l'adresse : https://theses.insa-lyon.fr/publication/2022ISAL0090/these.pdf
© [R. Zhang], [2022], INSA Lyon, tous droits réservés

[SOE 07] Soer W., De Hosson J. T. M., Minor A., Shan Z., Syed Asif S., Warren O.

Incipient plasticity in metallic thin films. *Applied physics letters*, vol. 90, n° 18, 2007, Page 181924, American Institute of Physics.

[SUZ 19] Suzuki K., Kato M., Sunaoshi T., Uno H., Carvajal-Nunez U., Nelson A. T., McClellan K. J.

Thermal and mechanical properties of CeO2. *Journal of the American Ceramic Society*, vol. 102, n° 4, 2019, p. 1994–2008, Wiley Online Library.

[TAN 08] Tang H., Schwarz K., Espinosa H.

Dislocation-source shutdown and the plastic behavior of single-crystal micropillars. *Physical review letters*, vol. 100, n° 18, 2008, Page 185503, APS.

[TIW 18] Tiwari S., Balasubramanian N., Biring S., Sen S.

Effect of Co doping on structural and mechanical properties of CeO2. *AIP Conference Proceedings*, vol. 1966 AIP Publishing LLC, 2018, Page 020037.

[TRA 14] Travitzky N., Bonet A., Dermeik B., Fey T., Filbert-Demut I., Schlier L., Schlordt T., Greil P.

Additive manufacturing of ceramic-based materials. *Advanced engineering materials*, vol. 16, n° 6, 2014, p. 729–754, Wiley Online Library.

[TRA 15] Tracy C. L., Lang M., Zhang F., Trautmann C., Ewing R. C.

Phase transformations in Ln 2 O 3 materials irradiated with swift heavy ions. *Physical Review B*, vol. 92, n° 17, 2015, Page 174101, APS.

[TRE 19] Trenque I., Magnano G. C., Bolzinger M. A., Roiban L., Chaput F., Pitault I., Briançon S., Devers T., Masenelli-Varlot K., Bugnet M. et al.

Shape-selective synthesis of nanoceria for degradation of paraoxon as a chemical warfare simulant. *Physical Chemistry Chemical Physics*, vol. 21, n° 10, 2019, p. 5455–5465, Royal Society of Chemistry.

[TUR 11] Turner S., Lazar S., Freitag B., Egoavil R., Verbeeck J., Put S., Strauven Y., Van Tendeloo G.

High resolution mapping of surface reduction in ceria nanoparticles. *Nanoscale*, vol. 3, n° 8, 2011, p. 3385–3390, Royal Society of Chemistry.

Cette thèse est accessible à l'adresse : https://theses.insa-lyon.fr/publication/2022ISAL0090/these.pdf
© [R. Zhang], [2022], INSA Lyon, tous droits réservés

[UCH 04] Uchic M. D., Dimiduk D. M., Florando J. N., Nix W. D.
Sample dimensions influence strength and crystal plasticity. *Science*, vol. 305, n° 5686, 2004, p. 986–989, American Association for the Advancement of Science.

[UCH 06] Uchic M. D., Dimiduk D. M., Wheeler R., Shade P. A., Fraser H. L.
Application of micro-sample testing to study fundamental aspects of plastic flow. *Scripta materialia*, vol. 54, n° 5, 2006, p. 759–764, Elsevier.

[VAN 04] Van Swygenhoven H., Derlet P. M., Frøseth A.
Stacking fault energies and slip in nanocrystalline metals. *Nature materials*, vol. 3, n° 6, 2004, p. 399–403, Nature Publishing Group.

[VEN 61] Venables J.
Deformation twinning in face-centred cubic metals. *Philosophical magazine*, vol. 6, n° 63, 1961, p. 379–396, Taylor & Francis.

[VOL 06a] Volkert C., Lilleodden E., Kramer D., Weissmüller J.
Approaching the theoretical strength in nanoporous Au. *Applied Physics Letters*, vol. 89, n° 6, 2006, Page 061920, American Institute of Physics.

[VOL 06b] Volkert C. A., Lilleodden E. T.
Size effects in the deformation of sub-micron Au columns. *Philosophical Magazine*, vol. 86, n° 33-35, 2006, p. 5567–5579, Taylor & Francis.

[WAN 08] Wang D., Volkert C., Kraft O.
Effect of length scale on fatigue life and damage formation in thin Cu films. *Materials Science and Engineering: A*, vol. 493, n° 1-2, 2008, p. 267–273, Elsevier.

[WAN 12] Wang Z.-J., Shan Z.-W., Li J., Sun J., Ma E.
Pristine-to-pristine regime of plastic deformation in submicron-sized single crystal gold particles. *Acta Materialia*, vol. 60, n° 3, 2012, p. 1368–1377, Elsevier.

[WAN 15a] Wang X., Chen K., Zhang Y., Wan J., Warren O. L., Oh J., Li J., Ma E., Shan Z.
Growth conditions control the elastic and electrical properties of ZnO nanowires. *Nano letters*, vol. 15, n° 12, 2015, p. 7886–7892, ACS Publications.

[WAN 15b] Wang Z.-J., Li Q.-J., Cui Y.-N., Liu Z.-L., Ma E., Li J., Sun J., Zhuang Z., Dao M., Shan Z.-W. et al.

Cette thèse est accessible à l'adresse : https://theses.insa-lyon.fr/publication/2022ISAL0090/these.pdf
© [R. Zhang], [2022], INSA Lyon, tous droits réservés

Cyclic deformation leads to defect healing and strengthening of small-volume metal crystals. *Proceedings of the National Academy of Sciences*, vol. 112, n° 44, 2015, p. 13502–13507, National Acad Sciences.

[WAN 17a] Wang H., Li R., Zhou M., Cedelle J., Huang Z., Wang Q.

Grain boundary sliding mechanism in plastic deformation of nano-grained YAG transparent ceramics: Generalized self-consistent model and nanoindentation experimental validation. *Journal of the European Ceramic Society*, vol. 37, n° 7, 2017, p. 2705–2715, Elsevier.

[WAN 17b] Wang L., Guan P., Teng J., Liu P., Chen D., Xie W., Kong D., Zhang S., Zhu T., Zhang Z. et al.

New twinning route in face-centered cubic nanocrystalline metals. *Nature communications*, vol. 8, n° 1, 2017, p. 1–7, Nature Publishing Group.

[WEI 08] Weinberger C. R., Cai W.

Surface-controlled dislocation multiplication in metal micropillars. *Proceedings of the National Academy of Sciences*, vol. 105, n° 38, 2008, p. 14304–14307, National Acad Sciences.

[WIL 96] Williams D. B., Carter C. B.

The transmission electron microscope. *Transmission electron microscopy*, p. 3–17 Springer, 1996.

[WU 04] Wu L., Wiesmann H., Moodenbaugh A., Klie R., Zhu Y., Welch D., Suenaga M.

Oxidation state and lattice expansion of CeO 2- x nanoparticles as a function of particle size. *Physical Review B*, vol. 69, n° 12, 2004, Page 125415, APS.

[WYC 63] Wyckoff R. W. G., Wyckoff R. W.

Crystal structures, vol. 1. Interscience publishers New York, 1963.

[XIE 21] Xie L., Cheng J., Wang T., Lu X.

Mechanical wear behavior between CeO2 (100), CeO2 (110), CeO2 (111), and silicon studied through atomic force microscopy. *Tribology International*, vol. 153, 2021, Page 106616, Elsevier.

Cette thèse est accessible à l'adresse : https://theses.insa-lyon.fr/publication/2022ISAL0090/these.pdf
© [R. Zhang], [2022], INSA Lyon, tous droits réservés

[XU 17] Xu N., Han W., Wang Y., Li J., Shan Z.

Nanoscratching of copper surface by CeO2. *Acta Materialia*, vol. 124, 2017, p. 343–350, Elsevier.

[XU 22] Xu N., Ma J., Liu Q., Han W., Shan Z.

Size Effect of CeO2 Particle On Nanoscale Single-Asperity Sliding Friction. *Tribology Letters*, vol. 70, n° 1, 2022, p. 1–10, Springer.

[YAM 02] Yamakov V., Wolf D., Phillpot S. R., Mukherjee A. K., Gleiter H.

Dislocation processes in the deformation of nanocrystalline aluminium by molecular-dynamics simulation. *Nature materials*, vol. 1, n° 1, 2002, p. 45–49, Nature Publishing Group.

[YAN 19] Yang G., Park S.-J.

Deformation of single crystals, polycrystalline materials, and thin films: A Review. *Materials*, vol. 12, n° 12, 2019, Page 2003, Multidisciplinary Digital Publishing Institute.

[YAS 03] Yashima M., Ishimura D., Yamaguchi Y., Ohoyama K., Kawachi K.

High-temperature neutron powder diffraction study of cerium dioxide CeO2 up to 1770 K. *Chemical physics letters*, vol. 372, n° 5-6, 2003, p. 784–787, Elsevier.

[ZHA 05] Zhao Y., Liao X., Zhu Y., Horita Z., Langdon T.

Influence of stacking fault energy on nanostructure formation under high pressure torsion. *Materials Science and Engineering: A*, vol. 410, 2005, p. 188–193, Elsevier.

[ZHA 06] Zhang G., Volkert C., Schwaiger R., Wellner P., Arzt E., Kraft O.

Length-scale-controlled fatigue mechanisms in thin copper films. *Acta Materialia*, vol. 54, n° 11, 2006, p. 3127–3139, Elsevier.

[ZHA 07] Zhang Y., Han X., Zheng K., Zhang Z., Zhang X., Fu J., Ji Y., Hao Y.-j., Guo X.-y., Wang Z.

Direct observation of super-plasticity of beta-SiC nanowires at low temperature. *Advanced Functional Materials*, vol. 17, n° 17, 2007, p. 3435–3440, Wiley Online Library.

[ZHA 13] Zhang J., Sha Z., Branicio P., Zhang Y., Sorkin V., Pei Q., Srolovitz D.

Superplastic nanocrystalline ceramics at room temperature and high strain rates. *Scripta Materialia*, vol. 69, n° 7, 2013, p. 525–528, Elsevier.

Cette thèse est accessible à l'adresse : https://theses.insa-lyon.fr/publication/2022ISAL0090/these.pdf
© [R. Zhang], [2022], INSA Lyon, tous droits réservés

[ZHU 12] Zhu Y., Liao X., Wu X.

Deformation twinning in nanocrystalline materials. *Progress in Materials Science*, vol. 57, n° 1, 2012, p. 1–62, Elsevier.

[ZIN 07] Zinkevich M.

Thermodynamics of rare earth sesquioxides. *Progress in Materials Science*, vol. 52, n° 4, 2007, p. 597–647, Elsevier.

Cette thèse est accessible à l'adresse : https://theses.insa-lyon.fr/publication/2022ISAL0090/these.pdf
© [R. Zhang], [2022], INSA Lyon, tous droits réservés

Cette thèse est accessible à l'adresse : https://theses.insa-lyon.fr/publication/2022ISAL0090/these.pdf
© [R. Zhang], [2022], INSA Lyon, tous droits réservés

FOLIO ADMINISTRATIF

THESE DE L'INSA LYON, MEMBRE DE L'UNIVERSITE DE LYON

NOM : ZHANG
(avec précision du nom de jeune fille, le cas échéant)

DATE de SOUTENANCE : le 24 Octobre 2022

Prénoms : Rongrong

TITRE : *In situ* compression of cerium oxides in environmental transmission electron microscopy

NATURE : Doctorat

Numéro d'ordre : 2022ISAL0090

Ecole doctorale : ED 34 Matériaux de Lyon

Spécialité : Science des Matériaux

RESUME : Les matériaux céramiques présentent une excellente résistance mécanique et sont utilisés dans de nombreux domaines. Cependant, la caractéristique la plus préjudiciable des céramiques est leur fragilité, qui limite leur application. Des recherches cependant ont montré que les matériaux céramiques à l'échelle nanométrique présentent une déformation plastique supérieure à celle de leurs homologues à l'état massif. Ce comportement plastique à l'échelle nanométrique pourrait être intéressant pour améliorer le traitement des céramiques, soit en diminuant l'énergie nécessaire au cours du processus, soit en optimisant la microstructure obtenue. Cependant, peu d'études sur le comportement plastique des matériaux céramiques ont été rapportées jusqu'à présent.
Cette étude porte sur des nanocubes d'oxydes de cérium dont la taille varie entre 20 et 130 nm. Nous utilisons des tests de nanocompression *in situ* en microscopie électronique à transmission environnementale (ETEM) sur des nanocubes isolés. La géométrie du cube permet de tester le cube le long d'une direction cristallographique connue, la direction [001]. Pendant le test, la courbe de contrainte/déformation est obtenue à partir du capteur du porte-échantillon et couplée à la vidéo de la nanoparticule comprimée.
En raison d'un effet de réduction du faisceau d'électrons dans le TEM, différentes structures sont analysées, de CeO_2 à Ce_2O_3 en fonction des conditions expérimentales (dose d'électrons ou présence de gaz autour de l'échantillon). Nous effectuons des tests de compression sur la bixbyite Ce_2O_3 et sur la fluorite CeO_2. Lors de la compression de la bixbyite, nous observons la formation de dislocations parfaites suivie de leur dissociation en partielles avec la formation de failles d'empilement. Ce mécanisme peut être comparé à ce qui est observé dans les structures métalliques FCC.
Dans la fluorite CeO_2, les dislocations apparaissent mais se dissocient rarement. En utilisant plusieurs axes de zone, les dislocations peuvent être indexées. Avec nos résultats, le système de glissement principal est identifié comme étant <110>{111}. Les nanocubes de CeO_2 montrent également une forte relation entre la taille du cube et la contrainte à l'écoulement . Cet effet de taille est discuté en utilisant des modèles de la littérature et en considérant le mécanisme de déformation.

MOTS-CLÉS : Cerium oxide; in situ; environmental transmission electron microscope; plasticity

Laboratoire (s) de recherche : Laboratoire MATEIS - INSA Lyon

Directrices de thèse : Karine Masenelli-Varlot INSA Lyon
Lucile Joly-Pottuz INSA Lyon

Président de jury :

Composition du jury :
Rapporteur : Olivier THOMAS, Aix-Marseille Université
Rapportrice : Anne JOULAIN, Université de Poitiers
Examinateur : Marc LEGROS, CEMES-CNRS
Examinateur : David COOPER, CEA-LETI
Examinateur : David DUNSTAN, Queen Mary University of London

Cette thèse est accessible à l'adresse : https://theses.insa-lyon.fr/publication/2022ISAL0090/these.pdf
© [R. Zhang], [2022], INSA Lyon, tous droits réservés

Cette thèse est accessible à l'adresse : https://theses.insa-lyon.fr/publication/2022ISAL0090/these.pdf
© [R. Zhang], [2022], INSA Lyon, tous droits réservés